A Novel Dynamic Forcing Scheme Incorporating Backscatter for Hybrid RANS/LES

A Thesis Submitted to the Committee

in Partial Fulfilment of the Requirements for the Degree of

Doctor of Philosophy

Department of Mechanical Engineering

University of Manitoba

Winnipeg, Manitoba

by

Qianqiu Xun

Abstract

In hybrid RANS/LES, Reynolds-averaged Navier-Stokes (RANS) equations method is used to treat the near-wall region and large-eddy simulation (LES) is applied to the core turbulent region. Owing to the incompatibility of these two numerical modelling approaches, an artificial (i.e., non-physical) buffer layer forms along the interface where the model switches from RANS to LES. In this thesis, a novel dynamic forcing scheme incorporating backscatter is proposed in order to remove the artificial buffer layer. In contrast to previous forcing techniques, the proposed forcing is determined dynamically from the flow field itself, and does not require any extraction of turbulent fields from reference direct numerical simulation (DNS) or high-resolution LES databases. The proposed forcing model has been tested on three types of wall-bounded turbulent flows, namely, turbulent flow in a plane channel; turbulent flow in a spanwise rotating channel; and turbulent flow in a spanwise rotating rib-roughened channel. In order to validate the present hybrid approach, turbulence statistics obtained from hybrid RANS/LES simulations are thoroughly compared with the available DNS results and laboratory measurement data. Based on the study of a plane channel flow, transport equations for the resolved turbulent stresses and kinetic energy are introduced to investigate the effects of dynamic forcing on reduction of the thickness and impact of the artificial buffer layer. As long as the dynamic forcing is in use, the artificial buffer layer have been successfully removed, indicating that the proposed hybrid approach is insensitive to the choices of the forcing region or interface location. The predictive performance of the dynamic forcing scheme has been further evaluated by considering turbulent flows subjected to a special type of body force, i.e., the non-inertial and non-conservative Coriolis force. Due to the effects of system rotation, turbulence level is enhanced on the pressure side and suppressed on the suction side of the rotating channel. Furthermore, it is reported in this thesis that the classification of the roughness type now relies not only on the pitch ratio, but also on the rotation number in the context of rotating rib-roughened flows.

Acknowledgements

I would like to express my profound appreciation to my supervisor, Professor Bing-Chen Wang, for his support and insightful guidance in my research and technical publications. My sincere thanks also go to Professor M. F. Tachie, Professor Y. Luo and Professor H. Soliman for their advice and help on my course studies.

I sincerely thank all my friends I have made in Winnipeg for bringing me so many joyful moments and encouragement.

Finally, I would like to express my deep love and appreciation to my parents, brothers, sisters, brothers-in-law and sisters-in-law, for their consistent and unconditional love and support.

I dedicate this thesis to my loving parents.

Table of Contents

List of Tables

List of Figures

Nomenclature

English Symbols

a	coefficient for discretized momentum and continuity equations
a_l	filter coefficients
A_i	cross-sectional area of a control volume perpendicular to the i-th dimension
b	source term of the discretized momentum and continuity equations
BR	Bradshaw-Richardson number: $s(s+1)$
C_f	skin friction coefficient
C_K	Kolmogorov constant
C_S	SGS stress model coefficient
C_W, C_N	coefficients in the dynamic forcing scheme
d	width of neutral stability region
D	wall damping function
$\mathcal{F}_i$	forcing term
G	filter function
G_{ij}, O_{ij}, P_{ij}	production terms for the resolved turbulent stresses
h	rib side length
H	channel height
$\mathcal{H}_i$	nonlinear term
i	index: $i = 1$, 2 and 3
I, J, K	index numbers
j	index: $j = 1$, 2 and 3
k	index: $k = 1$, 2 and 3; or resolved TKE

k^L	modelled SGS KE
k^R	total TKE
L_1, L_2, L_3	length, height, and width of the computational domain, respectively
$\mathcal{L}_{ij}$	Leonard-type stress tensor in the DSM
L_p	pitch length
N	number of the nodes for a 1-D discrete filter stencil
N_i	number of grid points in the x_i direction
N_{ij}	differential tensor in the dynamic forcing scheme
p	pressure
p_0	reference static pressure
P_k	production term for the resolved TKE
P_r^B	KE backscatter produced by the forcing
p'	pressure correction
q_0	reference dynamic pressure
Re	Reynolds number based on the bulk mean velocity: $U_b H/\nu$
Re_b	Reynolds number based on the bulk mean velocity: $U_b\delta/\nu$
Re_τ	Reynolds number based on the wall friction velocity: $u_\tau\delta/\nu$
Re_ℓ	Reynolds number based on integral length scale ℓ
Ro	rotation number based on the bulk mean velocity: $\Omega H/U_b$
Ro_b	rotation number based on the bulk mean velocity: $2\Omega\delta/U_b$
Ro_τ	rotation number based on the wall friction velocity: $2\Omega\delta/u_\tau$
s	dimensionless parameter: $-2\Omega/(d\langle\bar{u}_1\rangle/dx_2)$ or $2\Omega/\omega_3$
$\bar{S}_{ij}$	resolved (or mean) strain rate tensor: $(\partial\bar{u}_i/\partial x_j + \partial\bar{u}_j/\partial x_i)/2$
$\lvert\bar{S}\rvert$	norm of $\bar{S}_{ij}$: $\left(2\bar{S}_{ij}\bar{S}_{ij}\right)^{1/2}$
t	time
Δt	time step
T	averaging time interval
T_{ij}^B	forcing stress tensor at the test-grid level in the dynamic forcing scheme
u_i	velocity components: $i = 1, 2, 3$
u_τ	wall friction velocity

$u_i^{(\star)}$, $u_i^{(\star\star)}$	estimated velocity
U_b	bulk mean velocity
$\overline{v^2}$	velocity scale in the $\overline{v^2}$-f RANS closure model
W_{ij}	differential tensor in the dynamic forcing scheme
x_i	coordinates ($i = 1$, 2 and 3)
Δx_i	grid size in the x_i direction

Greek Symbols

α_{ij}	base tensor at the test-grid level in the DSM
β_{ij}	base tensor at the grid level in the DSM
δ	half channel height
δ_{ij}	Kronecker delta
Δ	mesh or filter size
ε	dissipation rate of TKE
ε_{ijk}	Levi-Civita symbol
ϵ	ratio between the cutoff sizes of the test-grid and grid filters: $\tilde{\bar{\Delta}}/\bar{\Delta}$
γ_{ij}, η_{ij}	base tensors at the grid level in the dynamic forcing scheme
κ	von Karman constant; or a wavenumber
λ_{ij}, ζ_{ij}	base tensors at the test-grid level in the dynamic forcing scheme
ν	kinematic viscosity
ν_t	eddy viscosity
ℓ	integral length scale in turbulence
η	Kolmogorov length scale in turbulence
ω_1	streamwise vorticity: $\partial\bar{u}_3/\partial x_2 - \partial\bar{u}_2/\partial x_3$
ω_3	mean spanwise vorticity: $\partial\langle\bar{u}_2\rangle/\partial x_1 - \partial\langle\bar{u}_1\rangle/\partial x_2$
Ω	angular velocity
$\bar{\Omega}_{ij}$	resolved rotation rate tensor: $(\partial\bar{u}_i/\partial x_j - \partial\bar{u}_j/\partial x_i)/2$

ν_t^L	eddy viscosity of the LES closure model
ν_t^R	eddy viscosity of the RANS closure model
ϕ	a flow variable
ρ	density
τ_{ij}	grid level SGS stress tensor in the LES closure model; or Reynolds stress tensor in the RANS closure model
τ_{ij}^B	forcing stress tensor at the grid level in the dynamic forcing scheme
τ_w	wall shear stress
ω	specific dissipation rate with dimension of inverse time

Subscripts and Superscripts

$(\ )_1$	streamwise component
$(\ )_2$	wall-normal component
$(\ )_3$	spanwise component
$(\ )_b$	value at the back face of a control volume
$(\ )_B$	value at the back neighbour node
$(\ )_e$	value at the east face of a control volume
$(\ )_E$	value at the east neighbour node
$(\ )_f$	value at the front face of a control volume
$(\ )_F$	value at the front neighbour node
$(\ )_i$, $(\ )_j$, $(\ )_{ij}$	vectors or second-order tensors: $i, j = 1, 2, 3$
$(\ )_{ij}^*$	trace-free format of a second-order tensor: $(\ )_{ij}^* = (\ )_{ij} - (\ )_{kk}\delta_{ij}/3$
$(\ )_n$	value at the north face of a control volume
$(\ )_N$	value at the north neighbour node
$(\ )_{NP}$	value at a neighbour node
$(\ )^{(n)}$, $(\ )^{(n+1)}$	result at the (n)-th and $(n+1)$-th time step, respectively
$(\ )_p$	value at the pressure wall

$(\,)_P$	value at the central node
$(\,)_{\mathrm{rms}}$	RMS value
$(\,)_s$	value at the south face of a control volume; or value at the suction wall
$(\,)_S$	value at the south neighbour node
$(\,)_w$	value at the west face of a control volume; or value at the wall
$(\,)_W$	value at the west neighbour node
$\overline{(\,)}$	grid level filter; or a resolved quantity
$\widetilde{(\,)}$	test-grid level filter
$\widehat{(\,)}$	Fourier transform
$(\,)'$, $(\,)''$	residual component
$(\,)^+$	wall coordinates
$\langle\,\rangle$	time- and plane-averaged quantity; or time- and spanwise-averaged quantity
$[\,]$	time-averaged quantity

Abbreviations

1-D	1-Dimensional
2-D	2-Dimensional
3-D	3-Dimensional
CFD	Computational Fluid Dynamics
CFL	Courant-Friedrichs-Lewy Condition
CPU	Central Processing Unit
CV	Control Volume
DES	Detached-Eddy Simulation
DSM	Dynamic Smagorinsky Model

DNS	Direct Numerical Simulation
KE	Kinetic Energy
LES	Large-Eddy Simulation
LHS	Left-Hand-Side
MPI	Message Passing Interface
NP	Neighbour Points
PDF	Probability Density Function
PIV	Particle Image Velocimetry
RANS	Reynolds-Averaged Navier-Stokes Method
RHS	Right-Hand-Side
RMS	Root-Mean-Square
SGS	Subgrid-Scale
SM	Smagorinsky Model
T-G	Taylor-Görtler
TKE	Turbulence Kinetic Energy

Chapter 1

Introduction

Turbulent flows are of considerable interest in engineering, physics, aeronautics, meteorology, agriculture and oceanography. The physical mechanisms underlying the transport of momentum, heat or mass in these examples are significantly affected by turbulence phenomena. For a proper engineering design of a system involving turbulence, engineers require the knowledge of turbulence, which has been obtained by either theory, laboratory experiments, or numerical simulations. In the first half of the 20th century, theoretical analysis and laboratory experiments were probably the most reliable way to gain insights into the physics of the flow. Ever since the 1960s, with the emergence of modern computational technologies, numerical simulations have been accomplished with desirable predictions of the turbulent flow for analysis.

There are three major numerical approaches, namely, direct numerical simulation (DNS), Reynolds-averaged Navier-Stokes (RANS) equations method, and large-eddy simulation (LES). Among them, DNS is the most reliable approach because it can provide complete and accurate flow information without any turbulence modelling. However, excessive computational resources and time are often required by the DNS approach, especially for scenarios involving complex flow physics. In RANS and LES approaches, turbulence modelling is introduced based on various levels of approximation and empiricism. It has been shown that numerical approaches with proper modelling strategies can bring up the possibility to study inherently unsteady phenomena in, e.g., the propagation of sound, the control of turbulence, and the dispersion of air pollutants. In a very general sense, the objective of this thesis is to take yet another (small) step towards such simulations. More specifically, this thesis aims to propose a novel strategy for turbulence modelling to obtain desirable results of turbulent flows by using reasonable computational resources (less than 10% of those used by DNS at the same Reynolds number).

1.1 Turbulence and CFD Modelling

In order to explain the technical aspects involved in the area of computational fluid dynamics (CFD), and also to highlight the differences among the major modelling strategies, a typical 1-dimensional (1-D) energy spectrum for a turbulent flow is shown in Fig. 1.1. In the figure, $E(\kappa)$ denotes the turbulence kinetic energy (TKE) distribution function per unit mass for a certain wavenumber κ.

As shown in Fig. 1.1, three principal subranges can be identified, including energy containing subrange, inertial subrange, and viscous dissipation subrange. Energy containing subrange is where larger scales of turbulent motions exist. Turbulence is strongly driven by these large eddies. A length scale ℓ characteristic of the larger eddies is known as integral length scale, which is the primary length scale that most turbulence models are based on. Dissipation subrange is where the TKE is dissipated by smaller scales through viscous effects. The motion at the smallest scale of turbulence has the Kolmogorov length scale η, which is defined as $\eta = (\nu^3/\varepsilon)^{1/4}$, where ν is the kinematic viscosity and ε is the dissipation rate. The inertial subrange, lying between the energy containing range and dissipation range, plays a role on transferring energy to smaller scales successively from the larger energetic scales. As shown in Fig. 1.1, the inertial subrange is governed by the $K41$ theory and $-\frac{5}{3}$ law given as

$$E(\kappa) = C_K \varepsilon^{2/3} \kappa^{-5/3} \quad \text{for} \quad \frac{1}{\ell} \ll \kappa \ll \frac{1}{\eta} \quad , \tag{1.1}$$

where C_K is the Kolmogorov constant. Kolmogorov's universal equilibrium theory (cf. Pope [3]) states that only the energetic scales are strongly affected by the initial

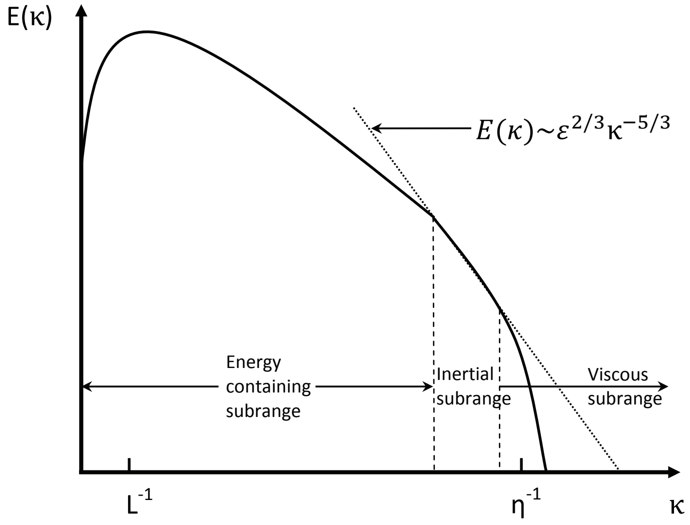

FIGURE 1.1: Energy spectrum for a turbulent flow with log-log scales. The figure is replotted following Wilcox [1].

and boundary conditions (i.e., dependent on the particular flow), whereas the scales with negligible energy are assumed to be approximately universal (i.e., similar in every flow). The dissipation subrange and inertial subrange are where the universal equilibrium is achieved, that is, the smaller eddies are in a state where the rate of receiving energy from the larger eddies is almost equal to the rate at which the smallest eddies dissipate the energy into heat. As pointed out by Wilcox [1], the inertial subrange governed by Eq. (1.1) is critically important for defining different numerical approaches, based on whether turbulence motions in this subrange are directly resolved or modelled.

In a DNS approach, all scales of turbulent motion from the largest integral scale to the dissipative scales of order η are resolved. Because turbulence modelling is not involved, a properly performed DNS simulation represents the turbulence very accurately. The computational cost, however, is dependent on the Reynolds number Re. It is required that in the DNS approach, the computational domain must be significantly larger than the integral scale ℓ, on the other hand, the grid size must be fine enough to capture flow motions at Kolmogorov scale η. To satisfy this requirement, the number of grid points needed along one direction is proportional to the ratio of the length scales ℓ/η. According to Tennekes and Lumley [4], this ratio is proportional to

$Re_\ell^{3/4}$. As such, the number of grid points needed to perform a 3-dimensional (3-D) DNS is proportional to $Re_\ell^{9/4}$. Here, Re_ℓ is the Reynolds number based on the integral scale ℓ. For example, it took 120 days for Hoyas and Jiménez [5] to conduct the DNS study on a fully-developed plane channel flow at $Re_\tau = 2003$ (based on the friction velocity u_τ and half channel height δ), using approximately 18 billion grid points and 2048 processors. Most of their computational effort was devoted to resolving the scale of motions in the inertial and dissipative subranges (i.e., the approximately universal scales).

In contrast to the DNS approach, all scales of turbulence motions are modelled in the RANS equations. In a RANS approach, as the transport equations are ensemble averaged and only mean flow statistics are calculated, the computational cost is much lower than that of DNS. Furthermore, the required number of grid points for the RANS approach becomes almost independent (or weakly dependent) of the Reynolds number. Because the effects of the flow dependent scales (i.e., large energy-containing scales) are modelled, a large variety of RANS closure models are introduced for simulating turbulent flows, ranging from the simplest mixing-length model, to the classical two-equation k-ε model and its extended versions, and to the complex second-order Reynolds stress model. These RANS closure models are well reviewed and documented in literature such as Wilcox [1] and Pope [3].

As an alternative CFD tool, LES is suitable for transient simulation of turbulent flows. The underlying concept of LES method is a direct application of Fig. 1.1. The energetic, flow dependent scales are resolved directly (without modelling), while smaller (subgrid) scales are modelled. This implies that in comparison with RANS, LES can provide more accurate spatial and temporal predictions of a turbulent flow. In the context of homogeneous isotropic turbulence, the computational cost of LES becomes independent of the Reynolds number, since the directly computed (or resolved) scales are inviscid and hence independent of Re. Studies over the last few decades have largely shown LES to live up to these promises for free shear flows, such as jets, mixing layers, and wakes. For wall-bounded turbulent flows, however, the

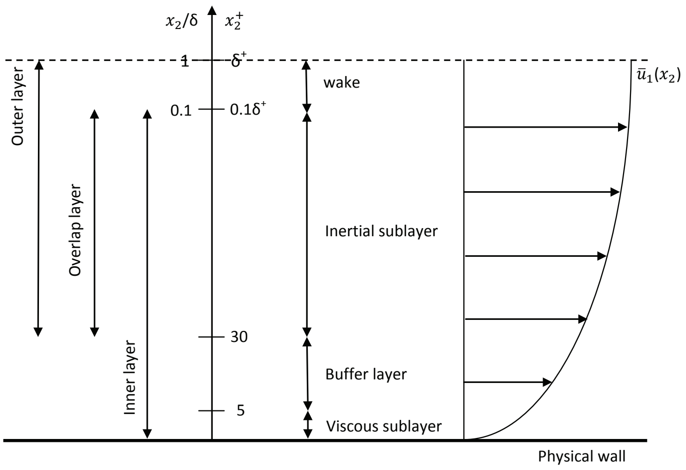

FIGURE 1.2: Schematic of the boundary layer in a turbulent plane channel flow at a high Reynolds number. The figure is replotted following Wosnik *et al.* [2].

results are much less encouraging. The challenges involved in LES of wall-bounded turbulent flows can be explained using the schematic of a boundary layer illustrated in Fig. 1.2. In the near wall region, the flow is dominated by viscous forces, and the relevant length and velocity scales for the turbulence are the distance from the wall x_2 and the friction velocity u_τ, respectively. The characteristic length scale is ν/u_τ. With this viscous length scale, the so-called wall coordinate (or, inner coordinate) $x_2^+ = x_2 u_\tau/\nu$ can be defined, which is essentially a local Reynolds number. Near the wall for $x_2/\delta \leq 0.1$, viscous forces dominate inertial forces, and the flow layer is typically referred to as 'inner layer' (cf. Wosnik *et al.* [2]). However, inertial forces become dominant and the effects of viscosity become relatively small for $x_2^+ \geq 30$, which corresponds to the so-called 'outer layer'.

In the overlap region, the size of the energetic eddies scales with the wall distance x_2, while the size of the dissipative eddies scales with η. The Kolmogorov scale η grows very slowly with the wall distance as a function of $x_2^{1/4}$ (cf. Pope [3]), therefore, the ratio of these two length scales x_2/η depends strongly on x_2 as a function of $x_2^{3/4}$, implying that the dissipative and energetic scales of motions approach each other as the wall is approached. Near the wall, the energetic dynamically important scales are no longer 'large', and the interpretation of LES is ambiguous [6]. As a consequence, viscous scales in the near-wall region must be directly resolved by LES. Following the study of Chapman [7], Larsson [6] estimated that the computational cost for LES to resolve the viscous sublayer is almost as high as that for DNS in the context of a fully-developed plane channel flow.

1.2 Hybrid RANS/LES

1.2.1 Formulation and Mechanism

The challenge that wall resolved LES is not computationally affordable on wall-bounded turbulent flows at high Reynolds numbers triggered the invention of hybrid RANS/LES. The terminology 'hybrid RANS/LES' refers to a large number of similar methods which combine both LES and RANS approaches in numerical simulations, and have been thoroughly reviewed in Fröhlich and von Terzi [8]. The classification of these methods is based on distinguishing segregated models from unified models, and interfacing from blending. According to their variability in time, interfaces are furthermore classified as either soft or hard.

One of the most popular hybrid approaches is the so-called detached-eddy simulation (DES), which was originally introduced by Spalart *et al.* [9]. The DES method is an unified RANS/LES approach with a hard interface where the length scale switches between the RANS and LES models. Another method to unify RANS and LES with a hard interface is the so-called layering RANS/LES approach. Fig. 1.3 shows the schematic of how to layer RANS and LES to the simulation of a turbulent plane channel flow. As demonstrated in the figure, in a layering approach, the computational domain is divided into distinct RANS and LES zones, in which the conventional turbulence models and subgrid-scale (SGS) stress models are used for closure of the governing equations, respectively. The flow fields from the two modelling approaches (i.e., RANS and LES) mutually influence each other through the interface between the RANS zone and LES zone. The interface location that separates the two zones can be explicitly specified by a given wall-normal distance [10, 11] or dynamically determined as the minimum of the RANS length scale (an integral length scale) and

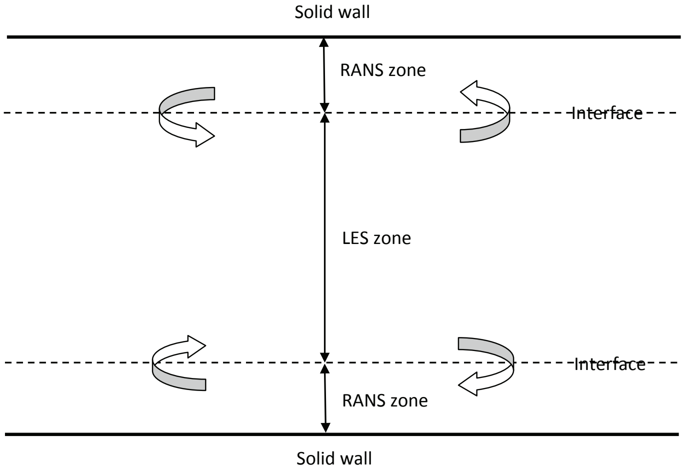

FIGURE 1.3: Schematic of application of hybrid RANS/LES (a layering approach) to a turbulent plane channel flow.

the LES length scale (comparable to grid spacing) [12].

The layering RANS/LES approach has been widely used for computing separated flows and shear flows as well. From here on, the word ‘hybrid’ refers to the layering approach without otherwise specifications. Davidson and Peng [10] used a two-equation k-ω model (where k and ω denote the TKE and specific dissipation rate with dimension of inverse time, respectively) in the RANS zone and a one-equation k-ℓ SGS model in the LES zone. They applied their hybrid approach to simulation of turbulent flows in a plane channel and over a 2-dimensional (2-D) hill. Tucker and Davidson [12] studied both plane and ribbed channel flows using an alternative hybrid approach which utilizes the one-equation k-ℓ model in both RANS and LES regions. Other combinations of the turbulence and SGS models for the RANS and LES zones have also been investigated by, e.g. Temmerman *et al.* [11], Hamba [13] and Larsson *et al.* [14], and well summarized in the comprehensive review of Fröhlich and von Terzi [8].

1.2.2 Artificial Buffer Layer

Owing to the different statistical averaging procedures used in the RANS (based on ensemble averaging) and LES (based on low-pass filtering) regions, the spectral properties in the RANS and LES solutions are significantly different. Consequently, there exists an incompatibility in the computed flow properties around the modelling interface in a hybrid approach. The so-called 'artificial buffer layer' [15] forms along the interface where the closure model switches between RANS and LES. The existence of the artificial buffer layer is unphysical, and as a result, in the context of a turbulent plane channel flow, the mean streamwise velocity profile deviates apparently from the log-law of the wall. Baggett [16] performed hybrid simulations of turbulent plane channel flows using the $\overline{v^2}$-f RANS model (where $\overline{v^2}$ and f denote the velocity scale associated with velocity fluctuations normal to streamlines and the elliptic relaxation factor, respectively) of Durbin [17] in the near-wall region. He observed some unphysical streak-like structures in the RANS zone. These unphysical streaks have larger dimensions than physical streaks observed in near-wall turbulent flows. Physical streaks are universal and their characteristic spanwise dimension λ is always the same if expressed in wall units (i.e., $\lambda^+ = \lambda u_\tau/\nu$) and measured immediately off the wall. DNS and laboratory experiments have shown that the value of mean spacing between near-wall streaks is about $\lambda^+ = 100$ [18–22]. The value of λ^+ for unphysical streaks obtained by Baggett [16] in his hybrid approach is about 260. He further indicated that these 'super-streaks' can cause de-correlation between the streamwise and wall-normal velocity fluctuations.

The artificial buffer layer is a rather interesting feature of hybrid RANS/LES, with little dependence upon the details of the specific closure models, interface locations, matching conditions, and grid resolutions. Many studies [11, 15, 23, 24] have been conducted to test the locations of the modelling interface, all resulting in similar velocity shifts from the log-law. It has been solidly proven that as a direct result of the artificial buffer layer, the velocity shift is an intrinsic characteristic of hybrid RANS/LES, which cannot be removed by simply using different matching conditions for the RANS and LES eddy viscosity terms [12] or different turbulence closure models [11, 12, 15]. Furthermore, tests on grid refinements have shown that even after the solution has reached a grid independent state, there still exists a velocity shift [14].

1.2.3 Remedy

Several strategies have been proposed to remove the artificial buffer layer through additional forcing in the momentum equations. The forcing can be either obtained from a stochastic model, or extracted from a reference DNS or wall-resolved LES database of a fully-developed channel flow. Piomelli *et al.* [23] used forcing to account for backscatter, and suggested that it should possess spatial and temporal scales on the order of the grid size and time step, respectively. Their forcing field consisted of essentially white noise, with which, they were able to reduce the velocity shift and had the super-streaks broken up. Batten *et al.* [25] and Davidson and Billson [26] proposed stochastic models that generate forcing fields with predefined spectra of TKE and anisotropy of turbulent stresses. They observed a quicker transition from modelled turbulence in RANS to resolved turbulence in LES and obtained a desirable reduced artificial buffer layer. Larsson *et al.* [14] and Davidson and Dahlström [24] extracted the forcing field from a reference database (based on DNS or high-resolution wall-resolved LES) in order to make the forcing field realistic in flow dynamics (with respect to, e.g. flow structures and eddy motions). With this technique, they were able to minimize the velocity shift to obtain a smaller artificial buffer layer and reduced near-wall super-streaks.

1.2.4 Alternatives to Hybrid RANS/LES

In addition to hybrid RANS/LES, there are other strategies to handle the inner layer in LES of wall-bounded turbulent flows. These strategies are well summarized in Piomelli and Balaras [27] and Piomelli [28]. The two most common strategies are briefly introduced as follows.

The first strategy is to analogously apply wall functions in the RANS approach to LES. This so-called ‘wall-modelling LES approach’ uses algebraic equations (typically derived from the log-law) to relate the wall shear stresses to the velocity profile in the overlapping layer without solving the governing equations [29–32]. However, Nicoud *et al.* [33] indicated that the approximate boundary conditions based on wall functions may not be accurate enough for high Reynolds number flows. Balaras *et al.* [34] and Wang and Moin [35] further confirmed that this approach may perform poorly for separated and non-equilibrium flows in which the mean streamwise velocity profile often deviates from the familiar log-law of the wall characteristic of a regular zero-pressure-gradient turbulent boundary layer.

The second strategy is to use a two-layer modelling approach, which was originally proposed by Balaras and Benocci [36]. This approach solves the LES equations only in the outer layer, and then solves a simplified set of boundary layer equations on a refined auxiliary grid in the inner layer all the way down to the wall. Balaras *et al.* [34] has extensively tested the two-layer modelling approach based on plane channel flows, rotating channel flows, and square duct flows. The two-layer model has also been successfully applied to LES of backward facing step flows by Cabot [37] and Diurno *et al.* [38] and to LES of flows passing a trailing edge by Wang and Moin [35]. Two separate sets of grids are needed in a two-layer modelling approach, and as a consequence, the computational cost increases by 10–15% in comparison with that for the aforementioned wall-modelling LES approaches based on wall functions [34].

1.3 Parallel Computing

To pull a bigger wagon, it is easier to add more oxen than to grow a gigantic ox. Considerations of both peak performance and ratio of price to performance are pushing large-scale computing in the direction of parallelism [39]. Parallel computing is an attempt at simulating phenomena that are too complex to be reliably predicted by theory or too dangerous or expensive to be reproduced in the laboratory.

To parallelize a problem, a suitable decomposition has to be used initially. There are a variety of decomposition methods including functional decomposition and domain decomposition [40]. Functional decomposition divides the problem among processors according to the different operations that will be performed on the data. This type of decomposition is often used to develop codes involving massive computing for large systems, e.g. the computer codes used for climate and weather forecasting. The processors are assigned with different models in the calculation, such as the ocean model, atmospheric model, etc. In comparison the functional decomposition method, the domain decomposition method is more popular in scientific and engineering computing. For a structured finite difference grid, the domain is sliced into structured subdomains (slabs) in a domain decomposition method. Each subdomain (slab) is assigned to a different processor and handled by a different process. Herein, the term 'processor' refers to a piece of hardware containing a central processing unit (CPU) capable of executing a program, and 'process' is a software concept representing an address space and one or more parallelized threads.

When solving systems of linear equations such as the Poisson problem using a domain decomposition, the nodes in each subdomain require data passed across the neighboring subdomain boundaries. In terms of memory access, there are two main parallel programming models for domain decomposition, namely, shared memory model and distributed memory model. For the shared memory model, each processor has an access to all of a single, shared address space at the usual level of loading and storing operations. In contrast, the distributed memory model posits a set of processes that have only local memory but are able to communicate with other processes by sending and receiving messages.

Message Passing Interface (MPI) library standard is a distributed memory model, developed by a committee of parallel computing researchers in universities, government labs and industry. The first version of MPI (MPI-1) was released in 1994 and its second version (MPI-2) was completed in 1998. MPI provides a way for the programmer to explicitly associate specific data with processes and thus allows the compiler and cache-management hardware to function fully. MPI also supports a large variety of programming languages [39], such as FORTRAN, C and C++.

The present CFD code developed for hybrid RANS/LES simulations is fully parallellized using MPI. In order to be compatible with the structured grid system, the domain decomposition method is employed to decompose the computational domain. Due to the use of the distributed memory model, designated MPI routines are carefully chosen to send and receive messages across the subdomain boundaries when governing equations for the turbulent flow are solved by the CFD code.

1.4 Objectives of the Thesis

This research focuses on forcing modelling for hybrid RANS/LES and includes four major objectives:

i) Notwithstanding the achievements in literature, lack of physical justifications due to use of stochastic models and a need of readily available databases for extraction of forcing for hybrid RANS/LES prevent any in-depth understanding of the physics underlying the formation of the artificial buffer layer. In contrast to the previous approaches, this research aims to propose an interesting physics-based dynamic forcing scheme incorporating backscatter obtained from the instantaneous flow field itself.

ii) Furthermore, through analyzing the effects of dynamic forcing on reducing the thickness and impact of the artificial buffer layer in the context of a turbulent plane channel flow, this research also aims to identify the important factors for improving the forcing techniques for hybrid RANS/LES. These factors include grid resolutions, SGS stress models, RANS-LES interface locations, and regions where forcing is applied.

iii) As turbulent flows subjected to spanwise system rotation are often encountered in wall-bounded turbulent flows, the predictive performance of the new dynamic forcing scheme will be assessed by considering a special type of body forces, i.e., the non-inertial and non-conservative Coriolis force. Due to the presence of Coriolis forces, the velocity field becomes statistically asymmetrical in the wall-normal direction. The flow becomes destabilized on the pressure side and stabilized on the suction side of the channel. Correspondingly, the local Reynolds number increases and decreases considerably on the pressure and suction side, respectively. These interesting physical features of the spanwise rotating channel flow impose additional challenges to the test of the forcing scheme for hybrid RANS/LES.

iv) A complex scenario when the turbulent flow subjected to the combined effects of system rotation and rib-roughness will be investigated in order to further evaluate the predictive performance of the novel dynamic forcing scheme. As the Coriolis force significantly influences the stability of the wall shear layer and the free shear layer created by the ribs, it will be interesting to observe whether the classification of the roughness type relies not only on the pitch ratio, but also on the rotation number in the context of rotating rib-roughened flows.

1.5 Outline of the Thesis

The thesis is organized as follows. In chapter 2, the methodology of hybrid RANS/LES will be introduced, including the justification of closure models used in the RANS and LES zones, the treatment of the interface between these two zones, and the novel dynamic forcing scheme proposed for the hybrid approach. The algorithm used for solving the governing equations will also be presented.

In chapter 3, a turbulent plane channel flow will be used to assess the predictive performance of the novel dynamic forcing scheme. Despite its geometrical simplicity, a turbulent plane channel flow is one of the most important benchmark test cases for studying shear flow physics and for examining closure models under wall anisotropy. This chapter will focus on formation and treatment of the artificial buffer layer that develops around the modelling interface. The effects of the dynamic forcing scheme on reducing the thickness and impact of the artificial buffer layer in the hybrid approach will be evaluated. In order to validate the hybrid RANS/LES approach, flow statistics obtained from the simulations will be thoroughly compared against the available DNS data.

In chapter 4, the predictive performance of the dynamic forcing scheme will be examined in the context of a rotating channel flow. In response to the spanwise system rotation, the flow on one side of the channel becomes more turbulent, while the flow on the other side becomes more laminarized. This chapter will focus on whether the proposed hybrid approach is able to reflect this anisotropic effect of the Coriolis force. In order to validate the present hybrid approach, turbulence statistics obtained from the simulations will be thoroughly compared against available experimental and DNS results.

In chapter 5, the effects of system rotation and surface roughness will be investigated by utilizing the hybrid RANS/LES approach based on the novel dynamic forcing scheme. Through the study of rotating rib-roughened channel flows, this chapter will focus on how the flow separation and reattachment phenomena due to the rib-roughness are altered by the imposed system rotation. In order to validate the present hybrid approach, turbulence statistics obtained from the simulations will be thoroughly compared with the available laboratory measurement data of Coletti *et al.* [41–43].

In chapter 6, a summary of the major conclusions of this thesis and a discussion of the research subjects for possible future explorations will be presented.

Chapter 2

Numerical Algorithm

The motion of fluid flow is governed by the continuity and momentum equations. In order to perform hybrid RANS/LES, ensemble averaging and filtering processes need to be applied to the governing equations to conduct RANS and LES, respectively. The turbulence closure problem arises as a result of the ensemble averaging and filtering procedures which lead to an extra stress term (i.e., Reynolds stresses in RANS or SGS stresses in LES). This extra stress term needs to be modelled in order to close the ensemble averaged or filtered momentum governing equations. In this chapter, the closure models for performing hybrid RANS/LES and the algorithm for discretizing the governing equations are described.

2.1 Governing Equations

The governing equations of mass and momentum conservations for an incompressible flow of a Newtonian fluid can be written in Cartesian tensor notation as

$$\frac{\partial u_i}{\partial x_i} = 0 \quad , \tag{2.1}$$

$$\frac{\partial u_i}{\partial t} + \frac{\partial}{\partial x_j}(u_i u_j) = -\frac{1}{\rho}\frac{\partial p}{\partial x_i} + \frac{\partial}{\partial x_j}\left[\nu\left(\frac{\partial u_i}{\partial x_j} + \frac{\partial u_j}{\partial x_i}\right)\right] + 2\varepsilon_{ij3}\Omega u_j \quad , \tag{2.2}$$

where ρ is the density, p is the pressure, ε_{ijk} is the Levi-Civita symbol, and u_i is the velocity component in the x_i-direction. In this thesis, x_1, x_2 and x_3 are used to denote the streamwise, wall-normal and spanwise coordinates, respectively. The summation convention applies to repeated indices in each term. The last term on the right-hand-side (RHS) of Eq. (2.2) represents the Coriolis force term if under spanwise system rotation at a rotating speed Ω.

When an ensemble averaging (or filtering) operation is applied, an instantaneous flow variable ϕ can be decomposed as

$$\phi = \bar{\phi} + \phi' \quad , \tag{2.3}$$

where $\bar{\phi}$ is the averaged (or filtered) component of ϕ that can be directly resolved, and ϕ' is the residual component. By applying the ensemble averaging (or filtering) procedure to Eqs. (2.1) and (2.2), the set of governing equations for performing hybrid RANS/LES become

$$\frac{\partial \bar{u}_i}{\partial x_i} = 0 \quad , \tag{2.4}$$

$$\frac{\partial \bar{u}_i}{\partial t} + \frac{\partial}{\partial x_j}(\bar{u}_i \bar{u}_j) = -\frac{1}{\rho}\frac{\partial \bar{p}}{\partial x_i} + \frac{\partial}{\partial x_j}\left(2\nu \bar{S}_{ij} - \tau_{ij}\right) + 2\varepsilon_{ij3}\Omega \bar{u}_j \quad , \tag{2.5}$$

where $\bar{S}_{ij} \overset{\text{def}}{=} (\partial \bar{u}_i/\partial x_j + \partial \bar{u}_j/\partial x_i)/2$ is the mean (or resolved) strain rate tensor, and the overbar '-' denotes the ensemble averaging operator for RANS or filtering operator for LES. As a consequence of the ensemble averaging or filtering process, an extra turbulent stress tensor τ_{ij} appears in the momentum equation, which is known as the Reynolds stress tensor in a RANS approach, defined as

$$\tau_{ij} = \overline{u_i' u_j'} \quad , \tag{2.6}$$

and as the SGS stress tensor in a LES approach, defined as

$$\tau_{ij} = \overline{u_i u_j} - \bar{u}_i \bar{u}_j \quad . \tag{2.7}$$

The turbulent stress term τ_{ij} needs to be modelled in order to close the above system of governing equations.

2.2 Hybrid RANS/LES Methodology

The hybrid approach consists of using a Reynolds stress model and a SGS stress model in the RANS and LES zones, respectively. In the following context, the closure models used in this research will be thoroughly described.

2.2.1 Reynolds Stress Model for RANS

The idea of Reynolds averaging is to decompose an instantaneous flow field into ensemble-averaged mean velocity and fluctuating velocity fields. Accordingly, in a RANS approach, only the mean flow properties are computed, whereas all scales of turbulent fluctuations are modelled. In this research, the mean value $\bar{\phi}$ is obtained through time averaging as

$$\bar{\phi}(x_i) = \lim_{T \to +\infty} \frac{1}{T} \int_0^T \phi(x_i, t) dt \quad , \tag{2.8}$$

where T is the averaging time interval.

The classical approach to model Reynolds stress term in Eq. (2.6) is to adopt the eddy viscosity concept based on Boussinesq approximation, which assumes

$$\tau_{ij} = \frac{2}{3} k^R \delta_{ij} - 2\nu_t^R \bar{S}_{ij} \quad , \tag{2.9}$$

where $k^R = \overline{u_i' u_i'}/2$ represents the TKE, δ_{ij} is the Kronecker delta, and ν_t^R is the eddy viscosity for RANS. In the above equation, superscript R is used to denote quantities related to the RANS approach. Analogous to the effect of molecular viscosity in the molecular diffusion of momentum, the eddy viscosity characterizes the effect of turbulent eddies on the transport and mixing of momentum in the flow. In the inner layer, the mixing length model with wall damping function [3] is used for the hybrid approach in this thesis, viz.

$$\nu_t^R = \kappa u_\tau x_2 D \quad , \tag{2.10}$$

where κ=0.41 is the von Kármán constant, and the wall damping function is given by

$$D = \left[1 - \exp\left(-\frac{x_2^+}{19}\right)\right]^2 \quad . \tag{2.11}$$

2.2.2 SGS Stress Model for LES

In LES, large and small scales of flow motion can be distinguished using a filtering operation. A filtered variable, denoted by an overbar, is defined as

$$\bar{\phi}(x_i, t) = \int \phi(x_i', t) G(x_i - x_i', \bar{\Delta}) dx_i' \quad , \tag{2.12}$$

where $G(x_i - x_i', \bar{\Delta})$ is the filter function and $\bar{\Delta}$ denotes the grid-level filter width. The Gaussian filter is reasonably compact both in physical and wavenumber spaces, and its filter function is expressed as

$$G(x_i - x_i', \bar{\Delta}) = \sqrt{\frac{6}{\pi \bar{\Delta}^2}} \exp\left(-\frac{6(x_i - x_i')^2}{\bar{\Delta}^2}\right) \quad . \tag{2.13}$$

In the dynamic SGS modelling approach, an explicit discrete filter is required for performing the test-grid level filtering process. The discrete Gaussian filters introduced by Sagaut and Grohens [44] are used for this purpose throughout this thesis. A 3-D filtering procedure can be constructed using a linear combination of 1-D discrete filters as

$$\tilde{\phi}(I, J, K) = \frac{1}{3} \sum_{l=-N}^{N} a_l \left[\phi(I + l, J, K) + \phi(I, J + l, K) + \phi(I, J, K + l)\right] \quad , \tag{2.14}$$

where $N = 1$ for a three-point stencil (2nd-order accuracy) and $N = 2$ for a five-point stencil (4th-order accuracy), and a_l represents the filter coefficients for the 1-D discrete filter.

In the LES zone of the hybrid approach, without an otherwise specification, the boundary field is processed using a 2nd-order discrete Gaussian filter, while the internal field is processed with a 4th-order discrete Gaussian filter. The 1-D discrete forms for the 2nd- and 4th-order Gaussian filters given by Sagaut and Grohens [44] are, respectively,

$$\tilde{\phi}(I) = \frac{1}{24}\epsilon^2 \left[\phi(I+1) + \phi(I-1)\right] + \frac{1}{12}(12 - \epsilon^2)\phi(I) \quad , \tag{2.15}$$

and

$$\begin{aligned}\tilde{\phi}(I) =& \frac{16\epsilon^2 - \epsilon^4}{288}\left[\phi(I+1) + \phi(I-1)\right] + \frac{\epsilon^4 - 20\epsilon^2 + 192}{192}\phi(I) \\ &+ \frac{\epsilon^4 - 4\epsilon^2}{1152}\left[\phi(I+2) + \phi(I-2)\right] \quad .\end{aligned} \tag{2.16}$$

Here, $\epsilon = \tilde{\bar{\Delta}}/\bar{\Delta}$ represents the ratio between the cutoff sizes of the test-grid and grid filters, which is set to $\epsilon = 2$ following the conventional approach [45]. It is interesting to observe that with the choice of $\epsilon = 2$, the discrete filtering scheme of 2nd-order accuracy (i.e., Eq. (2.15)) becomes identical to that of 4th-order accuracy (i.e., Eq. (2.16)).

The SGS stress term τ_{ij} defined in Eq. (2.7) represents the SGS momentum fluxes caused by the small (unresolved) scales of motion in the turbulent flow. Analogous to Eq. (2.9) for the RANS approach, the SGS stress tensor can be modelled as:

$$\tau_{ij} = \frac{2}{3}k^L\delta_{ij} - 2\nu_t^L\bar{S}_{ij} \quad , \tag{2.17}$$

where $k^L = \tau_{ii}/2$ is the modelled SGS KE, and ν_t^L is the eddy viscosity for LES.

In the outer layer, both the Smagorinsky model (SM) [46] and the dynamic Smagorinsky model (DSM) [47] are tested for the hybrid approach in this thesis. In the SM and DSM, the eddy viscosity (or, SGS viscosity) is determined as

$$\nu_t^L = C_S\bar{\Delta}^2|\bar{S}| \quad , \tag{2.18}$$

where $\bar{\Delta}$ is the grid-level filter size, $|\bar{S}| = (2\bar{S}_{ij}\bar{S}_{ij})^{1/2}$ is the norm of the resolved strain rate tensor $\bar{S}_{ij}$. The value of C_S is fixed to $C_S = 0.0042$ in the SM. In the DSM of Lilly [47], the optimal coefficient C_S can be obtained using the least squares method, viz.

$$C_S = -\frac{M_{ij}\mathcal{L}_{ij}}{M_{ij}M_{ij}} \quad , \tag{2.19}$$

where $\mathcal{L}_{ij}$ is the resolved Leonard type stress defined as $\mathcal{L}_{ij} \overset{\text{def}}{=} \widetilde{\bar{u}_i\bar{u}_j} - \tilde{\bar{u}}_i\tilde{\bar{u}}_j$, and $M_{ij} \overset{\text{def}}{=} \alpha_{ij} - \tilde{\beta}_{ij}$ is a differential tensor. Here, $\alpha_{ij} \overset{\text{def}}{=} 2\tilde{\bar{\Delta}}^2|\tilde{\bar{S}}|\tilde{\bar{S}}_{ij}$ and $\beta_{ij} \overset{\text{def}}{=} 2\bar{\Delta}^2|\bar{S}|\bar{S}_{ij}$ are base stress tensors at the test-grid and grid levels, respectively. In LES, the resolved or filtered quantities at the grid level are denoted using an overbar, while quantities filtered at the test-grid level for the dynamic procedure are denoted using a tilde.

2.2.3 Dynamic Forcing

By replacing τ_{ij} in Eq. (2.5) using Eq. (2.9) for RANS or Eq. (2.17) for LES, and by including a forcing term $\mathcal{F}_i$, the momentum equations for performing hybrid RANS/LES take the following form:

$$\frac{\partial \bar{u}_i}{\partial t} + \frac{\partial}{\partial x_j}(\bar{u}_i\bar{u}_j) = -\frac{1}{\rho}\frac{\partial \bar{p}}{\partial x_i} + \frac{\partial}{\partial x_j}\left[(\nu + \nu_t)\frac{\partial \bar{u}_i}{\partial x_j}\right] + 2\varepsilon_{ij3}\Omega\bar{u}_j + \mathcal{F}_i \quad , \tag{2.20}$$

where $\bar{p}$ herein represents the effective pressure combined with the imposed mean pressure gradient along the streamwise direction and the isotropic part of the Reynolds stress tensor for RANS (cf. Eq. (2.9)) or SGS stress tensor for LES (cf. Eq. (2.17)). The eddy viscosity ν_t can be either ν_t^R in RANS region or ν_t^L in LES region.

The forcing term $\mathcal{F}_i$ in Eq. (2.20) for hybrid RANS/LES considered in this thesis is modelled as:

$$\mathcal{F}_i = -\frac{\partial \tau_{ij}^B}{\partial x_j} \quad , \tag{2.21}$$

where τ_{ij}^B denotes the forcing stress tensor which can account for backscatter in the proposed modelling approach for forcing. In order to implement a forcing scheme in a hybrid RANS/LES approach, it is essential to understand to which length scale the forcing should be applied. Since backscatter is a direct result of the interactions between the resolved and subgrid scale motions, the length scale is chosen to be the grid level filter width, which overlaps the nodal distance of the grid system in a conventional LES approach.

In this research, the forcing stress tensor τ_{ij}^B proposed for hybrid RASN/LES is modelled as

$$\tau_{ij}^B = -C_W \gamma_{ij} - C_N \eta_{ij} \quad , \tag{2.22}$$

where γ_{ij} and η_{ij} represent two quadratic base tensor functions defined as $\gamma_{ij} \overset{\text{def}}{=} 4\bar{\Delta}^2(\bar{S}_{ik}\bar{\Omega}_{kj} + \bar{S}_{jk}\bar{\Omega}_{ki})$ and $\eta_{ij} \overset{\text{def}}{=} 4\bar{\Delta}^2(\bar{S}_{ik}\bar{S}_{kj} - \bar{S}_{mn}\bar{S}_{nm}\delta_{ij}/3)$, respectively; and, $\bar{\Omega}_{ij} \overset{\text{def}}{=} (\partial\bar{u}_i/\partial x_j - \partial\bar{u}_j/\partial x_i)/2$ is the resolved rotation rate tensor. The first term γ_{ij} in Eq. (2.22) does not make any contribution to the KE transfer between the resolved and subgrid scales, but according to a recent systematic *a priori* LES study of Horiuti [48], it significantly improves the correlation between the exact SGS stress extracted from a DNS database and that predicted by LES. As demonstrated in previous full LES studies [49–51], it is the second term η_{ij} that contributes significantly to the backscatter of KE from the subgrid to the resolved scales. The forcing model represented by Eq. (2.22) will be tested in the context of plane channel flows (in chapter 3) and rotating channel flows (in chapter 4). Later in chaper 5, an alternative forcing model simplified from Eq. (2.22) will be tested in the context of rib-roughened channel flows with and without system rotations.

In the following context, the concept of 'dynamic forcing' is further introduced so that the forcing stress tensor τ_{ij}^B in Eq. (2.22) (including its two model coefficients C_W and C_N) can be entirely dynamically determined using the local instantaneous flow field at each time step. The characteristic spatial and temporal scales at which the present dynamic forcing scheme is applied coincide with the filter size and simulation time step, respectively. This is similar to the modelling approach of Piomelli *et al.* [23], who also used the filter width and time step as the spatial and temporal scales in their stochastic forcing model.

Similar to the proposed forcing stress model at the grid level (i.e., Eq. (2.22)), the forcing stress tensor at the test-grid level can be modelled as:

$$T_{ij}^{B} = -C_W \lambda_{ij} - C_N \zeta_{ij} \quad , \tag{2.23}$$

where $\lambda_{ij} \overset{\text{def}}{=} 4\tilde{\bar{\Delta}}^2(\tilde{\bar{S}}_{ik}\tilde{\bar{\Omega}}_{kj} + \tilde{\bar{S}}_{jk}\tilde{\bar{\Omega}}_{ki})$ and $\zeta_{ij} \overset{\text{def}}{=} 4\tilde{\bar{\Delta}}^2(\tilde{\bar{S}}_{ik}\tilde{\bar{S}}_{kj} - \tilde{\bar{S}}_{mn}\tilde{\bar{S}}_{nm}\delta_{ij}/3)$.

In order to determine the two coefficients, it is assumed that Germano identity [45] holds in the dynamic procedure, which follows

$$\mathcal{L}_{ij} = T_{ij}^{B} - \widetilde{\tau_{ij}^{B}} \quad . \tag{2.24}$$

It can be shown that the values of the two coefficients C_W and C_N in Eq. (2.22) can be obtained by minimizing the residual of the Germano identity following the conventional dynamic procedure [47], viz.

$$\begin{bmatrix} W_{ij}W_{ij} & W_{ij}N_{ij} \\ N_{ij}W_{ij} & N_{ij}N_{ij} \end{bmatrix} \cdot \begin{bmatrix} C_W \\ C_N \end{bmatrix} = - \begin{bmatrix} \mathcal{L}_{ij}^{*}W_{ij} \\ \mathcal{L}_{ij}^{*}N_{ij} \end{bmatrix} \quad , \tag{2.25}$$

where $\mathcal{L}_{ij}^{*} = \mathcal{L}_{ij} - \mathcal{L}_{kk}\delta_{ij}/3$ is the trace-free form of $\mathcal{L}_{ij}$, and $W_{ij} \overset{\text{def}}{=} \lambda_{ij} - \tilde{\gamma}_{ij}$ and $N_{ij} \overset{\text{def}}{=} \zeta_{ij} - \tilde{\eta}_{ij}$ are two differential tensors.

2.2.4 Justification for the Closure Models

The hybrid RANS/LES approach proposed in this thesis uses the combination of algebraic closure models (represented by Eqs. (2.10) and (2.18)) and the dynamic forcing scheme (represented by Eq. (2.22)). The model testing strategy is similar to that of Larsson *et al.* [14], who used the algebraic model for the RANS region to test their hybrid approach. The strategy also agrees with the philosophy of two-layer wall-modelling LES approach reviewed by Piomelli and Balaras [27], where boundary-layer equations in the inner layer are solved for computing separating/reattaching flows based on the algebraic eddy viscosity model. Furthermore, Temmerman *et al.* [11], Hamba [13], Nikitin *et al.* [15] and Davidson and Dahlström [24] have obtained qualitatively similar results using a variety of eddy viscosity type turbulence closure models in their hybrid RANS/LES of turbulent plane channel flows. It was concluded from their studies that the existence of artificial buffer layer depends little upon the details of the closure models. Based on this conclusion, the hybrid RANS/LES approach considered in this thesis uses simple algebraic models for closure of the governing equations, and focuses on testing the dynamic forcing scheme to tackle directly the challenges from the velocity shift and artificial buffer layer. As such, the RANS model in Eq. (2.10) serves as a stable testing platform to this objective.

At the interface, the turbulence modelling approach switches from RANS to LES and the flow fields obtained from these two modelling approaches mutually influence each other. The interface location that separates the RANS and LES zones can be explicitly specified using a given wall-normal distance [10, 11], or dynamically determined as the minimum of the RANS length scale (based on an integral length scale) and the LES length scale (based on the filter size) [12]. Both approaches are practical and effective in defining the interface location, and both have little influence on the thickness of the artificial buffer layer [14]. In this research, the first approach [10,11] is adopted to specify the interface at a given wall-normal location.

In order to match the values of ν_t^R and ν_t^L at the interface of the RANS and LES zones, Temmerman *et al.* [11] and Nikitin *et al.* [15] enforced continuity of ν_t, whereas Larsson *et al.* [14] and Baggett [16] used blending functions. However, the results of these researchers are similar to those of Davidson and Peng [10] whose hybrid approach is free from any special treatment for ν_t. Because the exact matching conditions appear to have a marginal effect on the appearance of an artificial buffer layer, the approach of Davidson and Peng [10] is adopted and ν_t is neither enforced nor blended in this research.

2.2.5 Rationale for Use of Backscatter in Forcing

In LES, the SGS dissipation rate represents local KE transfer between the resolved and unresolved (subgrid) scales through an inertial and inviscid process. It represents the rate of KE production and functions as a source of KE for the residual SGS motions and a sink of KE for the large resolved scale motions. The instantaneous value of the SGS dissipation rate can be either positive or negative, representing a local forward or backward transfer of KE between the resolved and subgrid scales, respectively.

The proposed dynamic forcing scheme is associated with the following production term:

$$P_r^B = -\tau_{ij}^B \bar{S}_{ij} \quad . \tag{2.26}$$

Substituting Eq. (2.22) into Eq. (2.26), the following equation is obtained for evaluating P_r^B

$$P_r^B = C_W \gamma_{ij} \bar{S}_{ij} + C_N \eta_{ij} \bar{S}_{ij} \quad . \tag{2.27}$$

According to Wang and Bergstrom [49], in the above equation, the second term (i.e., $C_N \eta_{ij} \bar{S}_{ij}$) plays a pivotal role in the local KE backscatter, however the first term is zero (i.e., $C_W \gamma_{ij} \bar{S}_{ij} \equiv 0$) because γ_{ij} is an anti-symmetrical tensor and $\bar{S}_{ij}$ is a symmetrical tensor.

The proposed forcing scheme is inspired by the work of Davidson [52], who proposed a forcing scheme by adding the gradient of SGS stresses to the momentum equations. In the approach of Davidson [52], the forcing stress term τ_{ij}^B is extracted from a scale-similarity SGS model, and a sign function is defined to ensure that only the part of the SGS stress that can produce backscatter effects is used as forcing for hybrid RANS/LES. Different from the method of Davidson [52], the forcing stress tensor model proposed in Eq. (2.22) does not rely on the scale-similarity SGS model; instead, it stems from the dynamic nonlinear model of Wang and Bergstrom [49]. It is worthwhile to note that backscatter plays an important role in LES of wall-bounded turbulent flows, as pointed out by Völker *et al.* [53] and Bhattacharya *et al.* [54], the modelling of near-wall region must reflect such backward scatter of the local KE. Furthermore, according to Davidson [52], the ability of a forcing model to generate backscatter of KE is essential for performing transient simulation of turbulence in the LES region.

The stress tensor τ_{ij}^B can be also viewed as a modelling for the 'Germano stress-like term', which appears in the 'universal SGS stress' due to the hybrid filtering process proposed by Germano [55]. In Germano's approach [55], the hybrid filtering technique is based on blending filters, rather than blending RANS and LES closure models as suggested by Baggett [16]. By examining Germano's approach, Rajamani and Kim [56] demonstrated that it would be essential for hybrid RANS/LES to have a Germano stress-like term in the modelled stress in order to reach the proper level of total stresses. Furthermore, they confirmed that the proper energy transfer between RANS and LES regions is the key to successful hybrid models. However, as pointed out by Rajamani and Kim [56], the exact computation of Germano stress-like term has raised numerical difficulties in simulating a turbulent plane channel flow. Based on their observation, it would be more difficult to exactly compute the German stress-like term in studying wall-bounded turbulent flows subjected to effects of system rotation and surface roughness. A convenient way to handle the Germano-like term is to model this term as forcing in momentum equations.

2.3 Algorithm

In this thesis, a 3-D in-house CFD code has been developed to perform hybrid RANS/LES simulations of wall-bounded turbulent flows. The code is written using FORTRAN 90/95 programming language and fully parallelized using MPI library. It is modified from an existing computer code originally developed by LePoudre [57]. The original computer code is based on a staggered grid system for computing lid driven cavity laminar flows. In order to conduct the current hybrid RANS/LES, the code has been significantly modified based on a collocated grid arrangement and new implementations of closure models. In a collocated grid system, the information on both the velocity and the pressure field is stored at the center of the grid, and the velocities at the interface of a control volume are approximated by the interpolation of neighboring nodal velocities stored at the center of the grid. All hybrid simulations are conducted on WestGrid (a multi-cluster high performance computing consortium encompassing 14 major partner institutions in Western Canada).

A finite volume method was applied to the discretization of the governing equations. The Navier-Stokes equations were advanced in time using a fractional step method, which has been commonly used to obtain solutions of the unsteady Navier-Stokes equations. Different versions of fractional step method have been developed in literature, e.g., the semi-implicit method of Kim and Moin [58] and fully implicit method of Choi and Moin [59]. In this thesis, the latter suggested by Choi and Moin [59] (also presented in Ferziger and Perić [60]) was applied to solve the ensemble averaged (or filtered) Navier-Stokes equations using four steps.

At the first step, an intermediate velocity $\bar{u}_i^{(\star)}$ is obtained from the momentum equations using pressure from the previous time step

$$\frac{\bar{u}_i^{(\star)} - \bar{u}_i^{(n)}}{\Delta t} + \frac{1}{\rho}\frac{\partial \bar{p}^{(n)}}{\partial x_i} + \frac{\partial \tau_{ij}^{(n)}}{\partial x_j} - 2\varepsilon_{ij3}\Omega \bar{u}_j^{(n)} + \frac{\partial \tau_{ij}^{B(n)}}{\partial x_j} + \mathcal{H}_i = 0 \quad , \tag{2.28}$$

where $\mathcal{H}_i$ is the convective and diffusive terms, which is expressed as

$$\mathcal{H}_i = \frac{1}{4}\frac{\partial \left\{ \left[\bar{u}_j^{(\star)} + \bar{u}_j^{(n)}\right] \left[\bar{u}_i^{(\star)} + \bar{u}_i^{(n)}\right] \right\}}{\partial x_j} - \frac{\nu}{2}\frac{\partial^2 \left[\bar{u}_i^{(\star)} + \bar{u}_i^{(n)}\right]}{\partial x_j \partial x_j} \quad . \tag{2.29}$$

At the second step, the intermediate field $\bar{u}_i^{(\star)}$ is modified to a second intermediate field by removing half of the old pressure gradient

$$\frac{\bar{u}_i^{(\star\star)} - \bar{u}_i^{(\star)}}{\Delta t} = \frac{1}{2\rho}\frac{\partial \bar{p}^{(n)}}{\partial x_i} \quad , \tag{2.30}$$

then, the velocity at time level (n+1) is approximated as

$$\frac{\bar{u}_i^{(n+1)} - \bar{u}_i^{(\star\star)}}{\Delta t} = -\frac{1}{2\rho}\frac{\partial \bar{p}^{(n+1)}}{\partial x_i} \quad . \tag{2.31}$$

The Crank-Nicolson scheme which requires a contribution of half of the new pressure is applied in Eq. (2.31). Superscripts (n) and $(n+1)$ indicate the current and following time step, respectively; and superscripts $(\star)$ and $(\star\star)$ indicate a first and second estimated intermediate value in between the current and following time step, respectively. Adding Eqs. (2.28) (2.30) and (2.31) gives

$$\frac{\bar{u}_i^{(n+1)}-\bar{u}_i^{(n)}}{\Delta t}+\frac{1}{2\rho}\frac{\partial\left[\bar{p}^{(n)}+\bar{p}^{(n+1)}\right]}{\partial x_i}+\frac{\partial \tau_{ij}^{(n)}}{\partial x_j}-2\varepsilon_{ij3}\Omega\bar{u}_j^{(n)}+\frac{\partial \tau_{ij}^{B(n)}}{\partial x_j}+\mathcal{H}_i=0 \quad . \tag{2.32}$$

The splitting error associated with the fractional step method is a result of $\bar{u}_i^{(\star)}$ appearing in the convective and diffusive terms (i.e., $\mathcal{H}_i$) instead of $\bar{u}_i^{(n+1)}$. By adding Eqs. (2.30) and (2.31), it is easy to show that this error is second order in time

$$\bar{u}_i^{(n+1)}-\bar{u}_i^{(\star)}=-\frac{\Delta t}{2\rho}\frac{\partial\left[\bar{p}^{(n+1)}-\bar{p}^{(n)}\right]}{\partial x_i}\approx-\frac{(\Delta t)^2}{2\rho}\frac{\partial}{\partial x_i}\left(\frac{\partial \bar{p}}{\partial t}\right) \quad , \tag{2.33}$$

and therefore this error is of the same order as the truncation error in the Crank-Nicolson scheme. The fact that $\bar{u}_i^{(\star)}$ is a second-order approximation to $\bar{u}_i^{(n+1)}$ means that $\bar{u}_i^{(n+1)}$ boundary conditions can be used for Eq. (2.28) with no loss of overall accuracy [59].

Taking the divergence of Eq. (2.31) results in a Poisson equation for the pressure $\bar{p}^{(n+1)}$:

$$\frac{\partial^2 \bar{p}^{(n+1)}}{\partial x_i \partial x_i}=\frac{2\rho}{\Delta t}\frac{\partial \bar{u}_i^{(\star\star)}}{\partial x_i} \quad , \tag{2.34}$$

because the velocity at time level (n+1) satisfies continuity, therefore

$$\frac{\partial \bar{u}_i^{(n+1)}}{\partial x_i}=0 \quad . \tag{2.35}$$

For collocated grids, control volumes are extended to the boundary and the boundary pressure is required to calculate the pressure forces in momentum equations. In this thesis, the linear extrapolation with second-order accuracy was used to specify pressure at the boundary of the computational domain.

The above fractional step method was implemented in the code as follows. The first intermediate field $\bar{u}_i^{(\star)}$ was solved using Eq. (2.28) based on the previous fields $\bar{u}_i^{(n)}$ and $\bar{p}^{(n)}$, or an initial guess. The second intermediate field $\bar{u}_i^{(\star\star)}$ was calculated from $\bar{u}_i^{(\star)}$ using Eq. (2.30). Then, the $\bar{u}_i^{(\star\star)}$ field was used to construct the source term of Eq. (2.34), which was solved for the new pressure field $\bar{p}^{(n+1)}$ using a 4-level V-cycle based multi-grid method. The $\bar{u}_i^{(\star\star)}$ field was then updated to obtain the new divergence free velocity field $\bar{u}_i^{(n+1)}$ using Eq. (2.31). The convergence criterion for solving momentum and continuity equations was set to 10^{-6}, and the Courant-Friedrichs-Lewy (CFL) number was ensured to be less than 0.35. Details regarding the discretization for the momentum and continuity equations based on the fractional step method are summarized in the Appendix A in this thesis.

Chapter 3

Hybrid RANS/LES of Turbulent Flow in a Plane Channel

In this chapter, the dynamic forcing scheme incorporating backscatter (represented by Eq. (2.22)) is tested in the context of turbulent plane channel flows with two Reynolds numbers $Re_\tau = 650$ and 1020. Furthermore, transport equations for the resolved turbulent stresses and TKE are introduced to investigate the effects of dynamic forcing on reduction of the thickness and impact of the artificial buffer layer. In order to validate the hybrid RANS/LES approach, flow statistics obtained from the simulations are thoroughly compared against the available DNS data.

3.1 Numerical Aspects

Figure 3.1 shows the computational domain of the plane channel and coordinate system. The dimensions of the computational domain are $L_1 \times L_2 \times L_3 = 2.5\pi\delta \times 2\delta \times \pi\delta$ in the streamwise (x_1), wall-normal (x_2) and spanwise (x_3) directions, respectively. Two Reynolds numbers have been tested in this chapter, i.e. $Re_\tau \overset{\text{def}}{=} u_\tau\delta/\nu = 650$ and 1020. In order to thoroughly examine the proposed forcing model represented by Eq. (2.22), a comprehensive comparative study based on 12 test cases has been conducted. Table 3.1 summarizes the parameters used in these 12 test cases, with different combinations of Reynolds numbers, grid resolutions, SGS models, RANS-LES interface locations, and regions where forcing is applied. Among these test cases,

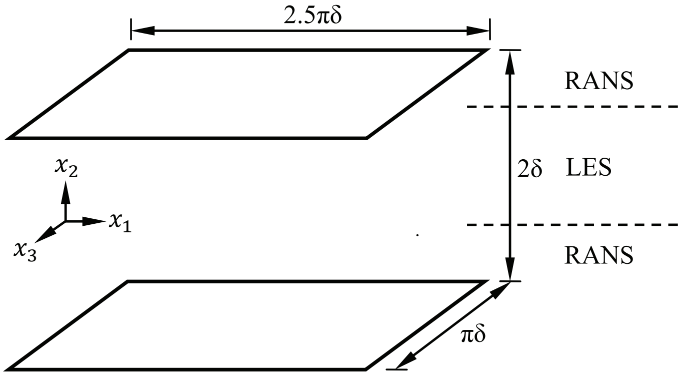

FIGURE 3.1: Computational domain for hybrid RANS/LES of a turbulent plane channel flow (using RANS in the near-wall region and LES in the core of the channel).

test case 1 is singled out to be used as the 'base case' in the comparative study. In Table 3.1, δ^+ represents the non-dimensionalized half channel height expressed using wall coordinates (i.e., $\delta^+ = \delta u_\tau/\nu$), and ΔC_f represents the percent discrepancy in the mean skin friction coefficient predicted using the current hybrid approach and DNS, viz.

$$\Delta C_f = \frac{C_{f,\,\mathrm{hybrid}} - C_{f,\,\mathrm{DNS}}}{C_{f,\,\mathrm{DNS}}} \times 100\% \quad . \tag{3.1}$$

The grid is uniform in the streamwise and spanwise directions, and stretched in the wall-normal direction using a hyperbolic-tangent function in order to provide a greater resolution in the near-wall region. The wall-normal dimensions of control volumes are given as follows:

$$\frac{\Delta x_{2,j}}{\delta} = \frac{\tanh(a\xi_j)}{\tanh(a)} - \frac{\tanh(a\xi_{j-1})}{\tanh(a)} \quad , \tag{3.2}$$

with

$$\xi_0 = -1 \quad \text{and} \quad \xi_j = \frac{2j}{N_2} - 1 \quad (\text{for } j = 1, 2, ..., N_2) \quad , \tag{3.3}$$

where N_2 is the total number of control volumes in the wall-normal direction, and a is a shape parameter for the hyperbolic function set to 1.85. The minimum value of Δx_2^+ corresponds to the wall-normal size of the first control volume off the wall, and is documented in Table 3.1 for each test case.

No slip and impermeable boundary conditions were imposed on the velocity components at the walls. Periodic boundary conditions were employed in the streamwise

TABLE 3.1: Test cases for hybrid RANS/LES of a fully-developed turbulent plane channel flow.

Case	Re_τ	$N_1 \times N_2 \times N_3$	SGS model	$\Delta x^+_{2,\ \mathrm{min}}$	$x^+_{2,\ \mathrm{interface}}$	Forcing region	ΔC_f	Comments
1 (base)	650	$64 \times 64 \times 64$	SM	3.9	39	$0 < x_2^+ < \delta^+$	-1.3%	
2	650	$64 \times 64 \times 64$	SM	3.9	6.5	$0 < x_2^+ < \delta^+$	-2.4%	
3	650	$64 \times 64 \times 64$	SM	3.9	19.5	$0 < x_2^+ < \delta^+$	-2.3%	
4	650	$32 \times 32 \times 32$	SM	8.4	39	$0 < x_2^+ < \delta^+$	-16.4%	Failure
5	650	$48 \times 48 \times 48$	SM	5.4	39	$0 < x_2^+ < \delta^+$	-3.5%	
6	650	$96 \times 96 \times 96$	SM	2.6	39	$0 < x_2^+ < \delta^+$	-1.2%	
7	650	$64 \times 64 \times 64$	SM	3.9	39	$0 < x_2^+ < x^+_{2,\ \mathrm{interface}}$	-1.2%	
8	650	$64 \times 64 \times 64$	SM	3.9	39	$x^+_{2,\ \mathrm{interface}} < x_2^+ < \delta^+$	-1.3%	
9	650	$64 \times 64 \times 64$	DSM	3.9	39	$0 < x_2^+ < \delta^+$	-1.3%	
10	650	$64 \times 64 \times 64$	SM	3.9	39	without forcing	-16.2%	Failure
11	650	$64 \times 96 \times 64$	SM	2.6	39	without forcing	-15.4%	Failure
12	1020	$96 \times 64 \times 64$	SM	6.1	61	$0 < x_2^+ < \delta^+$	-1.4%	

and spanwise directions since the flow field is assumed to be statistically homogeneous in these two directions. Statistics of various flow variables were calculated after the fluid field became turbulent and fully developed. In the presentation of the results, quantities non-dimensionalized using the friction velocity $u_\tau \overset{\text{def}}{=} \sqrt{\tau_w/\rho}$ (where τ_w represents the wall shear stress) are denoted with a superscript '+'.

3.2 Results and Discussions

In this section, flow statistics obtained from hybrid RANS/LES are thoroughly analyzed, which include the resolved mean velocity, resolved velocity fluctuations, resolved turbulent shear stresses and TKE, backscatter of KE produced by the dynamic forcing, and budget of total shear stresses. Furthermore, the physics underlying the formation of the artificial buffer layer are studied, and the effects of the proposed forcing term on breaking-up of super-streaks and on reduction of the velocity shift and artificial buffer layer are investigated. The influences of different grid resolutions, SGS models, and locations for applying the dynamic forcing on the predictive accuracy of the proposed hybrid method are also examined.

An instantaneous filtered quantity $\bar{\phi}$ can be decomposed into a time- and plane-averaged component and a residual component as:

$$\bar{\phi} = \langle \bar{\phi} \rangle + \bar{\phi}'' \quad . \tag{3.4}$$

Then the predicted resolved velocity fluctuations (or root-mean-square (RMS) values) can be defined as

$$\bar{u}^+_{i,\,\mathrm{rms}} \overset{\text{def}}{=} \left\langle \left(\frac{\bar{u}_i - \langle \bar{u}_i \rangle}{u_\tau} \right)^2 \right\rangle^{1/2} = \frac{\langle \bar{u}''^2_i \rangle^{1/2}}{u_\tau} \quad , \tag{3.5}$$

for $i = 1$, 2 and 3 respectively.

The physics underlying the formation of the artificial buffer layer, and the effects of the dynamic forcing on reducing the thickness and impact of the artificial buffer layer, can be well interpreted by utilizing transport equations for the resolved turbulent stresses. These transport equations have been derived in the full LES study of Xun *et al.* [61] on a rotating turbulent channel flow. It is worthwhile to note that the production terms in the transport equations have a significant influence on the absolute value and distribution of the resolved turbulent shear stresses (i.e., $-\langle \bar{u}_i'' \bar{u}_j'' \rangle$) and TKE (i.e., $\frac{1}{2}\langle \bar{u}_i'' \bar{u}_i'' \rangle$). The production rate for the resolved shear stress component $-\langle \bar{u}_1'' \bar{u}_2'' \rangle$ in a fully-developed turbulent channel flow is given by

$$P_{12} = \langle \bar{u}_2''^2 \rangle \frac{d\langle \bar{u}_1 \rangle}{dx_2} \quad , \tag{3.6}$$

and those for the resolved normal stress components $\langle \bar{u}_j'' \bar{u}_j'' \rangle$ (no summation implied here) are given by

$$P_{11} = -2\langle \bar{u}_1'' \bar{u}_2'' \rangle \frac{d\langle \bar{u}_1 \rangle}{dx_2} \quad , \tag{3.7}$$

$$P_{22} = 0 \quad , \tag{3.8}$$

$$P_{33} = 0 \quad . \tag{3.9}$$

The production rate for the resolved TKE can be obtained by taking one half of the sum of Eqs. (3.7)–(3.9), viz.

$$P_k = -\langle \bar{u}_1'' \bar{u}_2'' \rangle \frac{d\langle \bar{u}_1 \rangle}{dx_2} \quad . \tag{3.10}$$

The term on the RHS of Eqs. (3.6)–(3.10) implies the production rate arising from the mean resolved turbulent (shear and normal) stresses. In a fully-developed channel flow, $-\langle \bar{u}_1'' \bar{u}_2'' \rangle$ has the same parity as $d\langle \bar{u}_1 \rangle / dx_2$, both of which are positive and negative for $x_2 < 0$ and $x_2 > 0$, respectively. As a result, $P_{11} > 0$ holds across the entire channel, whereas P_{12} assumes a sign that is opposite to that of x_2. Because $P_{22} = P_{33} = 0$, there is no direct production for either $\langle \bar{u}_2''^2 \rangle$ or $\langle \bar{u}_3''^2 \rangle$ from the resolved turbulent stresses. Nevertheless, energy redistributes within the system and influences both these terms through the mechanisms of molecular diffusion, SGS production and diffusion, and pressure-strain interactions [61]. SGS production arises from the

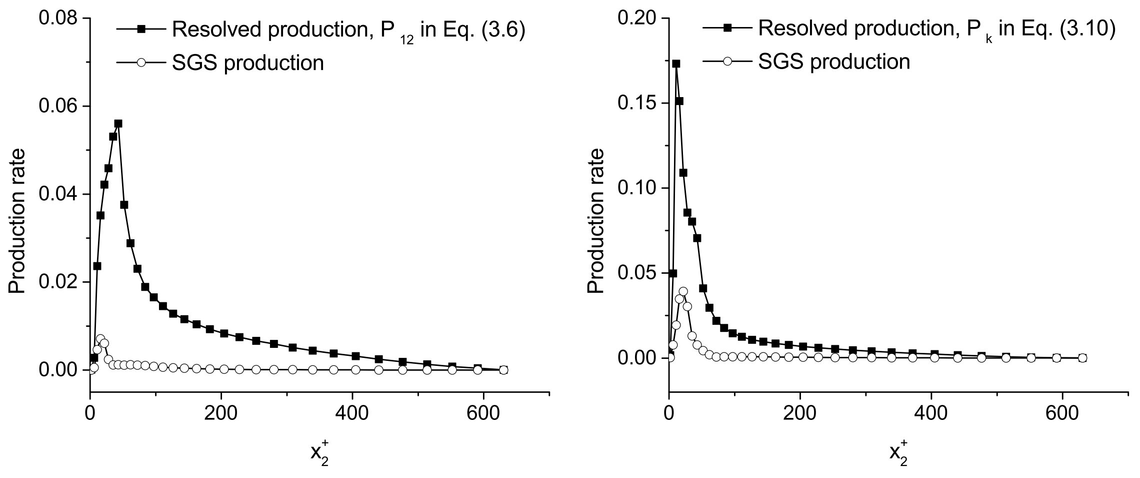

(a) Production for $-\langle \bar{u}_1''\bar{u}_2''\rangle$ (b) Production for $\frac{1}{2}\langle \bar{u}_i''\bar{u}_i''\rangle$

FIGURE 3.2: Comparison of the production rates contributed by the resolved and subgrid scales, with forcing applied to the entire computational domain for $0 < x_2^+ < \delta^+$ (non-dimensionalized using u_τ^4/ν; $Re_\tau = 650$; grid: $64 \times 64 \times 64$; interface: $x^+_{2,\,\mathrm{interface}} = 39$; SGS model in LES zone: SM).

action of the SGS stresses on the gradient of the residual velocity, and is associated with the interaction between the SGS stresses and the velocity fluctuations, i.e., $\langle \tau_{ij}\frac{\partial \bar{u}_k''}{\partial x_j}\rangle + \langle \tau_{kj}\frac{\partial \bar{u}_i''}{\partial x_j}\rangle$. Here, τ_{ij} is the SGS stress tensor. Fig. 3.2 compares production rate contributed by the subgrid scales with that contributed by the resolved scales. The total production for the resolved turbulent stresses and TKE in a hybrid approach includes contributions from both resolved and subgrid scales. As shown in Figs. 3.2(a) and (b), the production arising from the mean resolved turbulent (shear and normal) stresses dominates the SGS contributions. The maximum SGS production rate is 12.7% and 22.7% of the maximum resolved production rate (given by Eq. (3.6) and Eq. (3.10), respectively).

In order to validate the proposed dynamic forcing scheme for hybrid RANS/LES, the numerical results obtained at two Reynolds numbers are compared against two sets of DNS data obtained by Abe *et al.* [62] (designated here as AKM-2004, for $Re_\tau = 1020$) and Iwamoto *et al.* [63] (designated here as ISK-2002, for $Re_\tau = 650$), respectively. Furthermore, in order to demonstrate the advantages of the proposed method, in the next two subsections, the results on hybrid RANS/LES with and without forcing will be carefully compared.

3.2.1 Hybrid RANS/LES without Forcing

As shown in Fig. 3.3(a), for hybrid RANS/LES without forcing, the mean velocity profile deviates significantly from the profile of the log-law of the wall, and it is apparent that there exists a velocity shift. This incorrect prediction of the mean velocity profile by hybrid RANS/LES without forcing is a well-known result, which has been reported in many previous studies [11,14,15,23,24]. The discrepancy between the predicted mean velocity profile and the standard log-law is due to the existence of the artificial buffer layer between the LES and RANS zones. Baggett [16] observed the presence of very elongated non-physical 'super-streaks' in his hybrid RANS/LES study of a turbulent plane channel flow. These super-streaks cause a de-correlation between streamwise and wall-normal fluctuations. The observation of Baggett [16] is confirmed by the current study. As clearly shown in Fig. 3.4, super-streaks exist in the current flow (as a result of hybrid RANS/LES without forcing) and can be effectively demonstrated using the isopleths of instantaneous streamwise velocity fluctuations $\bar{u}_1''$ in the (x_1, x_3)-plane at the interface $x^+_{2,\text{ interface}} = 39$. Later in section 3.2.2.2, how these super-streaks can be effectively destroyed will be thoroughly demonstrated with the proposed forcing scheme in order to foster small-scale motions at the interface of the RANS and LES regions.

The formation of the artificial buffer layer (indicated by larger gradients of the resolved mean velocity around the interface) can be well explained by utilizing transport equations of turbulent stresses. Because of the de-correlation between streamwise and wall-normal fluctuations, the redistribution of TKE from the streamwise to the wall-normal component is suppressed. The contribution from subgrid scales is the sole source of production for the wall-normal component of resolved stresses, because $P_{22} = 0$ in Eq. (3.8). As shown in Fig. 3.5, for hybrid RANS/LES without forcing, the level of SGS production has been significantly reduced (by maximum 84.2%) in comparison with the case with forcing applied to the entire computational domain. As such, it is expected to observe a substantial underprediction of $\langle \bar{u}_2''^2 \rangle$ if forcing is absent. This is evident as $\bar{u}_{2,\text{ rms}}$ is excessively damped around the interface in

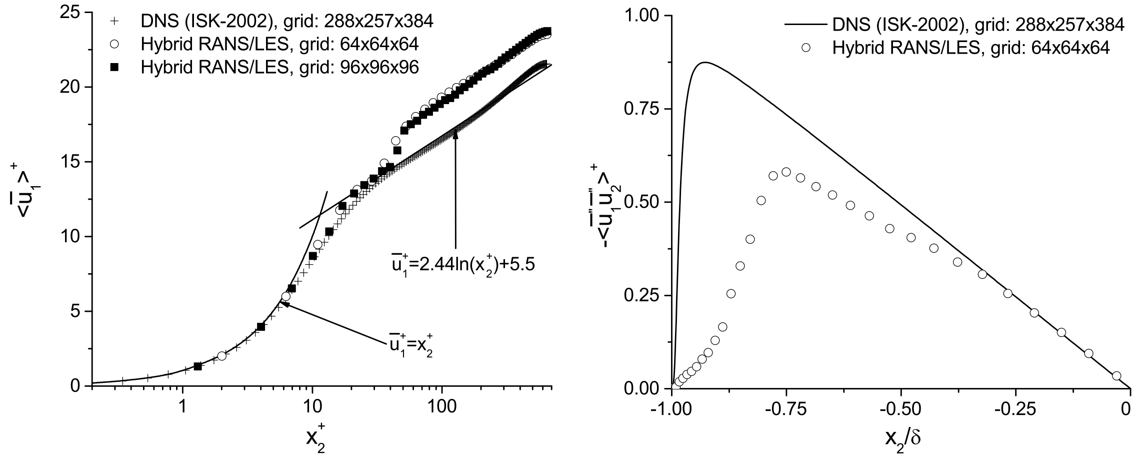

(a) Resolved mean velocity

(b) Resolved turbulent shear stress

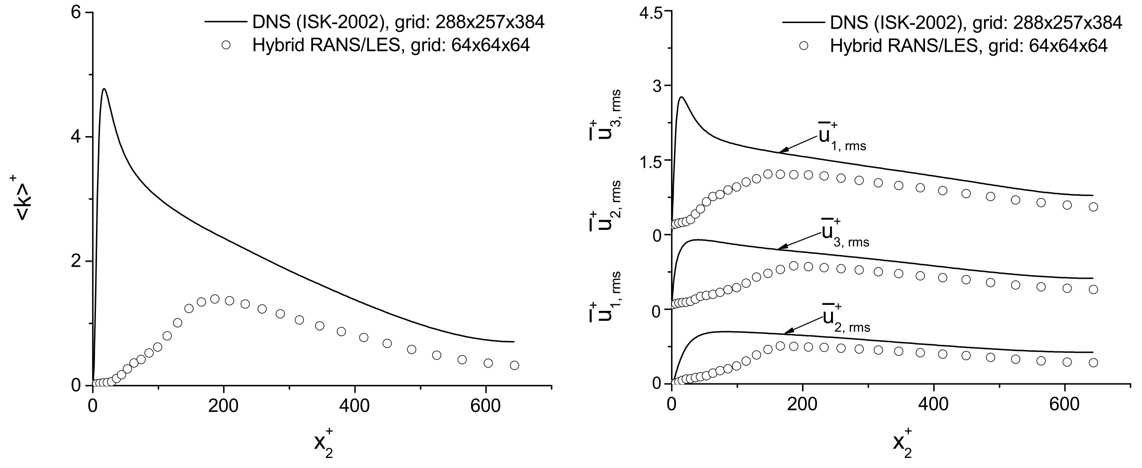

(c) Resolved turbulence kinetic energy

(d) Resolved velocity fluctuations

FIGURE 3.3: Resolved mean velocity, turbulent shear stress, turbulence kinetic energy and velocity fluctuations for hybrid RANS/LES without forcing ($Re_\tau = 650$; interface: $x^+_{2,\text{ interface}} = 39$; SGS model in LES zone: SM).

Fig. 3.3(d). Consequently, the velocity must shift upwards from the standard log-law (exhibiting an overly large gradient) in order to compensate the production P_{12} for the resolved shear stress $-\langle \bar{u}_1''\bar{u}_2''\rangle$ (cf. Eq. (3.6)). However, as shown in Fig. 3.3(b), the level of the resolved shear stress is much reduced, which then leads to a decrease in the values of the production terms P_k and P_{11} (see Eqs. (3.7) and (3.10)). This inevitably results in unreasonably low levels of resolved TKE and $\bar{u}_{1,\text{ rms}}$, which are clearly shown in Figs. 3.3(c) and 3.3(d), respectively. In comparison with the DNS result, the level of resolved normal stresses for hybrid RANS/LES without forcing

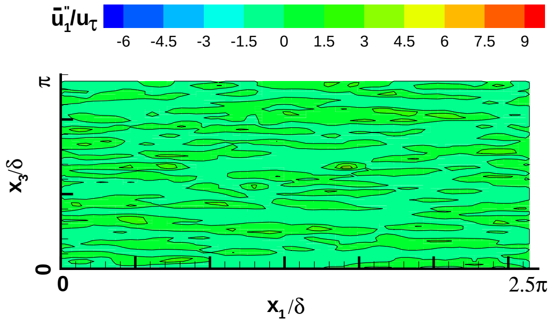

FIGURE 3.4: Isopleths of instantaneous streamwise velocity fluctuations $\bar{u}_1''$ in the $(x_1,\ x_3)$-plane at the interface located at $x^+_{2,\text{ interface}} = 39$ for hybrid RANS/LES without forcing ($Re_\tau = 650$; grid: $64 \times 64 \times 64$; SGS model in LES zone: SM).

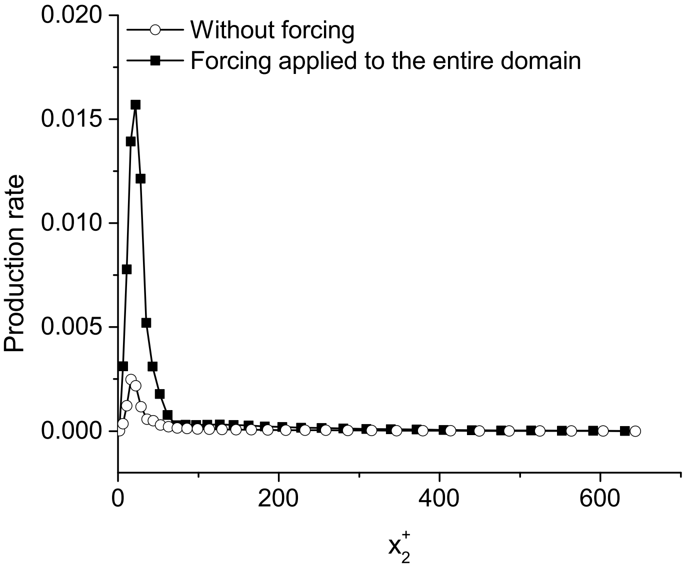

FIGURE 3.5: SGS production for $\bar{u}_{2,\text{ rms}}$ for hybrid RANS/LES with and without forcing (non-dimensionalized using u_τ^4/ν; $Re_\tau = 650$; grid: $64 \times 64 \times 64$; interface: $x^+_{2,\text{ interface}} = 39$; SGS model in LES zone: SM).

has been reduced by 77.1%, 85.2% and 81.6% for the streamwise, wall-normal and spanwise component at the interface (i.e., $x_2^+ = 39$), respectively.

3.2.2 Hybrid RANS/LES with Dynamic Forcing

The proposed dynamic forcing scheme represented by Eq. (2.22) is associated with the production term in Eq. (2.27). In the remainder of this subsection, with the dynamic forcing applied for hybrid RANS/LES, both instantaneous and averaged profiles of model constants in Eq. (2.22) will be analyzed. Then, the effects of forcing region, interface location, grid resolution and SGS model on both the first- and the second-order flow statistics will be investigated.

3.2.2.1 Model Coefficients

In a full LES, when the conventional DSM is applied to simulation of turbulence with a statistically homogeneous plane, the plane-averaging technique is often adopted to avoid numerical instability due to either excessive backscatter of SGS TKE or potential singularity of the modeling formulation. The current hybrid simulations are performed without any time- or plane-averaging for achieving numerical stability during the process of solving the linear matrix system (**AC=B**) represented by Eq. (2.25) to obtain model coefficients C_W and C_N. The condition number cond(A), i.e. $\text{cond}(A) = ||A||_\infty \cdot \|A^{-1}\|_\infty$, can be used for evaluating the stability of a linear matrix system such as Eq. (2.25). Here, the norm of matrix **A** is defined as

$$||A||_\infty = \max_{1\leq i\leq 3} \sum_{j=1}^{3} |A_{ij}| \quad . \tag{3.11}$$

As cond(A) increases, the linear matrix system becomes less stable in numerical simulations, and in the worst scenario, the system would become singular if $\text{cond}(A) \to \infty$. Fig. 3.6 shows profiles of the averaged and instantaneous condition number along the wall-normal direction. Typically, the instantaneous condition number has a value of about 15 with a maximum value of 125.4. The averaged condition number ranges from 10 to 60. These profiles indicate that the stability of the linear matrix system **AC=B** for the forcing model is generally satisfactory in the hybrid simulations performed. This is consistent with the full LES study of Wang and Bergstrom [49] that time- and plane-averaging is no longer necessary for obtaining the model constants in a dynamic nonlinear SGS modelling approach, and this observation has been included in the recent review of Meneveau [64]. In fact, multiple numerical tests have been performed in this study, each case with a significant number of time steps, and no

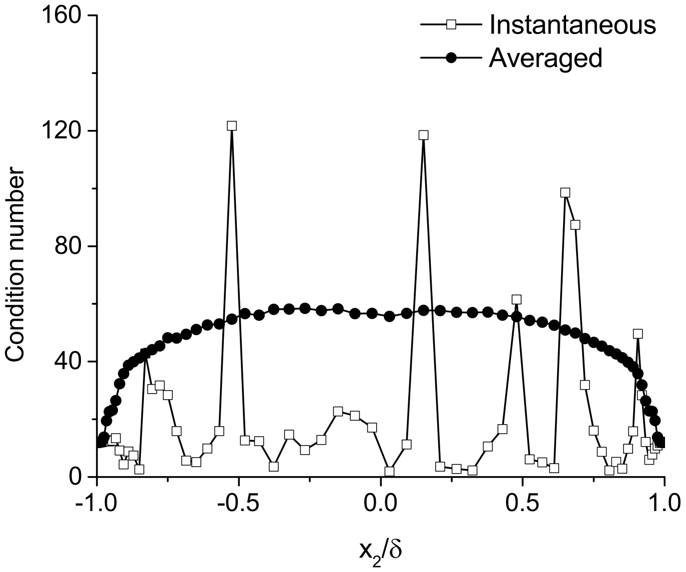

FIGURE 3.6: Profiles of averaged and instantaneous condition number obtained from hybrid RANS/LES with forcing applied to the entire domain ($Re_\tau = 650$; grid: $64 \times 64 \times 64$; interface: $x^+_{2,\text{ interface}} = 39$; SGS model in LES zone: DSM). The instantaneous values were extracted at the central domain for $x_1/L_1 = x_3/L_3 \approx 0.5$.

singularity difficulty has ever been encountered.

Figure 3.7 shows profiles of the averaged and instantaneous model coefficients along the wall-normal direction. In both Figs. 3.7(a) and (b), profiles of C_S are displayed in the LES region where the DSM has been employed in the hybrid approach. As shown in Fig. 3.7(a), both C_N and C_W reduce to zero at the wall and their magnitudes peak at the interface between RANS and LES region. The profiles of the coefficients exhibit a clear anisotropy in the wall-normal direction due to the restriction from the walls and the prescribed interface in the hybrid approach. The averaged value is positive for coefficients C_S and C_W, but negative for C_N. In the core region for the flow, the values for these three model coefficients are about $C_S = 0.0025$, $C_W = 0.010$, and $C_N = -0.010$. As shown in Fig. 3.7(b), the instantaneous coefficients fluctuate with an amplitude about 0–8 times the averaged values (shown in Fig. 3.7(a)). From Eq. (2.25), it is understood that the coefficients are flow dependent and determined by tensors derived from an instantaneous resolved flow field. Therefore, the model coefficients should be considered as local resolved turbulent quantities (via modelling). Although plane averaging of the model coefficients

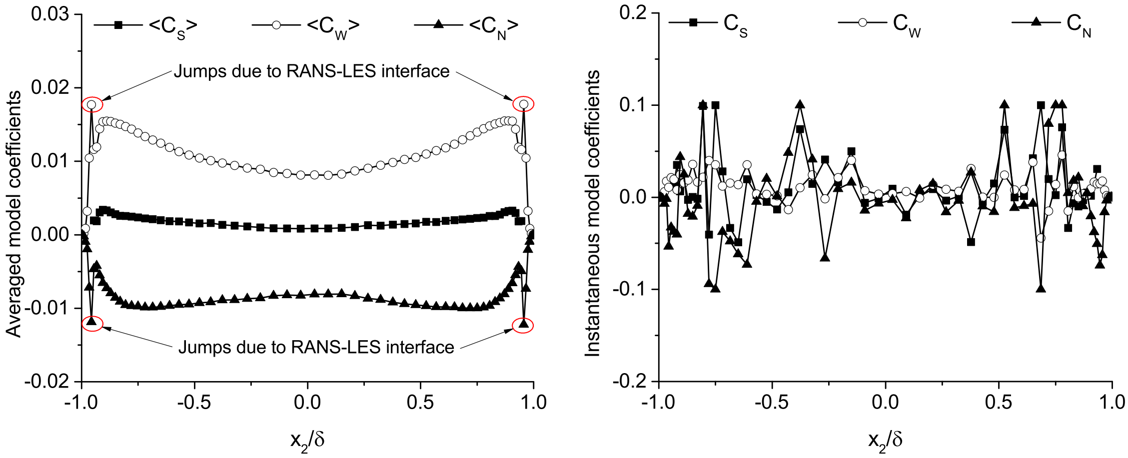

(a) Time- and plane-averaged

(b) Instantaneous

FIGURE 3.7: Profiles of averaged and instantaneous model coefficients C_S, C_W and C_N obtained from hybrid RANS/LES with forcing applied to the entire domain ($Re_\tau = 650$; grid: $64 \times 64 \times 64$; interface: $x^+_{2,\text{ interface}} = 39$; SGS model in LES zone: DSM). The instantaneous values were extracted at the central domain for $x_1/L_1 = x_3/L_3 \approx 0.5$.

is helpful to make the simulation more stable, the dynamic feature of the forcing model (and its coefficients) being locally self-adjusting at the resolved scales would be sacrificed.

3.2.2.2 Effects of Forcing Region

To date, the forcing techniques incorporating backscatter have been applied exclusively to either the RANS zone or the LES zone in previous hybrid RANS/LES studies. One may expect small scale flow motions are potentially effective in breaking up super-streaks, and therefore, the forcing should be applied to the RANS region. However, one could also argue that the forcing should be applied to the energetic scales which carry most of the TKE and are responsible for generating resolved Reynolds stresses in the LES zone. The debate on this issue has not been concluded in literature. Piomelli *et al.* [23] employed backscatter forcing in the RANS region below the interface, however, Davidson [52] added backscatter forcing to special scales in the LES region for $x^+_{2,\text{ interface}} < x^+_2 < 2x^+_{2,\text{ interface}}$. In this study, in order to investigate the effects of forcing region on the predictive accuracy of the hybrid approach, the present

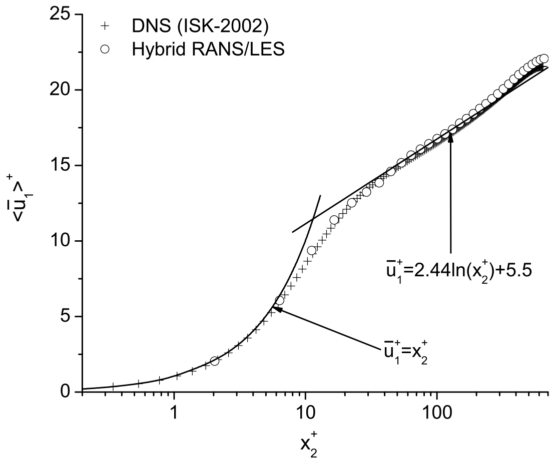

(a) Forcing in $0 < x_2^+ < x^+_{2,\text{ interface}}$

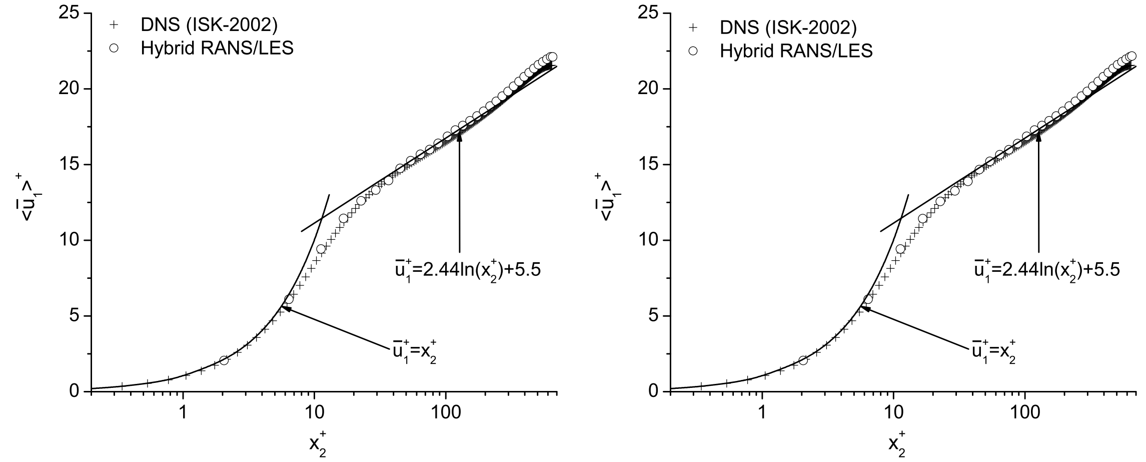

(b) Forcing in $x^+_{2,\text{ interface}} < x_2^+ < \delta^+$ (c) Forcing in entire domain $0 < x_2^+ < \delta^+$

FIGURE 3.8: Resolved mean velocity profile obtained from hybrid RANS/LES with forcing applied to three different regions ($Re_\tau = 650$; grid: $64 \times 64 \times 64$; interface: $x^+_{2,\text{ interface}} = 39$; SGS model in LES zone: SM).

backscatter forcing are tested in three different regions: (1) over the entire domain ($0 < x_2^+ < \delta^+$), (2) in the RANS region only ($0 < x_2^+ < x^+_{2,\text{ interface}}$), and (3) in the LES region only ($x^+_{2,\text{ interface}} < x_2^+ < \delta^+$). As shown in Figs. 3.8(a)–(c), the artificial buffer layer has been successfully removed for all three cases regardless the choices of forcing regions. In view of this, it is confirmed that the forcing region is indeed not a sensitive factor in a hybrid method, as long as the forcing is in use. The mechanism of backscatter of KE is a key element in a forcing design, which directly determines the success of breaking up super-streaks and removal of the undesirable artificial buffer

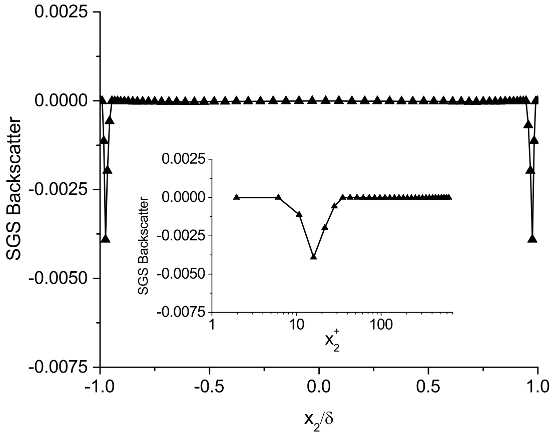

(a) Forcing in $0 < x_2^+ < x_{2,\text{ interface}}^+$

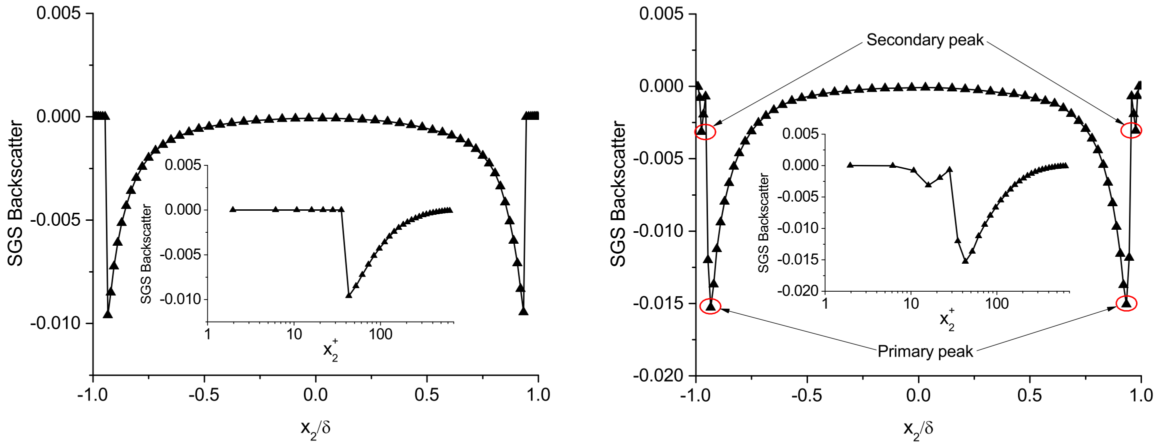

(b) Forcing in $x_{2,\text{ interface}}^+ < x_2^+ < \delta^+$

(c) Forcing in entire domain $0 < x_2^+ < \delta^+$

FIGURE 3.9: Backscatter of KE produced by the dynamic forcing exhibited using profiles of the time- and plane-averaged KE production rate $\langle P_r^B \rangle$ with forcing applied to three different regions (non-dimensionalized using u_τ^4/ν; $Re_\tau = 650$; grid: $64 \times 64 \times 64$; interface: $x_{2,\text{ interface}}^+ = 39$; SGS model in LES zone: SM). The small figure is rescaled using semi-logarithmic wall coordinate x_2^+ to highlight near-wall effects.

layer in a hybrid approach. In the following context, these key physical features will be analyzed.

Figures 3.9(a)–(c) show the time- and plane-averaged profile of $\langle P_r^B \rangle$ for the three forcing regions tested. The value of $\langle P_r^B \rangle$ has been non-dimensionalized using a constant wall dissipation rate defined as $\varepsilon_{wall} \overset{\text{def}}{=} u_\tau^4/\nu \approx 2\nu[\langle \bar{S}_{ij} \rangle \langle \bar{S}_{ij} \rangle]_{wall}$ (see Wang *et al.* [51] for the near-wall approximation of $\langle \bar{S}_{ij} \rangle$). For all three different forcing regions, the value of $\langle P_r^B \rangle$ maintains negative across the entire channel, representing a net effect of backscatter. Although the resolved mean velocity profiles (as an output from the filtered momentum equation (2.20)) obtained using different forcing regions are very similar in Fig. 3.8, the backscatter (as a forcing input to the filtered momentum equation (2.20)) itself shows distinctively different patterns. As shown in Fig. 3.9(a), the magnitude of backscatter reaches its maximum between the solid wall and the modelling interface (at $x_2^+ = 17$), then drastically reduces to zero immediately outside of the interface (within the core region of the channel). This feature is expected, because the forcing is exclusively applied to the RANS region. However, as shown in Fig. 3.9(b), when the forcing is applied to the LES region only, the magnitude of backscatter increases drastically from zero near the solid wall (in the RANS region) to its peak value right above the interface (at $x_2^+ = 47$, in the LES region), and then gradually decreases back to zero in the core region of the channel. As shown in Fig. 3.9(c), when forcing is applied to the entire channel, an interesting dual-peak pattern appears in the profile of $\langle P_r^B \rangle$: a secondary peak below the interface (at $x_2^+ = 17$, in the RANS region) and a primary peak above the interface (at $x_2^+ = 47$, in the LES region). Furthermore, the magnitudes of the secondary and primary peaks are of the same order of those shown in Figs. 3.9(a) and 3.9(b), respectively. This observation of a dual-peak pattern in $\langle P_r^B \rangle$ profoundly indicates that when a forcing is applied to the entire domain, there is combined backscatter effects from both the RANS and the LES regions. The backscatter of KE shown in Figs. 3.9(a)–(c) plays an important role to break up super-streaks and maintain the proper level of turbulent shear stresses in the core region of the channel. This is also the key physical feature that contributes directly to reduction in the thickness of the artificial buffer layer and removal of the tenacious velocity shift pattern. Furthermore, it should be indicated that it is very desirable to observe that the value of the magnitude of $\langle P_r^B \rangle$ approaches zero automatically in the core turbulent region of the channel, which satisfies the physical requirement that the forcing should not affect the accurate LES predictions. Fig. 3.9 shows clear evidence that backscatter can be generated to properly treat the interfacing problem once the proposed forcing scheme is activated in either the RANS or the LES zone. This is an encouraging result, which is fundamental for stable and

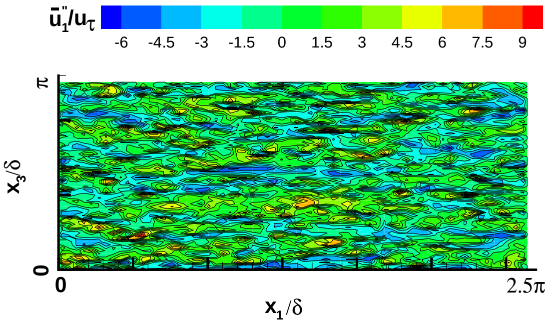

(a) Forcing in $0 < x_2^+ < x^+_{2,\text{ interface}}$

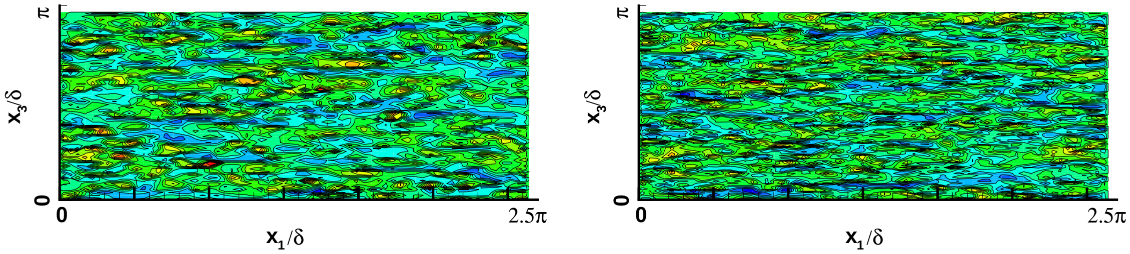

(b) Forcing in $x^+_{2,\text{ interface}} < x_2^+ < \delta^+$ (c) Forcing in entire domain $0 < x_2^+ < \delta^+$

FIGURE 3.10: Isopleths of instantaneous streamwise velocity fluctuations $\bar{u}_1''$ in the (x_1, x_3)-plane at the interface located at $x^+_{2,\text{ interface}} = 39$ with forcing applied to three different regions ($Re_\tau = 650$; grid: $64 \times 64 \times 64$; SGS model in LES zone: SM).

flexible numerical simulations based on the proposed forcing scheme.

In comparison with Fig. 3.4, it is evident in Figs. 3.10(a)–(c) that after forcing has been applied to three different regions, smaller scales are indeed formed and the super-streaks (demonstrated using isopleths of the instantaneous streamwise velocity fluctuations $\bar{u}_1''$) are broken up at the interface $x^+_{2,\text{ interface}} = 39$. This is consistent with the results that the velocity shift has been removed regardless the choices of the forcing region (see Fig. 3.8). In order to further demonstrate the physical mechanism on how forcing works to break up super-streaks as the distance from the wall increases (i.e., as x_2^+ increases), the instantaneous streamwise velocity fluctuation isopleths in a series of planes parallel to the wall are displayed in Figs. 3.11(a)–(e). These figures were obtained with the proposed forcing applied to the entire domain, which clearly show the effects of forcing on flow structures at different flow layers. The velocity fluctuation isopleths show elongated structures in the RANS region (i.e., $x_2^+ = 2$ and 17). But owing to the use of forcing as shown in Fig. 3.11(a), eddies with shorter

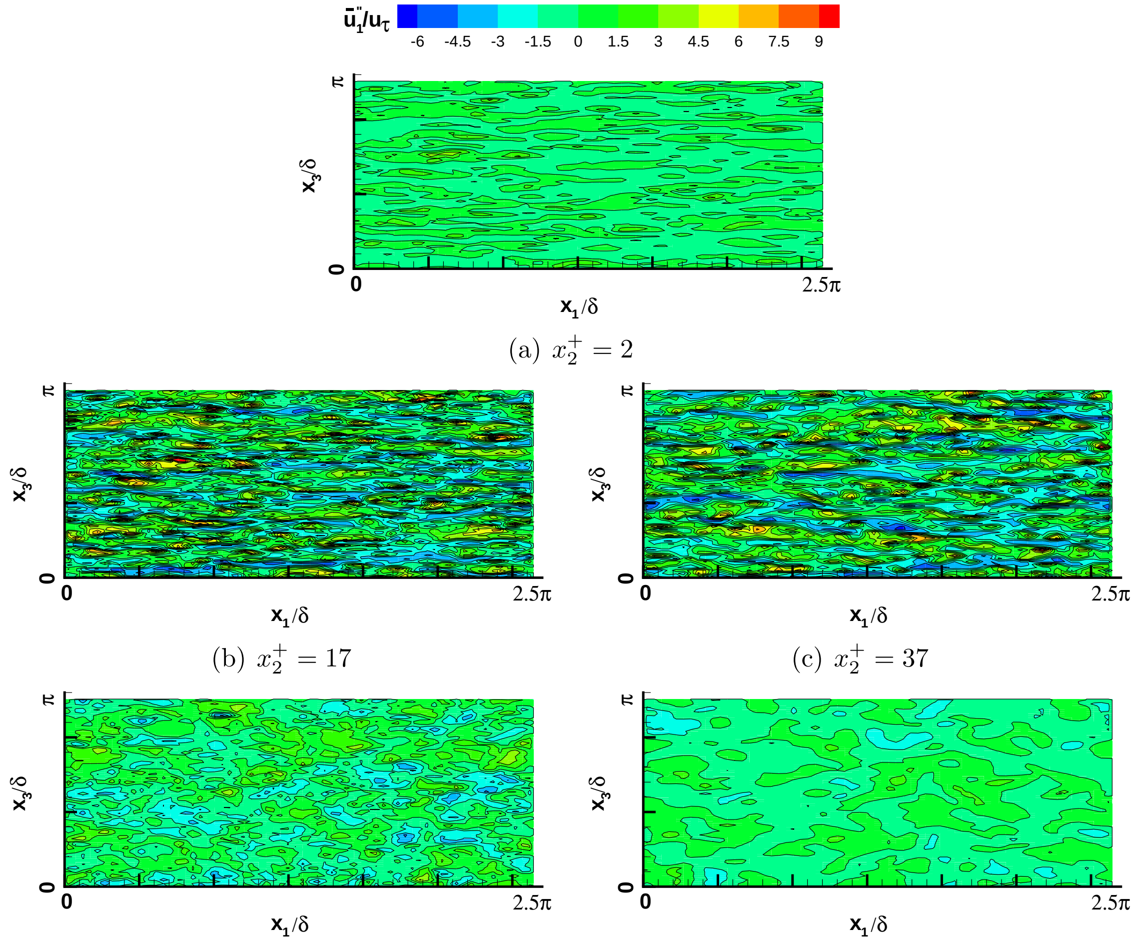

(a) $x_2^+ = 2$

(b) $x_2^+ = 17$

(c) $x_2^+ = 37$

(d) $x_2^+ = 239$

(e) $x_2^+ = 644$

FIGURE 3.11: Isopleths of instantaneous streamwise velocity fluctuations $\bar{u}_1''$ in (x_1, x_3)-planes parallel to the wall with forcing applied to the entire computational domain for $0 < x_2^+ < \delta^+$ ($Re_\tau = 650$; grid: $64 \times 64 \times 64$; interface: $x^+_{2,\text{ interface}} = 39$; SGS model in LES zone: SM).

wavelengths and time-scales can be observed even in the vicinity of the wall (i.e., $x_2^+ = 2$). It is clear from Fig. 3.11(c) that the forcing has been successful in breaking up the super-streaks and generating smaller scales near the interface (i.e., $x_2^+ = 37$). As shown in Figs. 3.11(d) and (e), in the outer flow region above the interface (for $x_2^+ = 239$ and 644), the eddies (identified using the streamwise velocity fluctuations) tend to become isotropic in the plane.

In order to quantitatively estimate the spanwise dimension of the super-streaks observed in Fig. 3.4, the two-point correlation coefficient of the streamwise velocity fluctuations $\bar{u}_1''$ is investigated following the approach of Baggett [16], viz.

$$R_{11}(\Delta z) = \frac{\langle \bar{u}_1''(x_1, x_2, x_3, t)\bar{u}_1''(x_1, x_2, x_3 + \Delta z, t)\rangle}{\langle \bar{u}_1''(x_1, x_2, x_3, t)^2\rangle} \quad . \tag{3.12}$$

Here, R_{11} is a function of spanwise separation length Δz between two points. Fig. 3.12 shows the correlation coefficient R_{11} in the x_1-x_3 plane at $x_2^+ = 2$. As it is evident in Fig. 3.12, R_{11} has a minimum value at a certain spanwise separation length Δz_{min}. The separation length at which the distinct minimum occurs provides an estimate of the mean separation length scale between high- and low-speed flows [19,20]. The mean spacing between the near-wall streaks can be therefore defined as twice the spanwise separation length scale corresponding to minimum R_{11} (i.e., $\lambda = 2\Delta z_{min}$). As shown in Fig. 3.12, for hybrid RANS/LES without forcing, the minimum value of R_{11} occurs at $\Delta z/\delta = 0.196$, which is corresponding to $\lambda^+ = 255.3$. In the hybrid approach of Baggett [16], the super-streaks has a similar value of $\lambda^+ = 260$. It is worthwhile to note that the characteristic spanwise dimension of streaks immediately off the wall is approximately $\lambda^+ = 100$ according to laboratory experiments [18, 21, 22] and DNS simulations [19, 20]. When forcing is applied to hybrid RANS/LES, regardless of the choice of the forcing regions, the value of λ^+ has been substantially reduced to 127.6. This implies that super-streaks have been broken up due to the forcing used in the current hybrid approach. Furthermore, it is expected to observe that the value of λ^+ remains the same in different forcing regions, because the value of λ^+ is universal for all near-wall streaks obtained within the range $0 < x_2^+ < 10$ [18–22].

3.2.2.3 Effects of Interface Location

At the interface, the turbulence modelling approach switches from RANS to LES and the flow fields obtained from these two modelling approaches mutually influence each other. In literature, investigations of the interface locations have focused primarily on the first-order flow statistics (i.e., mean velocity and mean skin friction coefficient associated with the discussion of artificial buffer layer and velocity shift). As analyzed in section 3.2.1, it is the incorrectly predicted second-order flow statistics (e.g., an

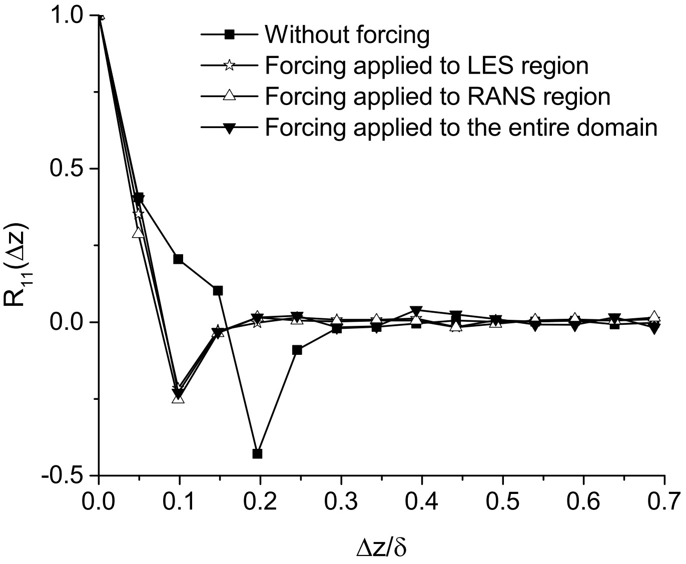

FIGURE 3.12: Two-point correlation coefficient of $\bar{u}_1''$ in the $(x_1,\, x_3)$-plane at $x_2^+ = 2$ for hybrid RANS/LES ($Re_\tau = 650$; grid: $64 \times 64 \times 64$; interface: $x^+_{2,\text{ interface}} = 39$; SGS model in LES zone: SM).

overly low level of $\bar{u}_{2,\text{ rms}}$ shown previously in Fig. 3.3(d)) that eventually cause unreasonably high gradients in the mean streamwise velocity profile around the interface (which then results in the artificial buffer layer) in a hybrid approach. The interface location that separates the RANS and LES zones can be explicitly specified using a given wall-normal distance [10, 11], or dynamically determined as the minimum of the RANS length scale (based on an integral length scale) and the LES length scale (based on the filter size) [12]. Both approaches are practical and effective in defining the interface location, and both have little influence on the thickness of the artificial buffer layer [14]. In this study, the first approach [10, 11] is adopted, and a comparative study has been conducted to examine the sensitivity of the interface locations. Furthermore, transport equations for resolved turbulent stresses and resolved TKE are utilized for investigating the effects of interface locations on the first- and second-order flow statistics. Three interface locations have been tested in the comparative study, i.e. $x^+_{2,\text{ interface}} = 6.5$, 19.5 and 39, corresponding to the viscous sublayer, buffer layer and overlap region, respectively.

Figures 3.13(a)–(d) compare these three characteristic wall-normal interface lo-

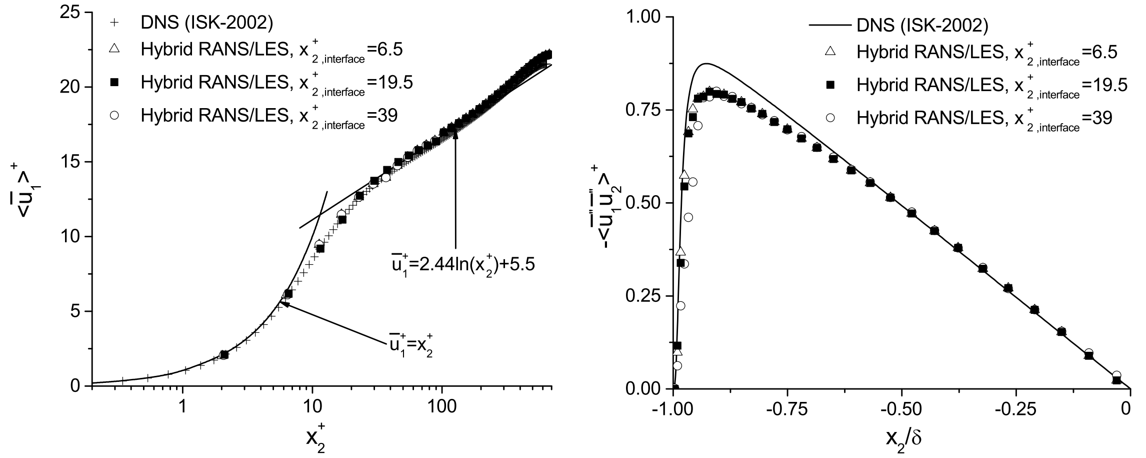

(a) Resolved mean velocity

(b) Resolved turbulent shear stress

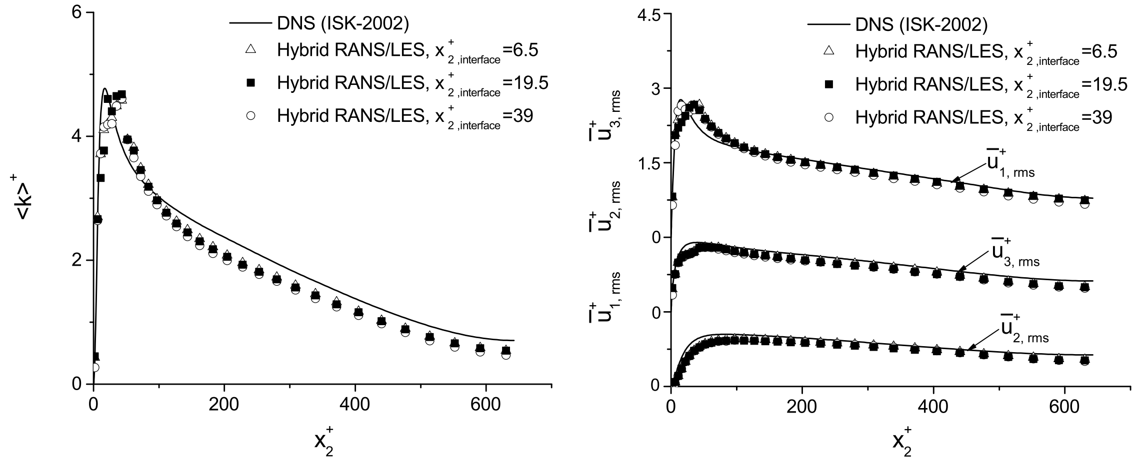

(c) Resolved turbulence kinetic energy

(d) Resolved velocity fluctuations

FIGURE 3.13: Effects of interface location on the resolved mean velocity, turbulent shear stress, turbulence kinetic energy and velocity fluctuations, with forcing applied to the entire computational domain for $0 < x_2^+ < \delta^+$ ($Re_\tau = 650$; grid: $64 \times 64 \times 64$; SGS model in LES zone: SM).

cations in terms of their effects on the predictions of the mean velocity, turbulent shear stresses, TKE and three RMS velocity components. As shown in Fig. 3.13(a), the mean velocity profiles predicted based on these three interface locations are very similar and in good agreement with both the DNS data and the classical log-law of the wall. The velocity shift around the modelling interface and the associated artificial buffer layer have been successfully removed in all three test cases, indicating that the hybrid method is indeed insensitive to the choice of the interface locations. These test results and conclusion are consistent with observations of Larsson *et al.* [14] and Nikitin *et al.* [15]. Fig. 3.13(b) compares the time- and plane-averaged resolved turbulent shear stress (i.e., $-\langle \bar{u}_1'' \bar{u}_2'' \rangle$) obtained from the hybrid approach with the 'exact' (or 'true') Reynolds shear stress (denoted using $-\langle u_1'^e u_2'^e \rangle$) from the DNS approach. As shown in Figs. 3.13(c) and (d), in general, the trends predicted by hybrid RANS/LES are in agreement with DNS data. However, small differences are observed: the hybrid method tends to slightly underpredict the resolved TKE, especially in the central region of the channel.

In order to further study the physical features exhibited in Fig. 3.13 and refine the investigation of the effects of the interface location on the predicted flow field, production terms corresponding to the resolved turbulent stresses and resolved TKE from transport equations are plotted in Figs. 3.14(a)–(c). These three figures are obtained in accordance with Eqs. (3.6), (3.10) and (3.7), respectively. As shown in Fig. 3.14(a), the predicted profiles for production term P_{12} are almost identical for three different interface locations tested. As a consequence, the value of resolved shear stress $-\langle \bar{u}_1'' \bar{u}_2'' \rangle$ is expected not to vary much as $x^+_{2,\text{ interface}}$ changes. Indeed, as it is clear from Fig. 3.13(b), predictions of $-\langle \bar{u}_1'' \bar{u}_2'' \rangle$ based on these three interface locations are consistent and close to the DNS results of Iwamoto *et al.* [63]. According to Eqs. (3.7) and (3.10), at a given Reynolds number (the profile of the mean velocity gradient component $d\langle \bar{u}_1 \rangle / dx_2$ is specified), this further necessarily makes the predicted values of P_{11} and P_k consistent in three different interface location cases. The above analysis is well confirmed through Figs. 3.14(b) and (c), which show that profiles of P_k and P_{11} obtained in the three interface location cases almost collapse. This in turn well explains the previous observation in Figs. 3.13(c) and (d) that the predicted values of the resolved TKE and $\bar{u}_{1,\text{ rms}}$ based on these three different interface locations are almost identical. It is also observed that the peak location of $\bar{u}_{1,\text{ rms}}$ slightly moves towards the wall as $x^+_{2,\text{ interface}}$ increases. Through the analysis presented in this and previous subsections, it is clear that the current hybrid approach is insensitive to the choices of the forcing region and interface location, which is a desirable feature for stable and robust simulations.

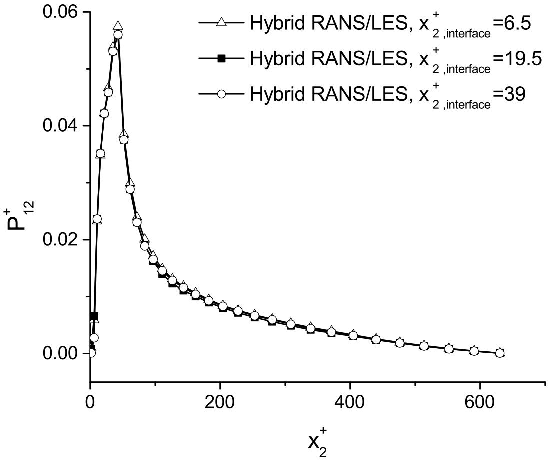

(a) P_{12}

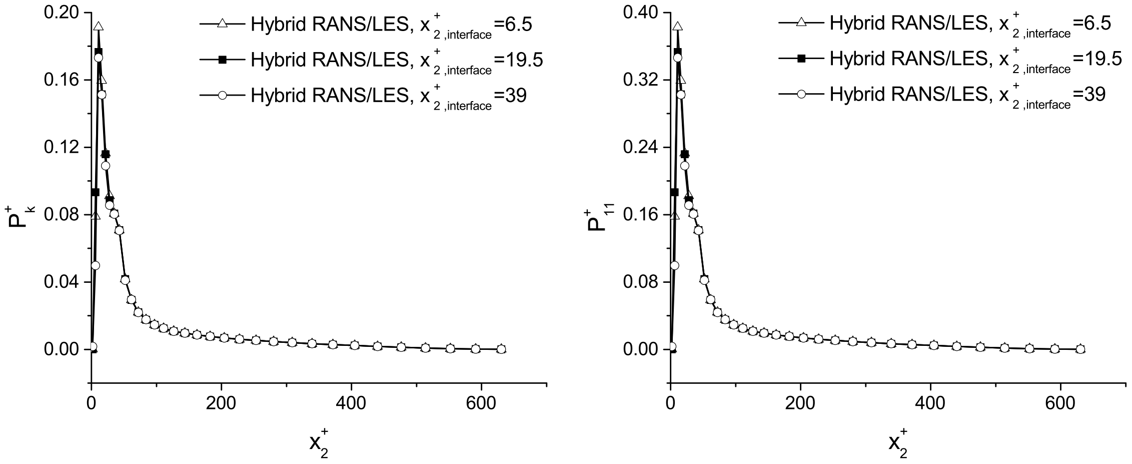

(b) P_k

(c) P_{11}

FIGURE 3.14: Effects of interface location on the production rates for the resolved turbulent shear stress P_{12}, resolved turbulence kinetic energy P_k and resolved streamwise normal stress P_{11}, with forcing applied to the entire computational domain for $0 < x_2^+ < \delta^+$ (non-dimensionalized using u_τ^4/ν; $Re_\tau = 650$; grid: $64 \times 64 \times 64$; SGS model in LES zone: SM).

3.2.2.4 Effects of Grid Resolution

The effects of grid resolution on the predictive accuracy of wall-resolved LES have been studied rather extensively in literature. It is well-known that a full LES with a coarse grid resolution tends to underpredict the mean skin friction coefficient. In the specific context of hybrid RANS/LES, it is crucial to study the effects of grid resolution on the prediction of the flow fields because the length scales resolved in

LES and RANS are significantly different. In RANS, the flow field is resolved at the largest integral scales, however, in a conventional LES approach, the field is resolved at the filter scale which correlates directly to the grid resolution. For instance, Nikitin *et al.* [15] performed hybrid RANS/LES of turbulent channel flows with different grid resolutions for a wide range of Reynolds numbers. They observed that the skin friction coefficient was underpredicted by approximately 15% in most of their cases. In the following context, how the results approach the grid independent state will be demonstrated based on different grid systems. Discrepancies in the values of the first- and second-order flow statistics due to different grid resolutions are carefully checked. In this research, a grid independent state is considered to be achieved when the discrepancy between the solutions obtained with two different grid resolutions is less than 5%.

Profiles of the resolved velocity, resolved shear stress, resolved TKE and resolved velocity fluctuations based on different grid resolutions are compared in Figs. 3.15(a)–(d). Four grid resolutions are tested in this comparative study based on 32^3, 48^3, 64^3 and 96^3 control volumes. The comparisons are made based on the common condition that the proposed forcing scheme is applied to the entire domain for $0 < x_2^+ < \delta^+$. The grid resolutions in terms of the values of non-dimensionalized nodal distances Δx_i^+ for these four grid systems are documented in Table 3.2. Davidson [52] indicated that the grid resolution in DNS and wall-resolved LES is dictated by the necessity of resolving the energy-generating process of high-speed in-rushes and low-speed ejections (i.e., the so-called streak process) in the viscous sublayer and buffer layer. For wall-resolved LES of a turbulent plane channel flow, reasonable grid resolutions are recommended to be $\Delta x_1^+ \approx 100$, $\Delta x_2^+ \approx 1$ (at wall-adjacent cell centers) and $\Delta x_3^+ = 30$ according to Davidson [52]; and $\Delta x_1^+ = 50 \sim 150$, $\Delta x_2^+ < 2$ and $\Delta x_3^+ = 15 \sim 40$ according to Piomelli and Chasnov [65]. These recommended grid resolutions for LES of turbulent channel flows are general and semi-empirical, and are obtained based on analysis of energy spectra, resolved TKE and two-point correlations of the velocity field [52,65]. It is worthwhile to note that there is a conceptual difference between wall-resolved full LES and hybrid RANS/LES approaches with respect to the near-wall solutions

TABLE 3.2: Grid resolution tests, with forcing applied to the entire computational domain for $0 < x_2^+ < \delta^+$ ($Re_\tau = 650$; interface: $x^+_{2,\text{ interface}} = 39$; SGS model in LES zone: SM).

Case	$N_1 \times N_2 \times N_3$	Δx_1^+	Δx_2^+	Δx_3^+
1 (base)	$64 \times 64 \times 64$	79.8	$3.9 \sim 39.4$	31.9
4	$32 \times 32 \times 32$	159.5	$8.4 \sim 78.6$	63.8
5	$48 \times 48 \times 48$	106.4	$5.4 \sim 52.5$	42.5
6	$96 \times 96 \times 96$	53.2	$2.6 \sim 26.1$	21.3

TABLE 3.3: Grid points used in DNS and hybrid RANS/LES of a fully-developed turbulent plane channel flow (per unit computational domain $\delta \times \delta \times \delta$).

Method	Re_τ	Grid descretization per δ^3	Computational cost saved
DNS [63]	650	$37 \times 129 \times 122$	—
Hybrid (Case 1)	650	$8 \times 32 \times 20$	99.12%
DNS [62]	1020	$160 \times 224 \times 240$	—
Hybrid (Case 12)	1020	$12 \times 32 \times 20$	99.91%

and grid resolutions. In hybrid RANS/LES, the position of the first node off the solid wall is no longer restricted to be $\Delta x_2^+ \leq 1$ due to the use of the RANS approach in the near-wall region. This advantage of hybrid RANS/LES over DNS in terms of saving of computational cost is demonstrated in Table 3.3. In order to make unbiased comparisons, the number of grid points in Table 3.3 is based on the unit computational domain $\delta \times \delta \times \delta$. With respect to grid resolutions, the hybrid approach has saved 99.12% and 99.91% of computational cost for $Re_\tau = 650$ and $Re_\tau = 1020$, respectively.

As shown in Fig. 3.15(a), the mean velocity profile obtained on the grid system of 32^3 control volumes far exceeds the standard log-law and DNS data by several wall units, which results in an underprediction of the skin friction coefficient by approximately 16.4% (see, Table 3.1). Further from Figs. 3.15(b)–(d), it is clear that this grid system (with 32^3 control volumes) has apparently failed to reproduce the correct levels of the resolved turbulent shear stress, resolved TKE, and resolved RMS velocities $\bar{u}_{1,\text{ rms}}$ and $\bar{u}_{3,\text{ rms}}$. This is a typical characteristic of a coarse grid LES computation

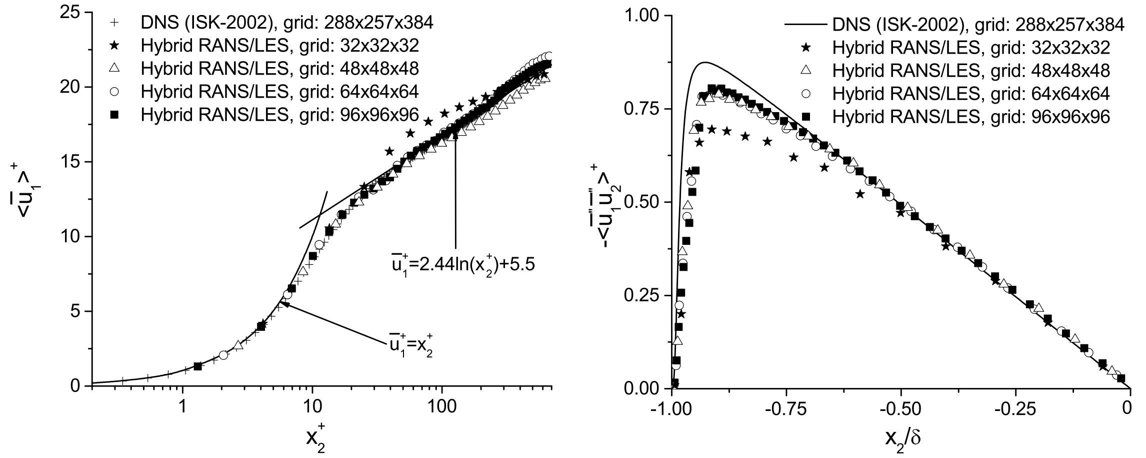

(a) Resolved mean velocity

(b) Resolved turbulent shear stress

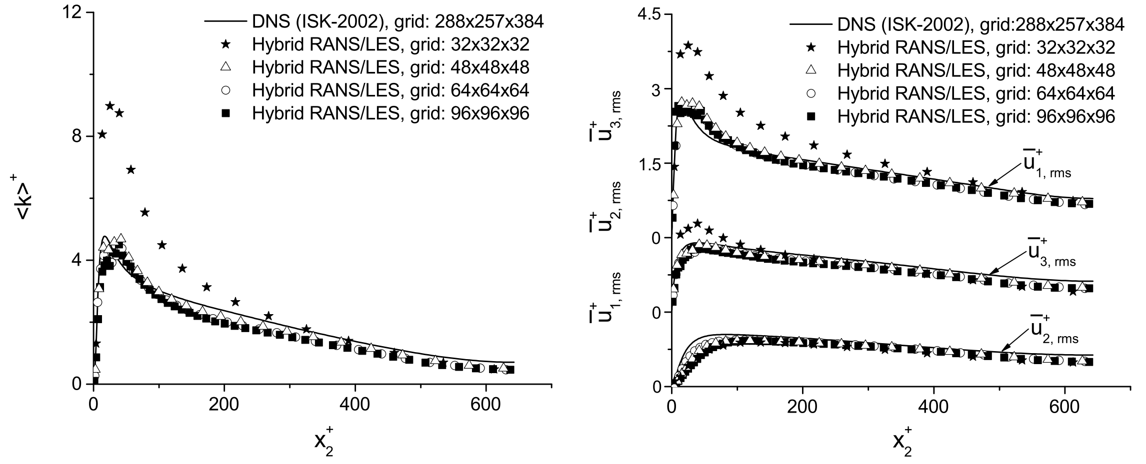

(c) Resolved turbulence kinetic energy

(d) Resolved velocity fluctuations

FIGURE 3.15: Grid independence tests with respect to the resolved mean velocity, turbulent shear stress, turbulence kinetic energy and velocity fluctuations, with forcing applied to the entire computational domain for $0 < x_2^+ < \delta^+$ ($Re_\tau = 650$; interface: $x^+_{2,\text{ interface}} = 39$; SGS model in LES zone: SM).

and is consistent with the result reported by Wang *et al.* [51] and Kravchenko *et al.* [66]. The discrepancy between the predicted value of the skin friction coefficient by the current hybrid approach and the DNS result is 3.5%, 1.3% and 1.2%, for the three grid systems of 48^3, 64^3 and 96^3 control volumes, respectively. From Fig. 3.15, it is observed that the solutions become grid independent on the grid system of 48^3 control volumes for both the first- and second-order flow statistics. This grid system yields $\Delta x_1/\delta \approx 0.164$, $\Delta x_3/\delta \approx 0.065$ and $\Delta x_2/\delta$ varying from 0.008 to 0.081 (or equivalently in the wall coordinates, $\Delta x_1^+ = 106.4$, $\Delta x_3^+ = 42.5$, and Δx_2^+ varying

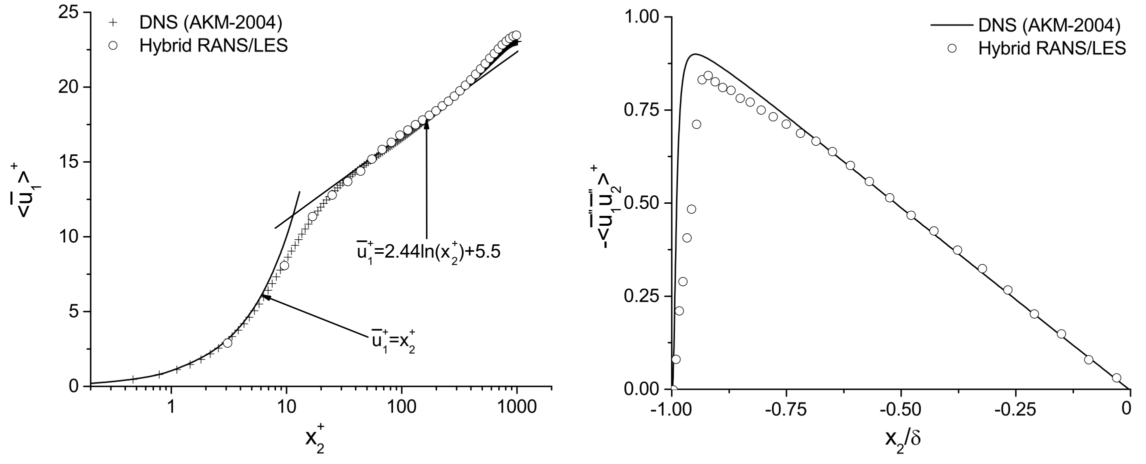

(a) Resolved mean velocity

(b) Resolved turbulent shear stress

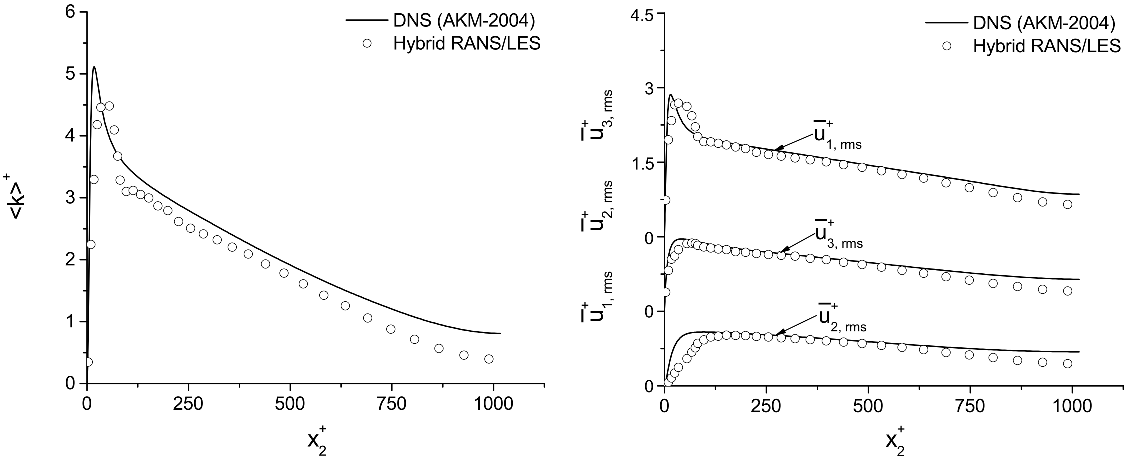

(c) Resolved turbulence kinetic energy

(d) Resolved velocity fluctuations

FIGURE 3.16: Resolved mean velocity, turbulent shear stress, turbulence kinetic energy and velocity fluctuations, with forcing applied to the entire computational domain for $0 < x_2^+ < \delta^+$ (at the higher Reynolds number for $Re_\tau = 1020$. Grid: $96 \times 64 \times 64$; interface: $x^+_{2,\text{ interface}} = 61$; SGS model in LES zone: SM).

from 5.4 to 52.5). Once the grid independent state is achieved, both the first and second-order flow statistics are in good agreement with the DNS results.

3.2.2.5 Effects of Reynolds Number on Eddy Viscosity ν_t

The proposed forcing scheme has been further examined at a higher Reynolds number for $Re_\tau = 1020$ (with forcing applied to the entire computational domain for $0 < x_2^+ < \delta^+$). Figs. 3.16(a)–(d) compare the obtained resolved mean velocity, turbulent

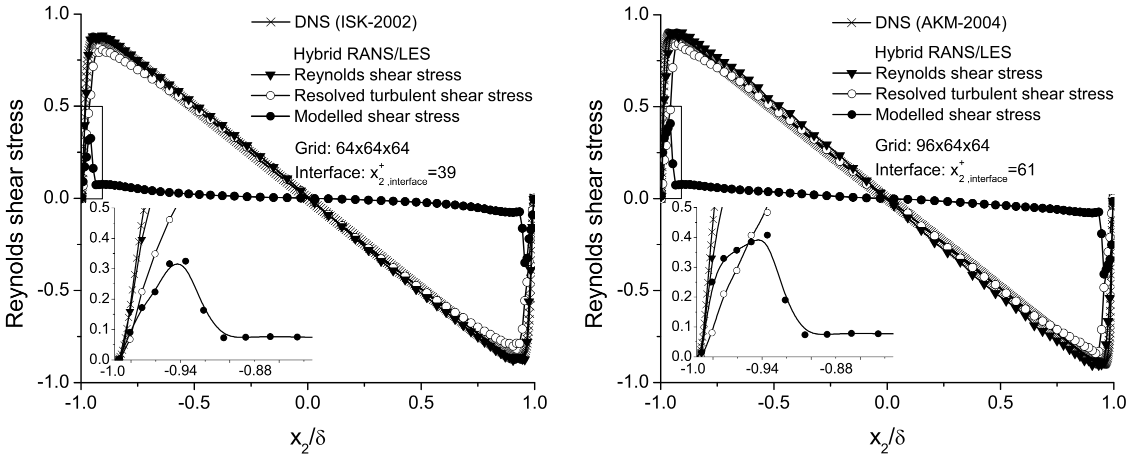

(a) $Re_\tau = 650$

(b) $Re_\tau = 1020$

FIGURE 3.17: Reynolds shear stress at $Re_\tau = 650$ and 1020 for hybrid RANS/LES with forcing applied to the entire computational domain for $0 < x_2^+ < \delta^+$ (non-dimensionalized using u_τ^2; SGS model in LES zone: SM). The framed areas are enlarged and shown separately using small figures.

shear stress, TKE and velocity fluctuations against the DNS data of Abe *et al.* [62]. As shown in Fig. 3.16(a), the well-predicted resolved mean velocity profile confirms that the artificial buffer layer has been successfully removed at $Re_\tau = 1020$. From Figs. 3.16(b)–(d), it is evident that the hybrid RANS/LES has also well predicted the second-order flow statistics at $Re_\tau = 1020$. Similar to the features exhibited in Figs. 3.13(b) and (c) for the lower Reynolds number case (for $Re_\tau = 650$), it is observed in Figs. 3.16(b) and (c) that the hybrid method tends to underpredict the resolved turbulent shear stress around its peak location and slightly underpredict the resolved TKE in the center of the channel.

The time- and plane-averaged deviatoric part of the 'exact' (or 'true') Reynolds shear stress obtained from a DNS approach can be estimated from hybrid RANS/LES by adding the resolved turbulent shear stress and the modelled shear stress [67, 68], i.e. $-\langle u_1'^e u_2'^e \rangle = -\langle \bar{u}_1'' \bar{u}_2'' \rangle + \nu_t \partial \langle \bar{u}_1 \rangle / \partial x_2$. Figs. 3.17(a) and (b) compare the Reynolds shear stresses predicted at two Reynolds numbers (i.e., $Re_\tau = 650$ and 1020) against two sets of DNS data, respectively. The stress terms presented in these figures are non-dimensionalized using u_τ^2. It is observed that the total Reynolds shear stress (i.e., $-\langle \bar{u}_1'' \bar{u}_2'' \rangle + \nu_t \partial \langle \bar{u}_1 \rangle / \partial x_2$) obtained using the current hybrid approach conforms very well with the DNS data at both Reynolds numbers. By comparing Figs. 3.17(a) and (b) with Figs. 3.13(b) and 3.16(b), respectively, it is evident that by including the modelled turbulent shear stress component $\nu_t \partial \langle \bar{u}_1 \rangle / \partial x_2$ in the calculation of the total Reynolds shear stress, the agreement between the hybrid RANS/LES with DNS predictions has been apparently improved. The characteristic anti-symmetry about $x_2/\delta = 0$ is well confirmed in the profile of the predicted total Reynolds shear stress in Figs. 3.17(a) and (b). In order to clearly demonstrate the stress profiles in the near-wall region, the curves presented in Figs. 3.17(a) and (b) are partially enlarged. As shown in both figures, in the RANS zone, the level of the modelled turbulent shear stress is comparable to the level of the resolved turbulent shear stress. In the LES region, the total Reynolds stress is primarily contributed by the resolved turbulent stress. As shown in Figs. 3.17(a) and (b), the modelled shear stress component peaks at the interface ($x_2/\delta = \pm 0.94$, or expressed using wall coordinates $x_2^+ = 39$ for $Re_\tau = 650$ and $x_2^+ = 61$ for $Re_\tau = 1020$, respectively). This feature is due to the prescribed interface where the model switches from RANS to LES. Given its modelling equation (i.e., Eq. (2.10)), the value of ν_t^R increases monotonically in the RANS region. On the other hand, it is well known that the value of the eddy viscosity is much larger in RANS than in LES, i.e. $\nu_t^R > \nu_t^L$ (because all turbulent motions including the most energetic eddy motions at the largest integral scales are modelled in RANS). As shown in the partially enlarged stress profiles in Figs. 3.17(a) and (b), Reynolds number has noticeable impact on the values and distribution of the shear stress components. Higher Reynolds number results in a higher level of modelled shear stress at the same wall-normal location x_2/δ in the RANS region. For $Re_\tau = 650$, the resolved component of shear stress exceeds the modelled component in the vicinity of the wall. However, this feature occurs around the interface for $Re_\tau = 1020$. In the following context, the effects of Reynolds number on the eddy viscosity are further analyzed.

Figure 3.18 shows the profiles of the eddy viscosity for the two Reynolds numbers tested in this study (i.e., $Re_\tau = 650$ and 1020). These profiles are obtained from

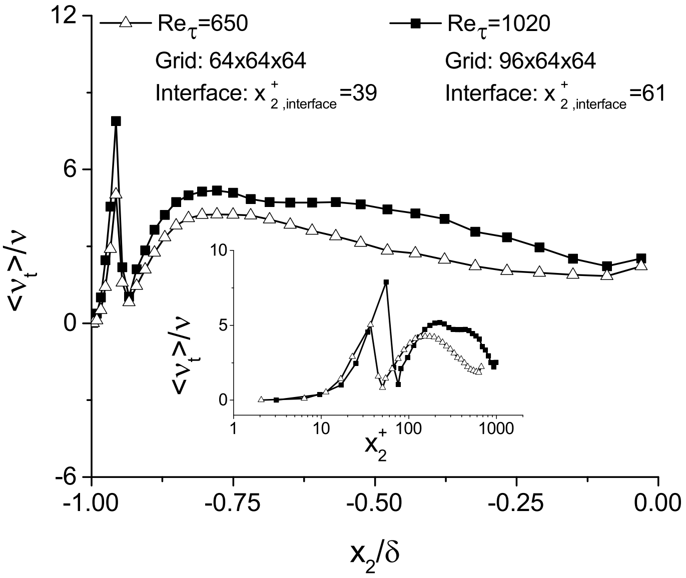

FIGURE 3.18: Eddy viscosity at $Re_\tau = 650$ and 1020 for hybrid RANS/LES with forcing applied to the entire computational domain for $0 < x_2^+ < \delta^+$ (non-dimensionalized using ν; SGS model in LES zone: SM). The small figure is re-scaled using semi-logarithmic wall coordinate x_2^+ to highlight near-wall effects.

hybrid RANS/LES with forcing applied to the entire domain for $0 < x_2^+ < \delta^+$, and non-dimensionalized using the kinematic viscosity ν. By comparing Fig. 3.18 with Fig. 3.17, it is clear that the wall-normal profile of the mean eddy viscosity is closely correlated with the modelled shear stresses. In the viscous sublayer, $\nu_t/\nu \ll 1$ strictly holds for both Reynolds numbers, implying that the level of modelled shear stress is significantly lower than that of the viscous shear stress. As x_2 increases, ν_t increases (defined in Eq. (2.10)) and peaks at the interface which is consistent with the previous observation that the modelled shear stress also peaks at the interface in Fig. 3.17. The mechanism underlying these peaks relates to the backscatter of KE produced by the proposed forcing scheme. As shown previously in Fig. 3.9, the backscatter of KE from small to large scale motions reaches the maximum at the interface, which significantly enhances the turbulence level at the boundary of the LES region (for transient simulation of turbulence). As a consequence, the level of the eddy viscosity and modelled shear stress increases drastically at the interface in Fig. 3.18 to reflect this mechanism. An enhanced level of modelled turbulence at the interface as exhibited in Figs. 3.17 and 3.18 is the key to the success of forcing modelling for properly running LES in a hybrid approach. It is interesting to note that in Fig. 3.18, within the RANS region, the eddy viscosity ratio between the two Reynolds numbers tested is approximately $\nu_{t,1020}/\nu_{t,650} = 1.6$, which matches well the ratio of the two nominal friction velocities (i.e., $u_{\tau,1020}/u_{\tau,650} = Re_{\tau,1020}/Re_{\tau,650} = 1020/650 \approx 1.6$). In fact, this 'coincidence' is strictly required by the RANS modelling equation (2.10), which demands that $\nu_t \propto u_\tau$ at a given wall-normal position x_2.

3.2.2.6 Budget of Shear Stresses

In order to further investigate the predictive performance of the proposed hybrid approach in terms of the momentum balance in the LES zone, the budget of the shear stresses across the channel is examined.

By substituting Eq. (3.4) into the filtered streamwise momentum equation (i.e., Eq. (2.20)) and then integrating the resulting equation from 0 to x_2 in the wall-normal direction, an equation that expresses the balance between the time- and plane-averaged viscous, turbulent and modelled shear stresses at an arbitrary wall-normal location x_2 is obtained:

$$\nu \frac{\partial \langle \bar{u}_1 \rangle}{\partial x_2} - \langle \bar{u}_1'' \bar{u}_2'' \rangle + \nu_t \frac{\partial \langle \bar{u}_1 \rangle}{\partial x_2} = \frac{x_2}{\rho} \frac{\partial \langle \bar{p} \rangle}{\partial x_1} + \frac{\tau_w}{\rho} \quad . \tag{3.13}$$

Two assumptions are made here: firstly, the flow is statistically stationary, and secondly, the flow is homogeneous in the x_1–x_3 plane (so, $\langle \bar{u}_2 \rangle = 0$ and $\langle \bar{u}_2'' \rangle = 0$). The three terms on the LHS of Eq. (3.13) represent the resolved viscous shear stress, resolved turbulent shear stress, and modelled shear stress, respectively. The two terms on the RHS of the equation correspond to the resolved integrated shear force due to the mean pressure gradient, and the resolved viscous shear stress at the solid wall, respectively.

Figures 3.19(a) and (b) compare the shear stress budget predicted using two different SGS models in the LES zone, namely, the SM [46] and DSM [45, 47]. All shear stress components presented in these figures have been non-dimensionalized us-

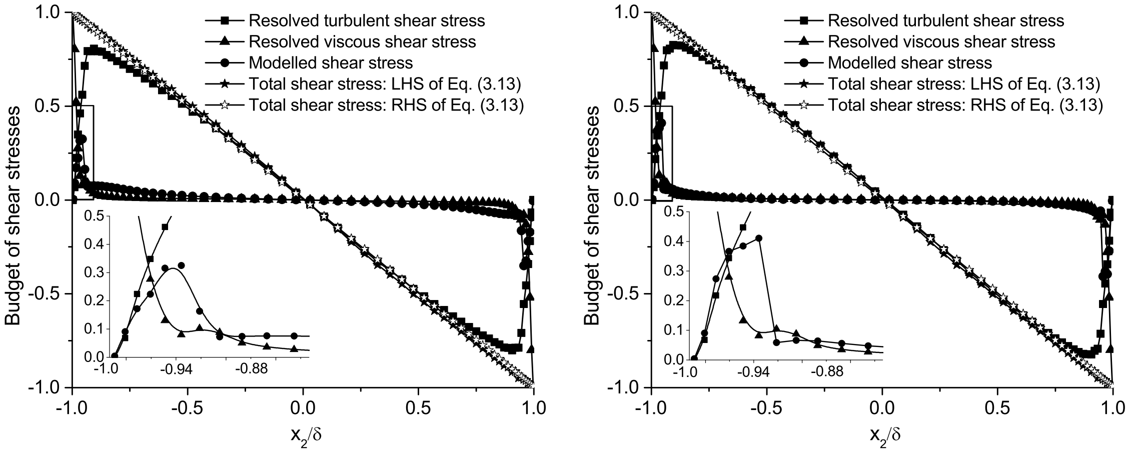

(a) SGS model: SM

(b) SGS model: DSM

FIGURE 3.19: Budget of shear stresses for hybrid RANS/LES with forcing applied to the entire computational domain for $0 < x_2^+ < \delta^+$ (non-dimensionalized using u_τ^2; $Re_\tau = 650$; grid: $64 \times 64 \times 64$; interface: $x^+_{2,\text{ interface}} = 39$). The framed areas are enlarged and shown separately using small figures.

ing the viscous shear stress term at the wall (i.e., u_τ^2). It can be clearly seen from the figures that the total shear stress calculated from the LHS of Eq. (3.13) agrees very well with that calculated from the RHS of Eq. (3.13), implying that shear stress balance predicted by both SGS models is well satisfied in the LES zone (and, this in spite of the fact that two assumptions have been made in the derivation of the shear stress balance). As expected, it is observed from Fig. 3.19 that the resolved viscous shear stress dominates in the viscous sublayer, while the resolved turbulent shear stress dominates in the fully turbulent region away from the wall. In order to clearly demonstrate the near-wall effects on the shear stress budget under investigation, Figs. 3.19(a) and (b) are partially enlarged. Both figures show clearly that as the distance from the wall increases, the time- and plane-averaged modelled shear stress component (i.e., $\nu_t \partial\langle\bar{u}_1\rangle/\partial x_2$) becomes greater than that of the viscous shear stress component. The peaks of the modeled shear stresses exhibited in Figs. 3.19(a) and (b) are direct results of the peak in the eddy viscosity shown previously in Fig. 3.18. Furthermore, by comparing the two partially enlarged figures embedded in Figs. 3.19(a) and (b), the effect of SGS modelling is observed: the modelled shear stress calculated using the SM is smaller than that calculated using the DSM. However, as analyzed above, this modelling effect does not alter the total shear stress balance prescribed by Eq. (3.13).

Chapter 4

Hybrid RANS/LES of Turbulent Flow in a Spanwise Rotating Channel

In this chapter, the predictive performance of the dynamic forcing scheme is evaluated in the context of turbulent rotating channel flows. The effects of the Coriolis force induced by a spanwise system rotation are investigated. The turbulent flow field studied herein is characterized by a Reynolds number fixed to $Re_\tau = 650$ and a wide range of rotation numbers varying from $Ro_\tau = 0$ to 15. In order to validate the hybrid approach, turbulence statistics obtained from the simulations are thoroughly compared against available experimental and DNS results.

4.1 Problem Description

Turbulent rotating channel flows are encountered in a variety of fluids engineering systems, such as the internal blade cooling system in gas turbines and rotating heat exchangers. As the Coriolis and centrifugal forces arise from the system rotation, both mean flow and turbulence level are significantly affected. Furthermore, turbulent flow structures are dramatically altered due to large secondary flows associated with the system rotation. As a consequence, the physical mechanisms underlying the transport of momentum in rotating flows are subjected to further dynamical complexities, which impose additional challenges on turbulence models to reflect and predict the effects of rotation.

The physical phenomena in a plane channel subjected to the spanwise rotation are of fundamental interests to the fluids community and have been reported in both experimental and numerical studies [20, 69–71]. The effect of the Coriolis force on the flow field can be quantified by a parameter $s \overset{\text{def}}{=} -2\Omega/(d\langle\bar{u}_1\rangle/dx_2)$. Here, $\langle\cdot\rangle$ denotes a quantity averaged both in time and over the homogeneous (x_1, x_3)-plane. Figure 4.1 shows the computational domain and coordinate system of a plane channel rotating in the spanwise direction at a constant angular speed Ω. As demonstrated by Johnston *et al.* [69], parameter s represents the ratio of the production rate due to the rotational shear stresses (i.e., $4\Omega\langle\bar{u}_1''\bar{u}_2''\rangle$) to the production rate due to the mean turbulent shear stresses (i.e., $-2\langle\bar{u}_1''\bar{u}_2''\rangle(d\langle\bar{u}_1\rangle/dx_2)$) in the simplified transport equation for the streamwise turbulent normal stress. According to the conventional criterion for characterizing rotation effects [72], turbulent mixing is enhanced on the side of the channel where the streamwise momentum is unstably stratified (also being referred to the destabilized or pressure side) when $-1 < s < 0$, whereas turbulent mixing is reduced on the opposite side of the channel where the streamwise momentum is stably stratified (also being referred to the stabilized or suction side) when $s > 0$.

The rotation effects and conventional criterion [72] mentioned above have been widely confirmed by laboratory measurements. Johnston *et al.* [69] conducted an experimental study on fully-developed turbulent flow in a spanwise rotating duct using both dye and hydrogen-bubble visualization methods. They observed augmentation and suppression of turbulence on the pressure and suction side, respectively. Furthermore, they were able to visualize Taylor-Görtler (T-G) vortices near the pressure side, which extended to the central core region of the channel in their experiment. It has been confirmed that T-G vortices are large longitudinal roll cells, which appear in pairs and have a significant impact on the spanwise distribution of mean flow quantities. Watmuff *et al.* [70] performed measurements using hot-wire anemometers to investigate a zero-pressure-gradient turbulent boundary layer subjected to spanwise system rotations. In their experiment, the mean velocity profiles affected by the rotation were described using a common universal viscous sublayer and modified logarithmic and wake regions. Due to the influence of T-G vortices, periodic spanwise variations of the skin friction coefficient were observed by Watmuff *et al.* [70] in the destabilized layer. Nakabayashi and Kitoh [73] carried out dimensional analysis and hot-wire measurements of spanwise rotating channel flows at low Reynolds numbers. They concluded that the level of turbulence is influenced simultaneously by both rotation and Reynolds number. The law of the wall for the mean velocity profile obtained by Nakabayashi and Kitoh [73] shows that in addition to the common viscous and buffer layers (as for a non-rotating channel flow), an extra layer where rotation effects predominate exists in a rotating channel flow. In their follow-up experiment, Nakabayashi and Kitoh [74] further suggested that the Coriolis force makes a large contribution to the transport of the Reynolds shear stresses owing to the accompanied strong ejection effects. It was observed that the ejection occurs periodically on the pressure side in response to the motion of T-G vortices induced by the spanwise system rotation. Instead of using hot-wire anemometers as in the experiments of Watmuff *et al.* [70] and Nakabayashi and Kitoh [73, 74], Bons and Kerrebrock [75] measured the full flow field in rotating channels using particle image velocimetry (PIV). However, the imaging system in their experiments was not attached to the rotating test section. Instead, the camera was fixed to a stationary frame and triggered at each passing of the rotating test section. The relative velocity was then obtained by subtracting the peripheral velocity from the measured absolute velocity. Unfortunately, as indicated by Di Sante *et al.* [76], such a method can result in low temporal and spatial resolutions and can cause large uncertainties in measurements especially at a high angular system rotation speed.

Besides experimental measurements, numerical studies have been extensively conducted to provide physical insights into the effects of system rotation on the flow field. Among these numerical studies, the RANS methods have been primarily focused on examination of the predictive performance of turbulence models. For instance, Belhoucine *et al.* [77] performed RANS simulations to study a rotating duct flow based on use of explicit algebraic Reynolds stress models. By taking the anisotropic dissipation into account, a RANS approach is capable of predicting the effects of the Coriolis force on the mean flow and turbulence structures. Different from the RANS method in which all scales of turbulent motions are modelled, no turbulence modelling is involved in a DNS approach as all scales of turbulent motions (from the largest integral scales to the finest Kolmogorov scale) are directly computed. In the DNS of Kristoffersen and Andersson [20], it has been demonstrated that the T-G vortices are intrinsically unstable and are free to wander in the spanwise direction, and they contribute significantly (up to 25%) to the total TKE. Grundestam *et al.* [71] performed DNS studies on fully-developed rotating channel flows at a fixed Reynolds number $Re_\tau = 180$ and multiple rotation numbers within the range $0 \leq Ro_b \leq 3.0$. Here, $Ro_b \overset{\text{def}}{=} 2\Omega\delta/U_b$ is the rotation number based on the bulk mean velocity U_b. The DNS results of Grundestam *et al.* [71] clearly suggest that complete flow laminarization occurs at $Ro_b = 3.0$. As revealed in the DNS study of Wallin *et al.* [78], the process of laminarization is strongly dominated by linear mechanisms of the Tollmien-Schlichting waves. In addition to the RANS and DNS approaches reviewed above, LES has also been employed to study turbulent flows subjected to system rotations. The LES method is effective in resolving the evolution of a flow field at scales that are larger than a certain filter size, therefore, it is more computationally affordable than the DNS approach. Pallares and Davidson [79] investigated the influence of system rotation on the spatial distribution of the mean velocity and Reynolds stresses. In their LES study, the Coriolis force tends to significantly reduce the overall turbulence level of the flow at a low Reynolds number. In the LES study of Xun *et al.* [80], the previous experimental observation of Watmuff *et al.* [70] that T-G vortices can cause quasi-periodicity in the spanwise distribution of the skin friction coefficient and Nusselt number has been confirmed. In another study, Xun *et al.* [61] presented both the general and simplified transport equations for the resolved turbulent stresses in the context of LES. They reported thoroughly the effects of spanwise system rotation on the transport of the resolved TKE and the interactions between small-scale flow structures for a low Reynolds number flow.

Application of DNS and LES to turbulent rotating channel flows at higher Reynolds numbers represents a challenge in the area of CFD. Firstly, as the wall is approached, viscous forces become dominant, and the computational resources needed for resolving the viscous scales increase exponentially. Tennekes and Lumley [4] indicated that the number of grid points needed to perform a 3-dimensional (3-D) DNS is proportional to Re_ℓ^3 (based on integral length scale ℓ), and Chapman [7] estimated that the number of grid points is proportional to $Re_\ell^{1.8}$ for LES to resolve the wall shear layer. Secondly, in comparison with the conventional case of a turbulent plane channel flow (without rotation), a finer grid resolution is required for LES and DNS to resolve the wall shear layer on the pressure side of a turbulent channel flow subjected to the spanwise system rotation. This is because as the flow becomes more turbulent on the pressure side, the local Reynolds number on the pressure side increases drastically with the presence of Coriolis forces. Due to these two limitations, previous numerical studies [20, 61, 71, 78, 80] on rotating flows using either DNS or LES have primarily focused on low Reynolds numbers flow for $Re_\tau \leq 194$.

In this chapter, the predictive performance of the dynamic forcing scheme represented by Eq. (2.22) is further examined in the context of a special body force (i.e., the Coriolis force). The turbulent channel flows subjected to the spanwise system rotation are characterized by a nominal Reynolds number $Re_\tau = 650$. Due to the presence of Coriolis forces, the velocity field becomes statistically asymmetrical in the wall-normal direction. The flow becomes destabilized on the pressure side and stabilized on the suction side of the channel. Correspondingly, the local Reynolds number increases and decreases considerably on the pressure and suction side, respectively. These interesting physical features of the spanwise rotating channel flow impose additional challenges to the test of the forcing scheme for hybrid RANS/LES.

4.2 Numerical Aspects

Figure 4.1 shows the computational domain and coordinate system of the rotating plane channel used in numerical simulations. The dimensions of the computational domain are $L_1 \times L_2 \times L_3 = 2.5\pi\delta \times 2\delta \times 2\pi\delta$ in the streamwise (x_1), wall-normal (x_2) and spanwise (x_3) directions, respectively. The turbulent flow field is characterized by a Reynolds number $Re_\tau = 650$ and a rotation number Ro_τ varying from 0 to 15.

A grid system consisting of $64 \times 64 \times 128$ control volumes (in the streamwise, wall-normal and spanwise directions, respectively) was used for all hybrid simulations. The grid is uniform in the streamwise and spanwise directions, and stretched in the wall-normal direction using a hyperbolic-tangent function in order to provide a greater resolution in the near-wall region. The size of control volumes in the wall-normal direction is given in Eq. (3.2). In this chapter, the proposed hybrid approach is evaluated based on the combination of algebraic closure models (i.e., the mixing length model for RANS region and the DSM of Lilly [47] for LES region) and the dynamic forcing scheme represented by Eq. (2.22). As demonstrated in chapter 3, the proposed dynamic forcing scheme for the hybrid RANS/LES approach is insensitive to the choices of the forcing region or interface location. Based on these observations, the forcing model represented by Eq. (2.22) were applied to the entire computational domain, and the interface location that separates the RANS and LES zones was explicitly specified at $x_2^+ \overset{\text{def}}{=} x_2 u_\tau / \nu = 39$.

No slip and impermeable boundary conditions were imposed on the velocity components at the walls. Periodic boundary conditions were employed in the streamwise and spanwise directions since the flow field is assumed to be statistically homogeneous in these two directions. Statistics of various flow variables were calculated based on 80,000 time steps after the flow field became fully developed.

4.3 Results and Discussions

In order to assess the predictive performance of the dynamic forcing scheme on a spanwise rotating channel flow, the results obtained from hybrid RANS/LES are compared against available laboratory measurements [69] and DNS results [20, 63, 71]. The effects of rotation number and Reynolds number on the flow field will be investigated, and prototypical features including turbulence structures, first- and second-order flow statistics, and budget of shear stresses will be examined. Furthermore, the 'dynamic'

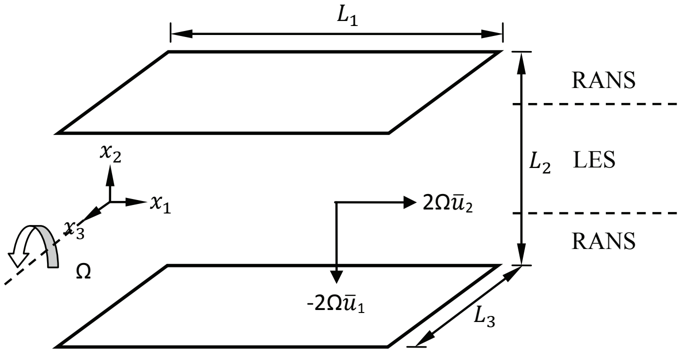

FIGURE 4.1: Computational domain for hybrid RANS/LES of a spanwise rotating channel flow. Specific to this rotating channel flow, the pressure (destabilizing) side wall is located at $x_2/\delta = -1.0$, and the suction (stabilizing) side wall is located at $x_2/\delta = 1.0$.

feature of the forcing model in terms of its role in capturing the rotation effects will be demonstrated by analyzing the rate of SGS KE backscatter.

4.3.1 Reynolds Numbers and Rotation Numbers

A flow in the spanwise rotating channel is characterized by a Reynolds number and a rotation number, both of which can be defined based on either the bulk mean velocity U_b or the friction velocity u_τ, i.e., $Re_b \overset{\text{def}}{=} U_b\delta/\nu$ or $Re_\tau \overset{\text{def}}{=} u_\tau\delta/\nu$, and $Ro_b \overset{\text{def}}{=} 2\Omega\delta/U_b$ or $Ro_\tau \overset{\text{def}}{=} 2\Omega\delta/u_\tau$. These definitions of Reynolds and rotation numbers have been widely used in literature [20, 61, 71, 80]. In the following analysis, Re_τ and Ro_τ are used as the controlling parameters to characterize the rotating flows under simulation following the approach of Kristoffersen and Andersson [20]. On the other hand, as results of the simulation, Re_b and Ro_b are considered as output parameters. In the above equations, subscripts 'b' and 'τ' are used to denote a variable calculated based on the bulk mean velocity U_b and the friction velocity u_τ, respectively. The bulk mean velocity is defined as $U_b = \int_{-\delta}^{\delta} \langle \bar{u}_1 \rangle \, dx_2/2\delta$, and the friction velocity is determined as

$$u_\tau = \sqrt{-\frac{\delta}{\rho}\frac{\partial\langle\bar{p}\rangle}{\partial x_1}} \quad . \tag{4.1}$$

Because the flow is driven by a prescribed constant pressure gradient $\partial\langle\bar{p}\rangle/\partial x_1$, the value of u_τ and also that of Re_τ are determined for a fully-developed channel flow.

Table 4.1 summarizes the values of Reynolds numbers and rotation numbers in the current hybrid simulations. As the controlling parameters, the Reynolds number Re_τ is fixed to 650, and the rotation number Ro_τ varies from 0 to 15. As the output parameters, the corresponding values of the Reynolds number and rotation number based on the bulk mean velocity (Re_b and Ro_b, respectively) for the 6 test cases are given in Table 4.1. Values of three other Reynolds numbers, namely, $Re_{\tau p}$, $Re_{\tau s}$ and Re_τ^a are also presented. These Reynolds numbers are defined based on $u_{\tau p}$, $u_{\tau s}$ and u_τ^a, respectively. Here, the modifying subscripts 'p' and 's' are used to denote the region near pressure and suction sides, respectively; and superscript 'a' denotes averaging over both walls. When rotation is imposed on the flow, the channel is divided into a pressure (unstable) and a suction (stable) side. The wall shear stresses on the two sides of the rotating channel become different, which results in different friction velocities $u_{\tau p}$ and $u_{\tau s}$ on the pressure and suction side of the channel, respectively. Because the streamwise pressure gradient is balanced by both wall shear stresses, the following relationship holds

$$u_\tau = \sqrt{\frac{\tau_{wp} + \tau_{ws}}{2\rho}} = \sqrt{\frac{u_{\tau p}^2 + u_{\tau s}^2}{2}} \quad . \tag{4.2}$$

Here, subscript 'w' is used to indicate the value of a variable at the channel wall. In numerical simulations, as demonstrated in the DNS study of Kristoffersen and Andersson [20], the values calculated using Eq. (4.2) underpredict u_τ by maximum 4.1%. As an alternative to u_τ, an averaged friction velocity over both pressure and suction walls can be considered [61, 80], which is defined as

$$u_\tau^a = \frac{u_{\tau p} + u_{\tau s}}{2} \quad . \tag{4.3}$$

Because both u_τ and u_τ^a are popular in the literature of rotating channel flows, care must be taken on the small differences in their values in order to understand and make

TABLE 4.1: Test cases for hybrid RANS/LES of a fully-developed plane channel flow subjected to spanwise system rotations.

Case	Rotation numbers		Reynolds numbers				
	Ro_τ	Ro_b	Re_τ	$Re_{\tau p}$	$Re_{\tau s}$	Re_τ^a	Re_b
1	0	0	650	649.2	648.7	649.0	19630.0
2	1.5	0.05	650	707.0	589.2	648.1	19731.6
3	2.5	0.08	650	726.1	563.8	645.0	19760.0
4	4.5	0.15	650	744.9	540.2	642.6	20145.1
5	7.5	0.24	650	756.2	502.7	629.5	20616.2
6	15	0.45	650	764.4	469.0	616.7	21441.1

precise comparisons of various reported results. As shown in Table 4.1, the value of u_τ^a calculated from Eq. (4.3) agrees with that of u_τ very well when the rotation number is low. However, as the rotation number increases, the discrepancy between the values of u_τ and u_τ^a increases. For the hybrid simulations conducted in the current study, this discrepancy can reach up to 4.8%.

Figure 4.2(a) shows the correlation between U_b and u_τ as a function of the rotation number. For the purpose of comparison, two sets of DNS data obtained by Grundestam *et al.* [71] at $Re_\tau = 180$ (designated as GWJ-2008) and Kristoffersen and Andersson [20] at $Re_\tau = 194$ (designated as KA-1993), and one set of full LES data obtained by Xun *et al.* [61] at $Re_\tau = 150$ (designated as XWY-2011) are also shown in the figure. For the non-rotating flow case (i.e., $Ro_\tau = 0$), the results predicted by all these simulations (based on different numerical methods and Reynolds numbers) collapse, and the current simulation indicates that $U_b/u_\tau = 15.1$. As shown in Fig. 4.2(a), for the rotating flows, U_b increases with Ro_b, which trend is in agreement with that of Grundestam *et al.* [71]. From Table 4.1, it is clear that the value of $Re_{\tau p}$ increases considerably as the rotation number increases. Owing to the low Reynolds number tested ($Re_\tau = 180$), Grundestam *et al.* [71] were able to perform DNS at very high rotation numbers. According to their research, when the rotation number further increases, the value of ratio U_b/u_τ increases favourably, and eventually reaches 60 for a completely laminarized flow state.

Figure 4.2(b) shows the values of $u_{\tau p}/u_\tau$ and $u_{\tau s}/u_\tau$ obtained at different rotation

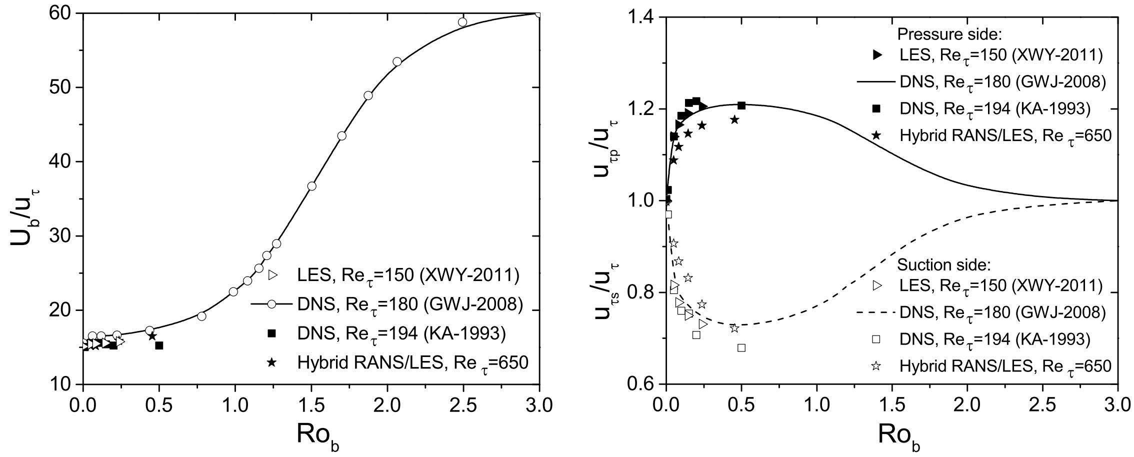

(a) U_b/u_τ

(b) $u_{\tau p}/u_\tau$ and $u_{\tau s}/u_\tau$

FIGURE 4.2: Rotation effects on the bulk mean velocity U_b and wall friction velocity $u_{\tau p}$ (for the pressure side) and $u_{\tau s}$ (for the suction side). The profiles are non-dimensionalized using u_τ.

numbers. As shown in the figure, the profiles of $u_{\tau p}$ and $u_{\tau s}$ obtained at $Re_\tau = 650$ using hybrid RANS/LES are generally in agreement with those in Kristoffersen and Andersson [20] and Grundestam *et al.* [71] using DNS, especially when Ro_b is low. However, small differences indeed exist due to the difference in Reynolds numbers of these test cases. The distinct characteristics of $u_{\tau p}$ and $u_{\tau s}$ shown in Fig. 4.2(b) effectively demonstrate the impacts of system rotations on a flow field. In response to the spanwise rotation, $u_{\tau p} > u_{\tau s}$ holds strictly. Corresponding to this velocity difference, the flow on the pressure side tends to become more turbulent and the boundary layer tends to become thinner, whereas the flow on the suction side tends to become more laminarized and the boundary layer tends to become thicker. This phenomenon is typically referred to as the 'Ekman layer effect', and is caused by the balance between the Coriolis force, mean pressure gradient and turbulent drag in a layer of flow subjected to a system rotation. The Ekman layer effect will be investigated in more details later in section 5.3.5 by examining the profiles of mean velocity.

4.3.2 Taylor-Görtler Vortices

Due to the existence of Coriolis forces, the flow field in a rotating channel is significantly altered from that without rotation. Typical for a rotating turbulent channel flow, large longitudinal roll cells exist in the time-averaged velocity field. This phenomenon has been reported in many previous investigations, including, e.g. the laboratory experiment of Johnston *et al.* [69] and DNS study of Kristoffersen and Andersson [20]. These large longitudinal roll cells appear in pairs and are interpreted as T-G vortices analogous to those arising from the flow instability mechanism associated with streamline curvatures [81–83]. In the following context, both instantaneous and time-averaged flow fields are studied in order to investigate the effects of Coriolis forces on flow structures in a rotating channel.

Figure 4.3 compares instantaneous vortex structures in the central cross-stream (x_2, x_3)-plane at different rotation numbers. The vortex structures shown in the figure are visualized using contours of instantaneous streamwise vorticity ω_1. In order to investigate the rotation effects on the vortex structures, the contour legend scale is kept identical in Figs. 4.3(a)-(c) for three different rotation numbers. As shown in Fig. 4.3(a), for the non-rotating flow case ($Ro_\tau = 0$), vortex features near the two channel walls are very similar. In the near-wall region, fine flow structures (indicated by contours of both positive and negative values of ω_1) swirl around each other in an intense manner. As the center of the channel is approached, the swirling vortex structures become larger and the magnitude of ω_1 becomes significantly reduced. As shown in Fig. 4.3(b), when the channel is imposed with rotation ($Ro_\tau = 7.5$), vortex structures near the pressure side (bottom wall) and suction side (upper wall) become different. Flow motions with large magnitude of vorticity (which originate from the pressure side) can directly reach the core region of the channel. As a consequence, the flow in the central part of the channel in Fig. 4.3(b) is seen to be more disturbed in comparison with that in the non-rotating channel shown in Fig. 4.3(a). At a higher rotation number for $Ro_\tau = 15$ as shown in Fig. 4.3(c), on the suction side, vortex structures become predominantly aligned with the spanwise direction. By comparing

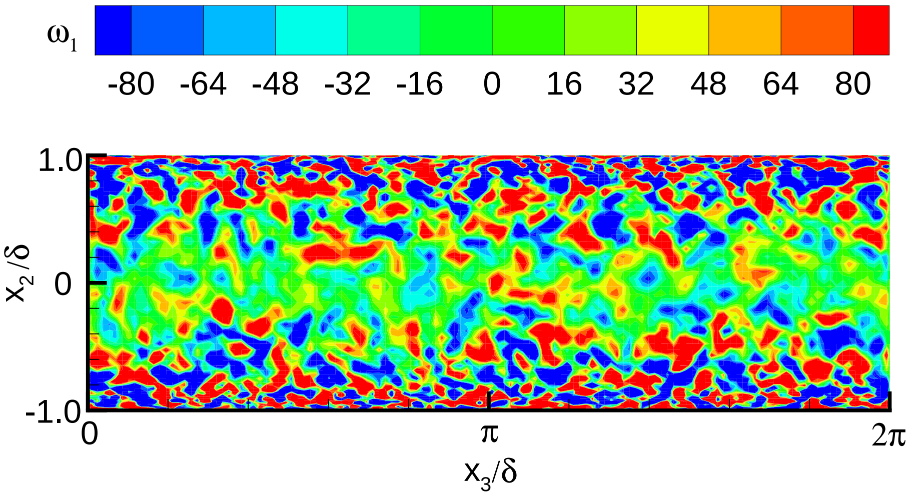

(a) $Ro_\tau = 0$

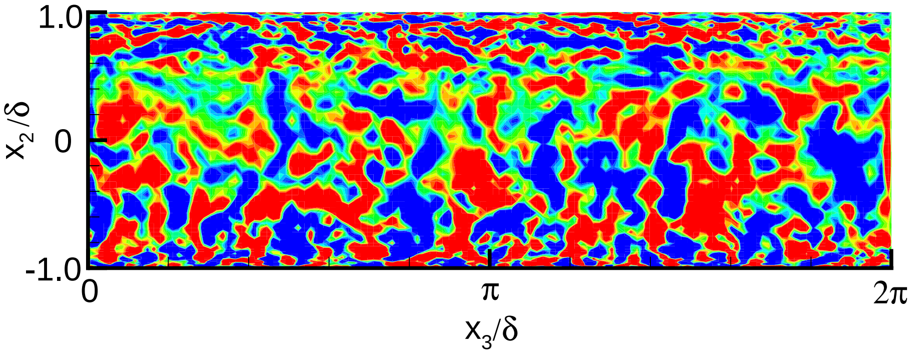

(b) $Ro_\tau = 7.5$

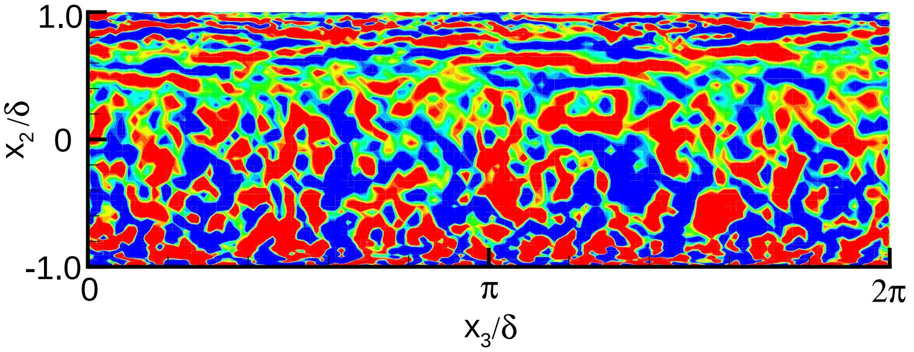

(c) $Ro_\tau = 15$

FIGURE 4.3: Contours of instantaneous streamwise vorticity obtained at different rotation numbers. The pressure (destabilizing) side wall is located at $x_2/\delta = -1.0$, and the suction (stabilizing) side wall is located at $x_2/\delta = 1.0$.

Fig. 4.3(c) with Fig. 4.3(b), it is evident that swirling motions are further suppressed near the suction side of the channel as the rotation number increases. As shown in

Fig. 4.3(c), on the pressure side, vortex structures with large magnitude of streamwise vorticity penetrate deeply into the central core. This contributes significantly to the transport of low-speed fluid parcels from the near-wall region into the core region of the channel, and as a result, the transfer of momentum is enhanced on the pressure side.

Owing to the system rotation, T-G vorticies are induced by the Coriolis force and appear as large organized secondary flow structures close to the pressure side of the rotating channel, which then have a significant impact on properties of the flow field, such as the mean velocity, skin friction coefficient, Nusselt number and Reynolds shear stresses [20,61,69,70,74,80]. Therefore, precise prediction of T-G vortices is essential for validating a forcing model for hybrid RANS/LES. Based on the assumption that the T-G vortices appear as near-circular roll cells occupying the entire cross-sectional area, Kristoffersen and Andersson [20] developed an approximate correlation between the number of T-G vortex pairs and the aspect ratio between the width and height of the channel, viz. $N = \text{int}(\frac{1}{2}L_3/L_2)$. Following the DNS study of Kristoffersen and Andersson [20], the aspect ratio is set to $L_3/L_2 = \pi$ in this study.

Figure 4.4 shows the time-averaged velocity field in the central cross-stream (x_2, x_3)-plane for $Ro_\tau = 2.5$ and 15. As shown in Fig. 4.4(a), two pairs of persistent T-G vortices are observed at $Ro_\tau = 2.5$. As rotation number increases to $Ro_\tau = 15$, the number of T-G vortex pairs increases to three in Fig. 4.4(b). The reason that the number of T-G vortex pairs increases with the increase of the rotation number Ro_τ lies in the fact that the flow layer on the suction side becomes thicker and more stable at a higher Ro_τ, which in turn reduces the vertical spacing (or, effective height) of the core turbulent region. As a result, the number of T-G vortex pairs increases in a narrower effective core turbulent region in the cross-stream plane. It is worthwhile to note that in the previous DNS study of Kristoffersen and Andersson [20] for $Re_\tau = 194$, and LES study of Xun *et al.* [61,80] for $Re_\tau = 150$, two and three persistent pairs of T-G vortices were observed (with the same aspect ratio of the channel for $L_3/L_2 = \pi$) at $Ro_\tau = 2.5$ and 7.5, respectively. In this study, because a much higher Reynolds number $Re_\tau = 650$ is tested, a higher rotation number $Ro_\tau = 15$ is required to form a

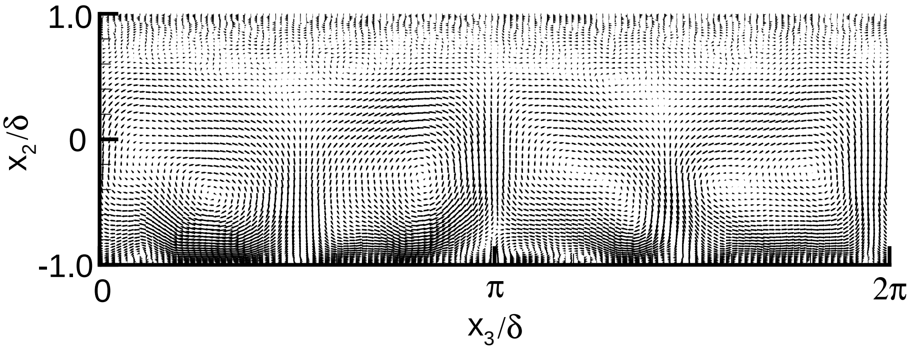

(a) $Ro_\tau = 2.5$

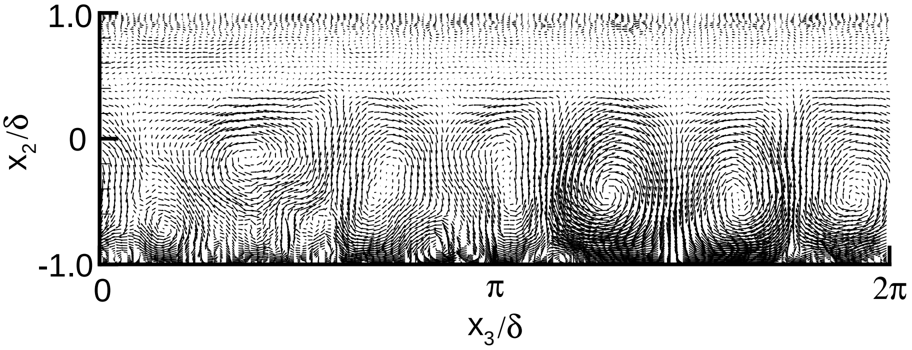

(b) $Ro_\tau = 15$

FIGURE 4.4: Taylor-Görtler vortices for $Ro_\tau = 2.5$ and 15, extracted from time-averaged velocity field in the central cross-stream (x_2, x_3)-plane at the downstream location $x_1/\delta = 1.25\pi$.

thick stabilized flow layer on the suction side (to reduce the effective vertical spacing of the core turbulent region) in order to facilitate development of three pairs of T-G vortices.

4.3.3 Mean Resolved Velocity

Figure 4.5 shows the mean resolved streamwise velocity profiles in the wall-normal direction across the channel. A set of DNS data on non-rotating channel flow ($Re_\tau = 650$ and $Ro_\tau = 0$) obtained by Iwamoto *et al.* [63] (designated as ISK-2002) is also included in the figure for the purpose of comparison. As shown in Fig. 4.5, the mean velocity profile is symmetric about the central channel plane ($x_2/\delta = 0$) for the non-rotating case ($Ro_\tau = 0$). However, for the rotating case ($Ro_\tau = 7.5$), the symmetry

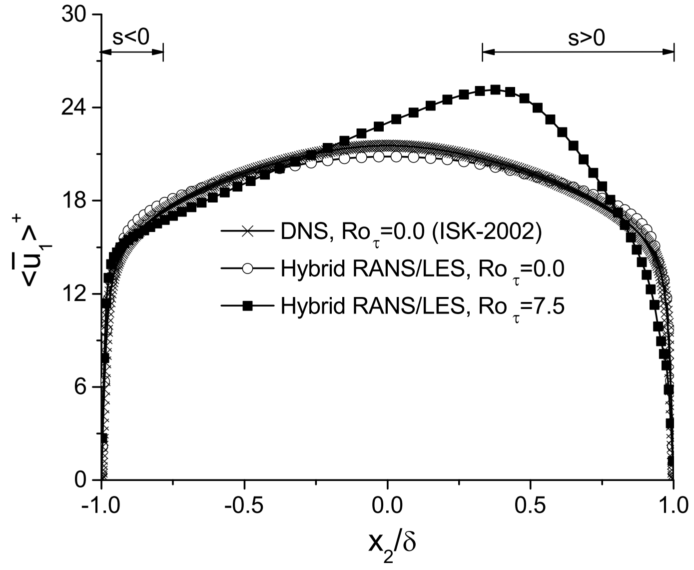

FIGURE 4.5: Resolved mean streamwise velocity obtained at $Ro_\tau = 0$ and 7.5 (non-dimensionalized using u_τ).

is broken. From Fig. 4.5, it is evident that $d\langle \bar{u}_1 \rangle / dx_2 > 0$ holds in the region near the pressure side (i.e., at $x_2/\delta = -1.0$), which results in $s < 0$, indicating that the system rotation has a destabilizing effect on the flow field near the pressure side. In contrast, near the suction side (i.e., at $x_2/\delta = 1.0$), $d\langle \bar{u}_1 \rangle / dx_2 < 0$, a condition that results in $s > 0$, indicating that system rotation has a stabilizing effect on the flow field near the the suction side. Furthermore, it is clearly shown in Fig. 4.5 that at $Ro_\tau = 7.5$, the mean streamwise velocity profile shifts to the pressure side. This is owing to the presence of large T-G vortices induced by the spanwise system rotation. These T-G vortices promote the transport of high-speed fluid from the core region of the channel towards the pressure wall (see also the qualitative visualization result presented previously in Fig. 4.4).

The rotation effect on the flow field can be also examined by comparing the wall shear stresses at the two (i.e., pressure and suction) sides of the rotating channel. The wall shear stress of the rotating channel flow is enhanced near the pressure side and reduced near the suction side because $|d\langle \bar{u}_1 \rangle / dx_2|_{wp} > |d\langle \bar{u}_1 \rangle / dx_2|_{ws}$ (which is evident in Fig. 4.5 by comparing the values of the wall-normal gradient of the mean resolved streamwise velocity $|d\langle \bar{u}_1 \rangle / dx_2|_w$ for the rotating and non-rotating cases).

The increase and reduction of wall shear stress on the pressure and suction sides, respectively, directly influence the values of $u_{\tau p}$ and $u_{\tau s}$ (demonstrated previously in Fig. 4.2 (b)). As a consequence, the Reynolds number based on the wall friction velocity becomes different on the two sides of the channel (see Table 4.1). For example, at $Ro_\tau = 7.5$, $Re_{\tau p} = 756.2$ and $Re_{\tau s} = 502.7$ (recall that for the non-rotating case, $Re_{\tau p} = Re_{\tau s} = 650$).

From previous experimental and DNS studies [20, 69], it is known that a relationship $s = -2\Omega/(d\langle\bar{u}_1\rangle/dx_2) = -1$ holds in the core region of a rotating channel, implying that the value of the mean shear vorticity component $d\langle\bar{u}_1\rangle/dx_2$ approaches 2Ω. As such, the absolute mean angular speed of the flow becomes approximately zero in the core region of the channel, i.e.

$$2\Omega - d\langle\bar{u}_1\rangle/dx_2 \approx 0 \quad . \tag{4.4}$$

This particular portion of the velocity profile corresponds to a flow region of neutral stability [20]. The neutral stability relationship represented by Eq. (4.4) can be further integrated and written in a dimensionless form, viz.

$$\langle\bar{u}_1\rangle^+ = Ro_\tau \cdot \frac{x_2}{\delta} + C \quad , \tag{4.5}$$

where C is a constant of integration. As shown in Fig. 4.6, the profiles become increasingly asymmetric as the rotation number increases. In the core region, the profiles become approximately linear with slope Ro_τ when rotation is imposed. These findings are fully consistent with the laboratory measurements of Johnston *et al.* [69] and the DNS results of Kristoffersen and Andersson [20].

Figure 4.7 shows the thickness (denoted as d) of the neutral stability zone for $Re_\tau = 650$ at different rotation numbers. In order to examine the Reynold number effect on the thickness of the neutral stability zone, the DNS results ($Re_\tau = 150$ and $Ro_\tau = 2.5$) obtained by Nishimura and Kasagi [84] (designated as NK-1996) and the LES results ($Re_\tau = 150$ and $0 \leq Ro_\tau \leq 7.5$) obtained by Xun *et al.* [61] (designated as

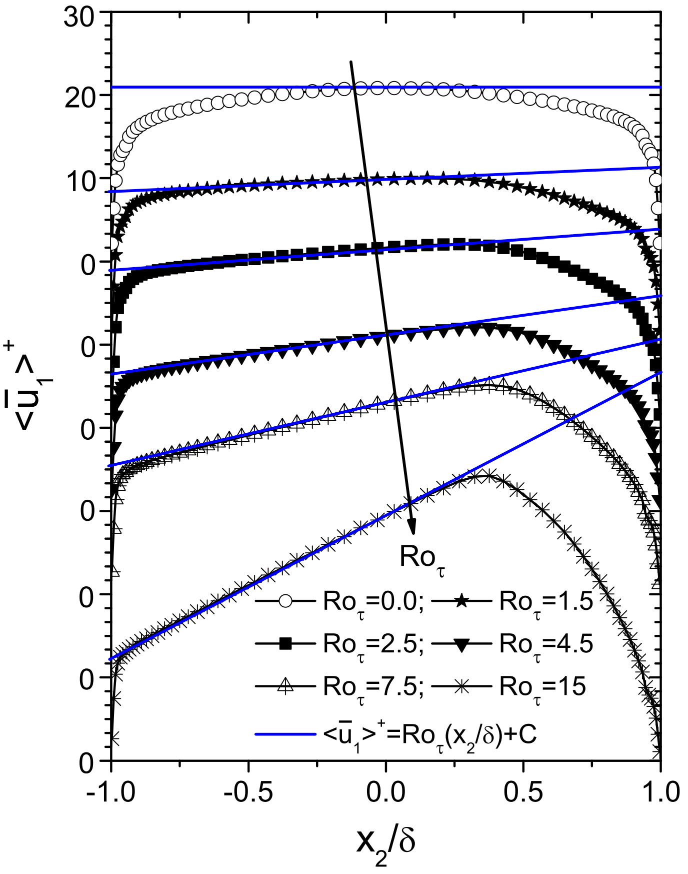

FIGURE 4.6: Resolved mean streamwise velocity obtained at different rotation numbers (non-dimensionalized using u_τ).

XWY-2011) are also presented in the figure. As shown in Fig. 4.7, for both Reynolds numbers, the thickness of the neutral stability zone increases as Ro_τ increases. With regard to the Reynolds number effects, it is obvious in Fig. 4.7 that d has a larger value at $Re_\tau = 650$ than that at $Re_\tau = 150$, under the same rotation number Ro_τ. This implies that the neutral stability zone is stretched wider in the central core of the channel at a higher Reynolds number. As the Reynolds number increases, the inertial forces increase, which work against the laminarization trend near the suction side.

Figure 4.8 displays the mean resolved streamwise velocity profiles for various rotation numbers (ranging from $Re_\tau = 0$ to 15). The wall coordinates in Fig. 4.8 are calculated by using $u_{\tau p}$ on the pressure side and by using $u_{\tau s}$ on the suction side. As shown in Fig. 4.8, mean velocity profiles on the suction side are strikingly different

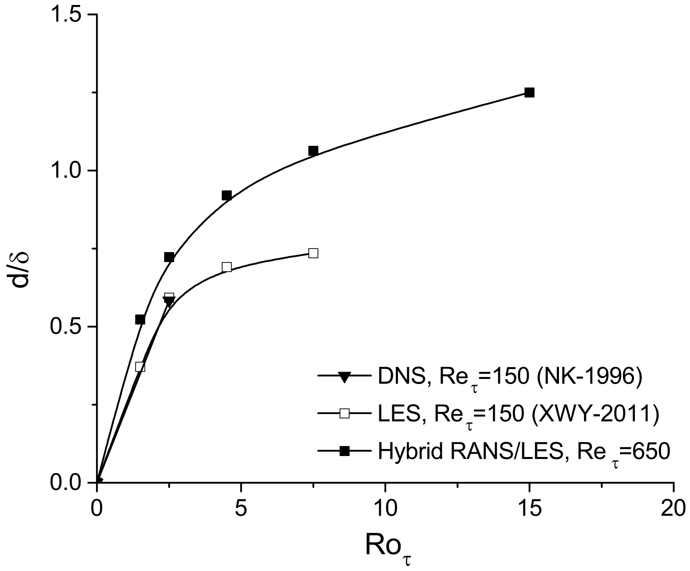

FIGURE 4.7: Thickness of the neutral stability zone obtained at different rotation numbers (non-dimensionalized using the half channel height δ).

from those on the pressure side. In comparison with the profile for the non-rotating case, the profile of the mean resolved velocity shifts upwards on the suction side and downwards on the pressure side for all the rotating cases. This is a classical pattern widely reported in previous investigations of spanwise rotating channel flows, e.g., in the DNS study of Kristoffersen and Andersson [20] and LES study of Xun *et al.* [61, 80]. As shown in Fig. 4.8, at $Ro_\tau = 15$, the profile of $\langle \bar{u}_1 \rangle^+$ on the pressure side deviates the most from the linear law-of-the-wall $\langle \bar{u}_1 \rangle^+ = x_2^+$ characteristic of the viscous sublayer within $x_2^+ < 10.8$ (based on von Kármán's two-layer boundary-layer model), indicating that the influence of the Coriolis force has penetrated through the buffer layer and extended deeply into the near-wall region. This observation is consistent with the DNS result of Kristoffersen and Andersson [20]. As is evident from the figure, on the suction side, as Ro_τ increases, the portion of the linear law-of-the-wall becomes increasingly extended in the profile of $\langle \bar{u}_1 \rangle^+$. This indicates that as the rotation number increases, the flow becomes increasingly dominated by the viscous shear stresses on the suction side of the channel. As such, the flow tends to become more laminarized.

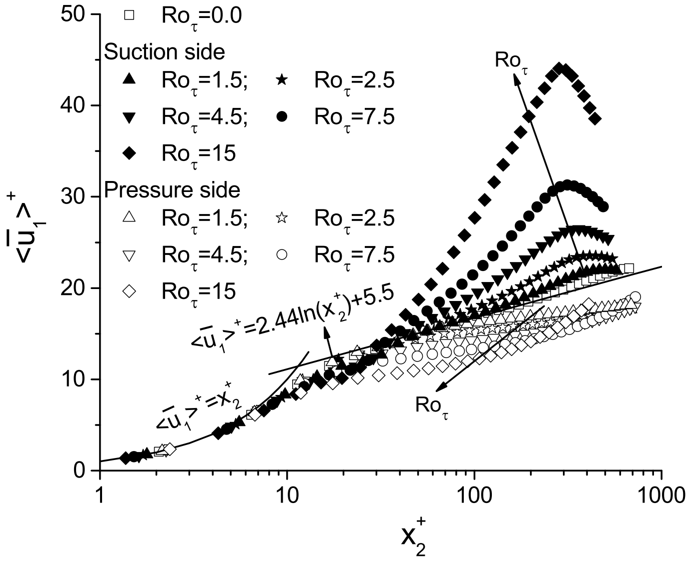

FIGURE 4.8: Resolved mean streamwise velocity obtained at different rotation numbers. The wall coordinates are calculated by using $u_{\tau p}$ on the pressure side and $u_{\tau s}$ on the suction side.

4.3.4 Second-Order Flow Statistics

Figure 4.9 compares RMS velocities obtained for the non-rotating flow case (at $Ro_\tau = 0$) and rotating flow case (at $Ro_\tau = 7.5$). As shown in Fig. 4.9, in general, the trends of the resolved RMS velocities predicted by hybrid RANS/LES are in agreement with the DNS data for the non-rotating case ($Ro_\tau = 0$). However, small differences are observed: the hybrid method tends to slightly underpredict the wall-normal and spanwise components of the resolved RMS velocity, especially in the central region of the channel. When the channel is imposed with rotation (demonstrated using the case of $Ro_\tau = 7.5$), the magnitude of all three components of the resolved turbulent intensity becomes much higher on the pressure side than on the suction side, indicating that the flow on the pressure side is more turbulent than that on the suction side. Furthermore, a nearly constant level of $\bar{u}^+_{1,\mathrm{rms}}$ can be seen from Fig. 4.9(a) within the range $-0.75 \leq x_2/\delta \leq 0.25$, which corresponds to the neutral stability zone for $Re_\tau = 650$ and $Ro_\tau = 7.5$ demonstrated previously in Figs. 4.5–4.7.

From the previous analysis, it is understood that the Coriolis force (and the T-G vortices induced by it) drastically changes the level of the first-order flow statistics

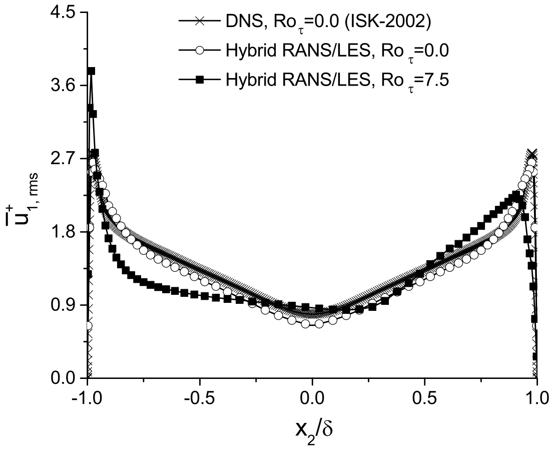

(a) RMS of the streamwise velocity

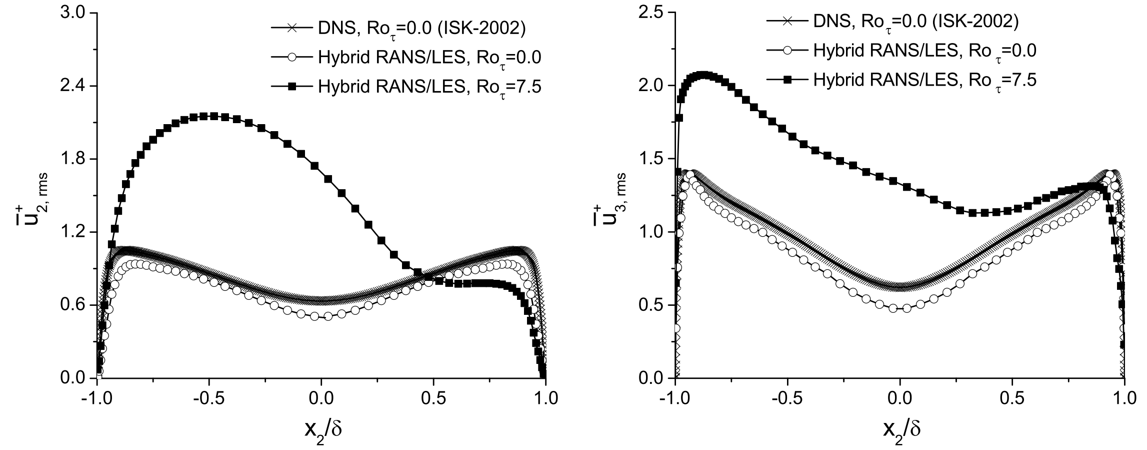

(b) RMS of the wall-normal velocity

(c) RMS of the spanwise velocity

FIGURE 4.9: Resolved RMS velocities obtained at $Ro_\tau = 0$ and 7.5 (non-dimensionalized using u_τ).

(e.g., resolved mean velocity) in a rotating flow. The effects of the Coriolis force on the second-order flow statistics (e.g., resolved turbulent stresses and TKE) in the context of LES can be studied through their transport equations, which have been derived and documented in Xun *et al.* [61]. As revealed in the experimental study of Johnston *et al.* [69] and DNS study of Kristoffersen and Andersson [20], the combined production rates (i.e., $P_{ij} + G_{ij}$) in the transport equations of the resolved turbulent stresses $-\langle \bar{u}_i'' \bar{u}_j'' \rangle$ have a significant influence on the absolute value and distribution of the resolved turbulent shear stresses and TKE. Herein, P_{ij} represents the production term arising from the mean resolved turbulent (shear and wall-normal) stresses, and

TABLE 4.2: Production terms due to the mean turbulent shear stresses (P_{ij}) and rotational stresses (G_{ij}) for a fully-developed plane channel flow subjected to spanwise system rotations.

ij	11	22	33	12
P_{ij}	$-2\langle\bar{u}_1''\bar{u}_2''\rangle(d\langle\bar{u}_1\rangle/dx_2)$	0	0	$\langle\bar{u}_2''^2\rangle(d\langle\bar{u}_1\rangle/dx_2)$
G_{ij}	$4\Omega\langle\bar{u}_1''\bar{u}_2''\rangle$	$-4\Omega\langle\bar{u}_1''\bar{u}_2''\rangle$	0	$2\Omega(\langle\bar{u}_1''^2\rangle-\langle\bar{u}_2''^2\rangle)$

G_{ij} represents the rotational stress production term that arises from the presence of Coriolis accelerations in a rotating channel flow. These production terms are written in component forms in Table 4.2. For instance, the production of the resolved shear stress component $-\langle\bar{u}_1''\bar{u}_2''\rangle$ in a fully-developed rotating channel flow is given by $P_{12}=\langle\bar{u}_2''^2\rangle(d\langle\bar{u}_1\rangle/dx_2)$ and $G_{12}=2\Omega(\langle\bar{u}_1''^2\rangle-\langle\bar{u}_2''^2\rangle)$; and that of the wall-normal stress component $\langle\bar{u}_2''\bar{u}_2''\rangle$ is given by $P_{22}=0$ and $G_{22}=-4\Omega\langle\bar{u}_1''\bar{u}_2''\rangle$.

The nearly constant level of $\bar{u}^+_{1,\mathrm{rms}}$ for $Ro_\tau=7.5$ observed in Fig. 4.9(a) within the neutral stability zone can be clearly explained using the production terms for the streamwise component $\langle\bar{u}_1''^2\rangle$ of the turbulent normal stresses. Given the definition parameter s, it is straightforward to show that $s=P_{11}/G_{11}$. Because $s=-1$ in the neutral stability zone, the combined productions vanish for $\langle\bar{u}_1''^2\rangle$ (i.e., $P_{11}+G_{11}=(1+s)P_{11}=0$). As shown in Fig. 4.7, for $Re_\tau=650$ and $Ro_\tau=7.5$, the thickness of the neutral stability zone approaches half channel height δ, as a consequence, the streamwise component of the turbulent normal stress in Fig. 4.9(a) remains at a constant level in a region with an extent about 50% of the channel height.

Figure 3.14 compares the production terms P_{ij} and G_{ij} for the resolved wall-normal turbulent stress and resolved turbulent shear stress for different rotation numbers. The values of P_{ij} and G_{ij} in Fig. 3.14 are non-dimensionalized using a constant wall dissipation rate defined as $\varepsilon_{wall}\overset{\mathrm{def}}{=}u_\tau^4/\nu\approx 2\nu[\langle\bar{S}_{ij}\rangle\langle\bar{S}_{ij}\rangle]_{wall}$ (see Wang *et al.* [51] for the near-wall approximation of $\langle\bar{S}_{ij}\rangle$). Because $P_{22}=0$, there is no direct production of $\langle\bar{u}_2''^2\rangle$ from the resolved turbulent stresses. Therefore, the effects of rotation on the value and distribution of the resolved wall-normal stress $\langle \bar{u}_2''^2 \rangle$ purely rely on G_{22}. As shown in Fig. 3.14(a), the magnitude of G_{22} is very sensitive to the rotation number, and increases monotonically with it. Besides the influence of G_{22}, energy redistributes within the system and affects the value of $\langle \bar{u}_2''^2 \rangle$ through the mechanisms of molecular diffusion, SGS production and diffusion, and pressure-strain interactions [61]. In order to clearly demonstrate the rotation effects on P_{12} and G_{12} in the near-wall region, Figs. 3.14(b)–(d) are partially enlarged. As shown in Figs. 3.14(b)–(d), both P_{12} and G_{12} are sensitive to the system rotation. Since the value and distribution of the resolved shear stress $-\langle \bar{u}_1'' \bar{u}_2'' \rangle$ is altered by $P_{12} + G_{12}$, the profile of this combined rate is shown in Fig. 3.14(d). As shown in Fig. 3.14(c), for a non-rotating case ($Ro_\tau = 0$), P_{12} assumes a sign that is opposite to that of x_2. However, due to the asymmetry of the resolved streamwise velocity profile in the wall-normal direction (see Figs. 4.5 and 4.6), it is not the case for a rotating channel flow. Furthermore, the magnitude of the production rate on the pressure side is significantly larger than that on the suction side for rotating cases.

Near the suction wall (located at $x_2/\delta = 1$) of the channel, the direct effects of system rotation are expected to reduce $\langle \bar{u}_2''^2 \rangle$ (or $\bar{u}_{2,rms}$) because $G_{22} < 0$ and the magnitude of G_{22} increases with Ro_τ (shown in Fig. 3.14(a)). As seen in Fig. 4.11, the value of $\bar{u}_{2,rms}$ is indeed damped in the region close to the suction wall. Near the suction wall, $-\langle \bar{u}_1'' \bar{u}_2'' \rangle < 0$, and the two production terms $G_{12} > 0$ and $P_{12} < 0$ (because $P_{12}{=}\langle \bar{u}_2''^2 \rangle (d\langle \bar{u}_1 \rangle / dx_2)$ and $d\langle \bar{u}_1 \rangle / dx_2 < 0$, see Figs. 4.5 and 4.6). As is clear from Fig. 4.11, near the suction side, the value of $\langle \bar{u}_2''^2 \rangle$ decreases monotonically as the rotation number increases. Therefore, it is expected that both values of $G_{12}{=}2\Omega(\langle \bar{u}_1''^2 \rangle - \langle \bar{u}_2''^2 \rangle)$ and $P_{12}{=}\langle \bar{u}_2''^2 \rangle (d\langle \bar{u}_1 \rangle / dx_2)$ increase as Ro_τ increases. These trends of G_{12} and P_{12} near the suction side of the channel are evident in Figs. 3.14(b) and (c), respectively. Consequently, as shown in Fig. 3.14(d), the level of the total production rate $P_{12} + G_{12}$ for the turbulent shear stress $-\langle \bar{u}_1'' \bar{u}_2'' \rangle$ increases as the rotation number increases, which then results in an increase in the value of $-\langle \bar{u}_1'' \bar{u}_2'' \rangle$ (correspondingly, a reduction in its magnitude $| - \langle \bar{u}_1'' \bar{u}_2'' \rangle|$) on the suction side. This physical feature that the magnitude of $-\langle \bar{u}_1'' \bar{u}_2'' \rangle$ is damped by the imposed system

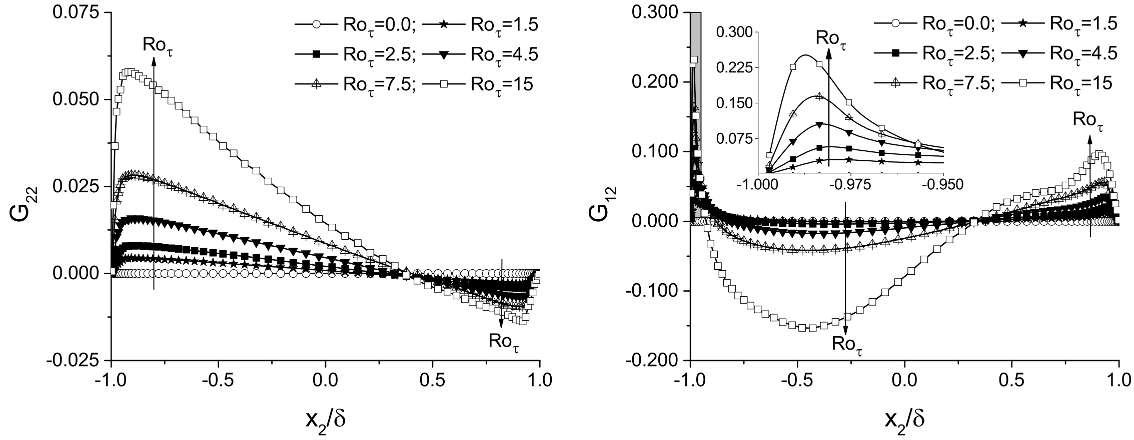

(a) G_{22} (b) G_{12}

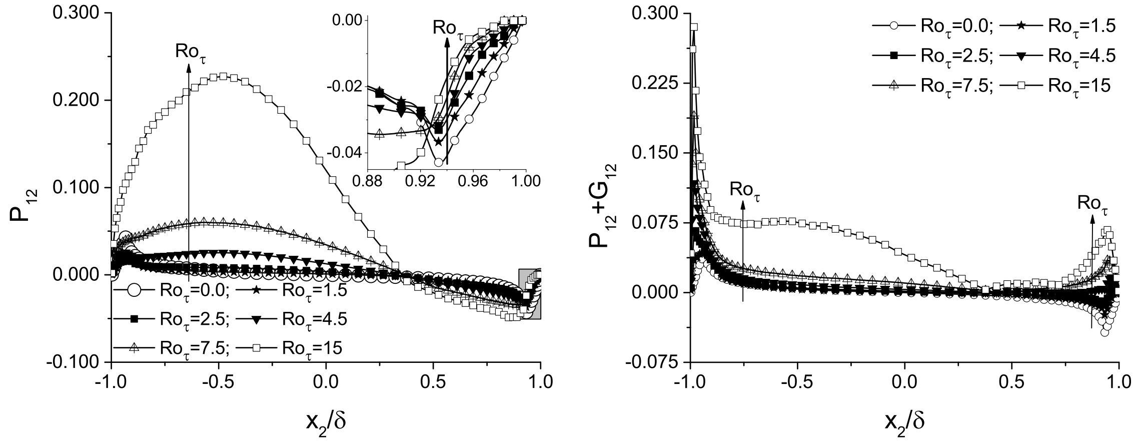

(c) P_{12} (d) P_{12}+G_{12}

FIGURE 4.10: Production rates for the resolved wall-normal turbulent stress and resolved turbulent shear stress obtained at different rotation numbers (non-dimensionalized using u_τ^4/ν). In order to demonstrate the near-wall effects, the framed areas in (b) and (c) are partially enlarged.

rotation in the flow region near the suction wall is evident in Fig. 4.12.

As shown in Figs. 4.6 and 4.12, on the pressure side of the channel, both the mean streamwise velocity gradient $d\langle\bar{u}_1\rangle/dx_2$ and resolved turbulent shear stress $-\langle\bar{u}_1''\bar{u}_2''\rangle$ are positively valued. The rotational stress production terms $G_{22}= - 4\Omega\langle\bar{u}_1''\bar{u}_2''\rangle > 0$ and $G_{12} > 0$ (see Fig. 3.14(c)), which tend to increase the levels of $\langle\bar{u}_2''^2\rangle$ and $-\langle\bar{u}_1''\bar{u}_2''\rangle$. Furthermore, because $P_{22}+G_{22} = G_{22} \propto \Omega > 0$, it is anticipated that the level of $\langle\bar{u}_2''^2\rangle$ (or, $\bar{u}_{2,rms}$) increases monotonically with Ro_τ on the pressure side. The distributions of the resolved turbulent stresses shown in Figs. 4.11 and 4.12 are in agreement with

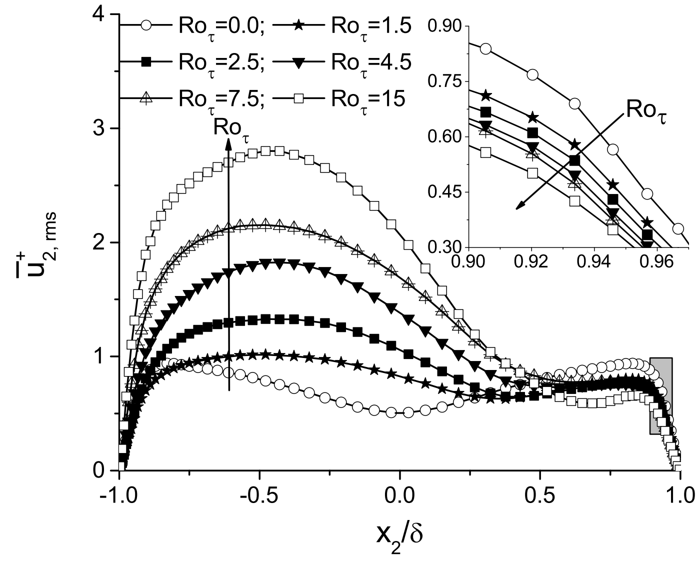

FIGURE 4.11: Resolved wall-normal component of RMS velocities obtained at different rotation numbers (non-dimensionalized using u_τ). In order to demonstrate the near-wall effects, the framed area is partially enlarged.

these expectations, and are consistent with the DNS results of Kristoffersen and Andersson [20]. However, it should be stressed that because of the modelling effects, the resolved turbulent shear stresses (i.e., $-\langle \bar{u}_1'' \bar{u}_2'' \rangle$) obtained in a hybrid approach is conceptually different from the 'exact' (or 'total') Reynolds shear stress (denoted using $-\langle u_1'^e u_2'^e \rangle$) in a DNS approach. In the following subsection, the budget of turbulent shear stresses and associated eddy viscosity profiles will be investigated.

4.3.5 Budget of Shear Stresses

In order to further study the predictive performance of the hybrid approach in terms of the momentum balance in the LES zone, the budget of shear stresses across the rotating channel needs to be examined. By applying the same procedure to obtain Eq. (3.13), an equation that expresses the balance of shear stresses at an arbitrary wall-normal location x_2 is obtained herein for the rotating channel flow, viz.

$$\nu \frac{\partial \langle \bar{u}_1 \rangle}{\partial x_2} - \langle \bar{u}_1'' \bar{u}_2'' \rangle + \nu_t \frac{\partial \langle \bar{u}_1 \rangle}{\partial x_2} = \frac{1}{\rho} \frac{\partial \langle \bar{p} \rangle}{\partial x_1} x_2 + \frac{\tau_{wp}}{\rho} \quad . \tag{4.6}$$

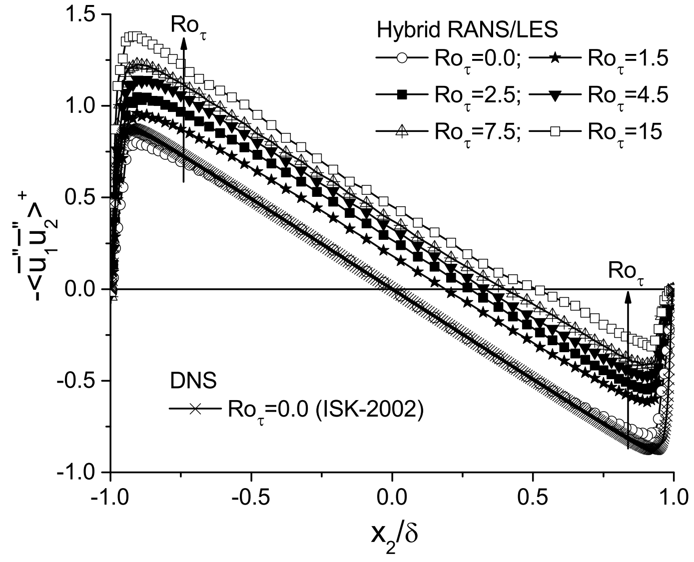

FIGURE 4.12: Resolved turbulent shear stress obtained at different rotation numbers (non-dimensionalized using u_τ^2).

Note that the Coriolis force term vanishes after the time- and plane-averaging is applied to the filtered streamwise momentum equation (i.e., Eq. (2.5)). The three terms on the LHS of Eq. (4.6) represent the resolved viscous shear stress, resolved turbulent shear stress, and modelled shear stress, respectively. The two terms on the RHS of the equation correspond to the resolved integrated shear force due to the mean pressure gradient, and the resolved viscous shear stress at the pressure wall, respectively.

Figure 4.13 shows the shear stress budget predicted using hybrid RANS/LES with the dynamic forcing scheme for the rotating channel flow at $Ro_\tau = 7.5$. All quantities presented in the figure have been non-dimensionalized using u_τ^2. In order to clearly demonstrate the near-wall effects on the shear stress budget under investigation, Fig. 4.13 is partially enlarged using sub-panels. It can be clearly seen from the figure that the total shear stress calculated from the LHS of Eq. (4.6) agrees very well with that calculated from the RHS of Eq. (4.6), implying that shear stress balance predicted by hybrid RANS/LES is well satisfied across the entire rotating channel. As expected, it is observed from Fig. 4.13 that the resolved viscous shear stress dominates in the viscous sublayer, while the resolved turbulent shear stress dominates the fully

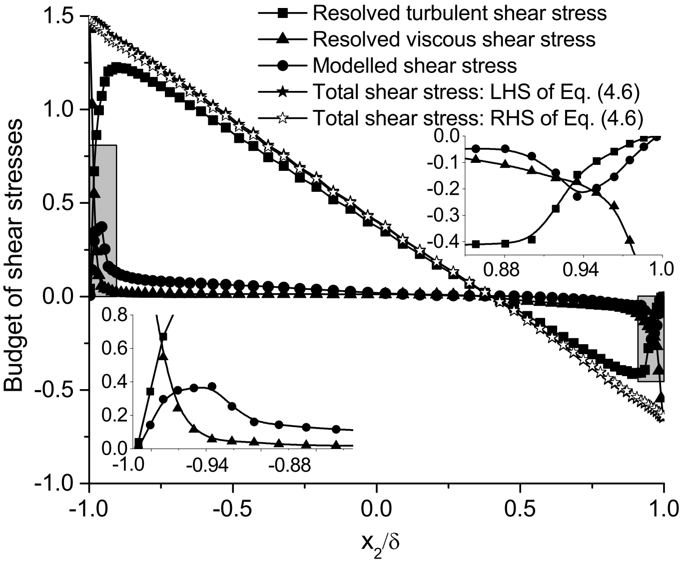

FIGURE 4.13: Budget of shear stresses obtained at $Ro_\tau = 7.5$ (non-dimensionalized using u_τ^2). In order to demonstrate the near-wall effects, the framed areas are partially enlarged.

turbulent layer away from the wall. As shown in Fig. 4.13, the modelled shear stress component peaks at the interface ($x_2/\delta = \pm 0.94$, or $x_2^+ = 39$). This feature is expected, because at the interface, the model switches from RANS to LES.

The effect of system rotation on the shear stress budget can be clearly seen by comparing Fig. 4.13 with Fig. 3.19 (which is identically corresponding to the non-rotating channel flow case ($Ro_\tau = 0$)). As shown previously in Fig. 3.19, for the non-rotating case, the profile of each component shear stress (corresponding to each term on the LHS of Eq. (3.13)) features an anti-symmetrical pattern about channel center (located at $x_2/\delta = 0$). However, as clearly shown in Fig. 4.13, this physical feature no longer holds when rotation is imposed. Furthermore, as shown in Fig. 3.19, for the non-rotating case, it is observed that as the distance from the wall increases, the time- and plane-averaged modelled turbulent shear stress component (i.e., $\nu_t \partial\langle\bar{u}_1\rangle/\partial x_2$) becomes greater than that of the viscous shear stress component. As shown in Fig. 4.13, for the rotating case, it is observed that the level of modelled turbulent shear stress surpasses that of viscous shear stress near the pressure side, however, this is not the case near the suction side. This is because turbulence is suppressed on the suction side of the channel by the Coriolis force in a rotating channel flow.

Figure 4.14 demonstrates the Reynolds shear stress decomposition predicted using hybrid RANS/LES at $Ro_\tau = 7.5$. The total (Reynolds) shear stress and the two shear stress components (namely, the resolved turbulent shear stress and the modelled turbulent shear stress) are shown in the figure. In order to clearly demonstrate the stress profiles in the near-wall region, the curves presented in Fig. 4.14 are partially enlarged using sub-panels. As is expected in a hybrid approach, the modelled turbulent shear stress component contributes significantly to the total Reynolds shear stress in the RANS zone, whereas the resolved component dominates in the LES zone. This feature is well captured in Fig. 4.14 using the dynamic forcing scheme for the rotating channel flow. The effect of system rotation on the level of Reynolds shear stress is obvious by comparing Fig. 4.14 with Fig. 3.17 (which is identically corresponding to the non-rotating channel flow case ($Ro_\tau = 0$)). As is clear from Fig. 3.17, for the non-rotating channel flow case, the profiles are anti-symmetrical about the channel center (located at $x_2/\delta = 0$) across the channel. However, as show in Fig. 4.14, it is clear that this property of anti-symmetry is broken due to the imposed system rotation. At $Ro_\tau = 7.5$, both the total and resolved Reynolds shear stresses become much higher on the pressure side ($x_2/\delta = -1$) where turbulence is enhanced than on the suction side ($x_2/\delta = -1$) where turbulence is suppressed. In the following context, the modelled turbulent shear stress in the RANS and LES zones will be further analyzed by investigating the wall-normal profile of the eddy viscosity ν_t.

Figure 4.15 compares the profiles of the eddy viscosity obtained at $Ro_\tau = 0$ and 7.5. These profiles are non-dimensionalized using the kinematic viscosity ν. By comparing Fig. 4.15 with Fig. 4.14, it is clear that the wall-normal profile of the mean eddy viscosity is closely correlated with the modelled shear stresses. In the viscous sublayer, $\nu_t/\nu \ll 1$ strictly holds for both non-rotating and rotating cases, implying that the level of modelled turbulent shear stress is significantly lower than that of the viscous shear stress. For both rotating and non-rotating cases, $\nu_t|_{wall} \equiv 0$ holds, and as the distance from the wall increases, ν_t increases (defined in Eq. (2.10)) and peaks at the interface (located at $x_2/\delta = \pm 0.94$), which is consistent with the previous

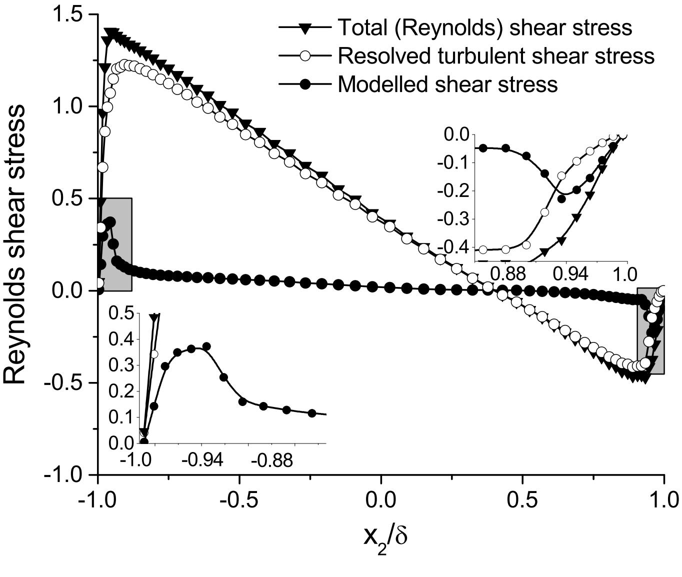

FIGURE 4.14: Reynolds shear stress decomposition for the rotating channel flow (non-dimensionalized using u_τ^2). In order to demonstrate the near-wall effects, the framed areas are partially enlarged.

observation that the modelled turbulent shear stress also peaks at the interface in Figs. 4.13 and 4.14. The mechanism underlying these peaks relates to the backscatter of KE produced by the dynamic forcing scheme. As shown previously in Fig. 3.9, the backscatter of KE from small to large scale motions reaches the maximum at the interface, which significantly enhances the turbulence level at the boundary of the LES region (for transient simulation of turbulence). As a consequence, the level of the eddy viscosity (and modelled turbulent shear stress) increases drastically at the interface in Fig. 4.15 to reflect this mechanism. An enhanced level of modelled turbulence at the interface as exhibited in Figs. 4.14 and 4.15 is the key to the success of forcing modelling for properly running LES in a hybrid approach.

The influence of rotation on the eddy viscosity is evident in Fig. 4.15. The profile of ν_t is symmetrical for the non-rotating case but asymmetrical for the rotating case (in response to the Coriolis force). For the rotating case ($Ro_\tau = 7.5$), although the peak of ν_t still occurs at the interface ($x_2/\delta = \pm 0.94$) between RANS and LES regions, the peak value is larger on the pressure side than that on the suction side. Furthermore, in the LES zone above the interface, $\nu_t/\nu > 1$ holds near the pressure side within the range $-0.94 < x_2/\delta < -0.5$, whereas $\nu_t/\nu < 1$ holds near the suction

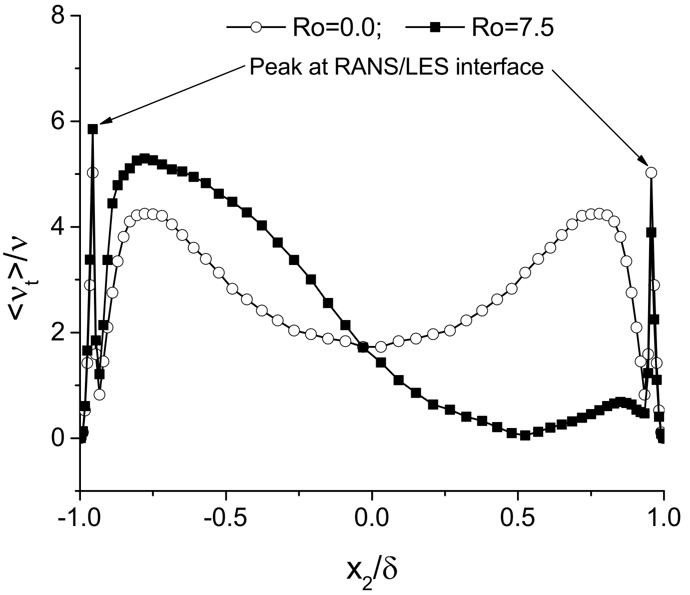

FIGURE 4.15: Comparison of the time- and plane-averaged wall-normal profiles of the non-dimensional eddy viscosity for non-rotating ($Ro_\tau = 0$) and rotating ($Ro_\tau = 7.5$) channel flow cases.

side within the range $0.5 < x_2/\delta < 0.94$. This indicates that in the LES zone, the level of modelled turbulent shear stress is larger near the pressure side but smaller near the suction side in comparison with that of the viscous shear stress (see also Fig. 4.13), further confirming that the turbulence level is enhanced and suppressed on these two sides, respectively.

4.3.6 Characteristics of the Dynamic Forcing

Figure 4.16 shows the time- and plane-averaged profiles of $\langle P_r^B \rangle$ for the rotating channel flow at $Ro_\tau = 7.5$. The value of $\langle P_r^B \rangle$ has been non-dimensionalized using a constant wall dissipation rate ε_{wall}. As shown in the figure, the time- and plane-averaged value of $\langle P_r^B \rangle$ maintains negative across the channel, indicating that the net effect of dynamic forcing is to produce backscatter of KE, which is needed in a successful hybrid RANS/LES simulation. The effect of system rotation on the wall-normal profile of $\langle P_r^B \rangle$ is clear by comparing Fig. 4.16 with Fig. 3.9(c). As the rotation number increases from $Ro_\tau = 0$ to 7.5, the profile of $\langle P_r^B \rangle$ becomes asymmetrical in the wall-normal direction under the influence of the Coriolis force.

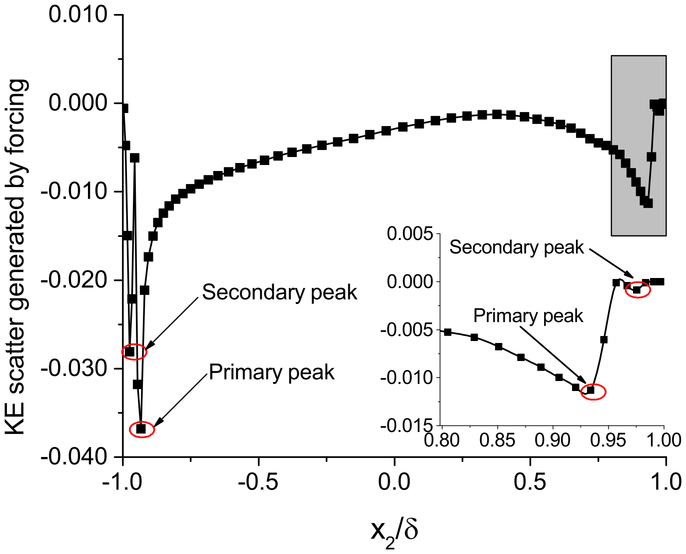

FIGURE 4.16: Backscatter of KE produced by the dynamic forcing exhibited using profiles of the time- and plane-averaged KE production rate $\langle P_r^B \rangle$ for the rotating ($Ro_\tau = 7.5$) channel flow case (non-dimensionalized using u_τ^4/ν). In order to demonstrate the near-wall effects, the framed area is partially enlarged.

In order to clearly show the $\langle P_r^B \rangle$ profile on the suction side of the rotating channel, Fig. 4.16 is partially enlarged in the near-wall region. As shown in Fig. 4.16, at $Ro_\tau = 7.5$, although the dual peak pattern of the backscatter produced by forcing is preserved, the strength of the backscatter is significantly enhanced on the pressure side. The magnitudes of the primary and secondary peaks of $\langle P_r^B \rangle$ on the pressure side at $Ro_\tau = 7.5$ are twice and eight times greater than those for the non-rotating channel case (at $Ro_\tau = 0$), respectively. This physical feature is expected, because the turbulence level is enhanced on the pressure side and suppressed on the suction side by the Coriolis force. Due to its self-calibrating mechanism, the dynamic foring is able to reflect this anisotropic effect of the Coriolis force in the wall-normal direction.

Chapter 5

Hybrid RANS/LES of Turbulent Flow in a Spanwise Rotating Rib-Roughened Channel

In this chapter, the predictive performance of the dynamic forcing scheme is further evaluated in the context of rib-roughened channel flows with and without system rotations. The rib-roughened channel is subjected to either clockwise or counter-clockwise system rotation. The combined effects of surface roughness and the Coriolis force on the flow field are investigated. The flow is characterized by a Reynolds number of $Re = 1.5 \times 10^4$ and a rotation number Ro ranging from -0.6 to 0.6. In order to validate the hybrid approach, turbulence statistics obtained from the simulations are thoroughly compared with the available laboratory measurement data recently acquired by Coletti *et al.* [41–43].

5.1 Problem Description

Rotating turbulent flow over a rib-roughened surface represents an interesting topic in flow physics and has important engineering applications in devices such as the internal blade cooling system of gas turbines and rotating heat exchangers. In these devices, the surface of the flow passage is typically roughened by the arranged elements such as transverse ribs and protuberances. In response to the unsteady vortices triggered by apparent roughness elements, near-wall turbulent mixing and heat transfer are often significantly enhanced. Furthermore, as the Coriolis force arises from the system rotation, flow structures in the rotating channel are dramatically altered due to the induced strong secondary flows in the cross-stream directions. As a consequence, the physical mechanisms underlying the combined effects of surface roughness and Coriolis force are subject to further dynamical complexities, which impose additional challenges on turbulence models for precise prediction of the flow field in a rotating rib-roughened channel.

5.1.1 Turbulent Flows over a Rib-Roughened Wall

In comparison with a smooth-wall turbulent boundary layer, vigorous separation and reattachment occur in turbulent flows over an obstacle-roughened wall. Roughness effects exist in a broad class of obstacle-induced separating/reattaching flows and boundary layers, varying from the flow over a single obstacle to that over an array of obstacles of different shapes. Among them, turbulent flows over a row of transverse ribs have been extensively investigated using both laboratory measurements [41, 85] and numerical simulations [86–90]. In such flows, ribs are typically aligned in the spanwise direction to form the so-called 'transverse-rib roughnesses'. Agelinchaab and Tachie [85] studied the effects of the cross-sectional shape of the obstacle on the size of the recirculation bubble and shear layer interactions. In their study, measurements were conducted using PIV on the turbulent flow over obstacles of square, rectangular and semicircular cross-sections. They observed that the size of the separation bubble obtained for a square rib is larger than that for rectangular and semicircular ribs under similar test conditions. As a result, the interaction between different shear layers is the most intense downstream of a square-shaped rib.

A rib-roughened flow is significantly influenced by the pitch ratio (i.e., L_p/h, where h represents the rib side length and L_p denotes the pitch between two adjacent ribs, see Fig. 5.1). In a turbulent flow over transverse ribs, different types of roughnesses can be achieved by varying the pitch ratio. Following Perry *et al.* [91], surface roughnesses can be classified as d-type, intermediate, and k-type. If $L_p/h < 4$, d-type roughness is obtained; if $L_p/h = 4$, the surface condition is often referred to as intermediate roughness; and if $L_p/h > 4$, the surface condition corresponds to k-type roughness. In d-type and intermediate roughness regimes, large stable vortices fill up and recirculate within the semi-open cavity between ribs, which prevents the outer flow from reattaching the floor of the cavity. In contrast, for k-type roughness, vortices occupy only a fraction of the cavity and the separated flow reattaches the floor. In the presence of k-type roughness, a free shear layer is triggered at the upstream edge of the rib, which then develops immediately above the rib and extends to the inter-rib region. Subsequently, the free shear layer interacts with both the outer flow and the wall shear layer redeveloped along the floor after the reattachment point, creating strong unsteady vortices and enhancing the near-wall turbulence mixing. Panigrahi and Acharya [92] concluded that the unsteady large-scale structures in the rib-roughened channel are associated with events of sweeps, ejections, and inward and outward interactions with the recirculation bubble. These events play an important role in the production and transport of turbulent shear stresses. Recently, based on their experimental study of rib-roughened flows, Coletti *et al.* [41] observed that the flapping of the free shear layer, which starts at the downstream edge of the obstacle, can result in oscillations in the position of the instantaneous reattachment point on the floor of the inter-rib region. Liu *et al.* [93] studied the oscillation zone for the instantaneous reattachment point by using a microphone array and a split-fiber film to measure the correlation between velocity and wall-pressure fluctuations behind the rib. They observed that the oscillation zone has a streamwise length of $1.2h$. Besides the pitch ratio, a rib-roughened flow is also influenced significantly by the blockage ratio (i.e., h/H, where H is the channel height). The blockage ratio h/H is a sensitive parameter in a ribbed heat exchanger, as it influences both heat transfer coefficient and hydraulic losses. Because the pressure drop rises as the rib height increases, the optimum blockage ratio is often set within the range $0.05 \leq h/H \leq 0.1$ in order to compromise the drag force and the thermal efficiency [94, 95].

5.1.2 Rotation Effects on Rib-Roughened Channel Flows

Recently, Coletti *et al.* [42, 43] performed detailed PIV measurements to study the effects of Coriolis and centrifugal forces on rib-roughened channel flows subjected to spanwise system rotations. In their experiments, transverse ribs were mounted on one of the duct walls, and turbulence statistics were obtained up to $3.5h$ along the wall-normal direction in order to cover the whole free shear layer over the rib. The PIV measurements of Coletti *et al.* [42, 43] were carefully performed with the imaging system mounted on the rotating test rig such that the relative flow velocity can be directly obtained. As indicated by Di Sante *et al.* [76], this can result in better temporal and spatial resolutions and can eliminate large uncertainties in measurements especially at a high angular velocity.

5.1.3 Numerical Studies on Rib-Roughened Channel Flows

Over the past decade, different numerical approaches have also been used to study the effects of surface roughness and rotation on rib-roughened turbulent flows. Owing to its important application in heat exchanger industry, in current literature, most of DNS and LES studies have focused on square-shaped ribs and the effects of the pitch ratio L_p/h on the flow field, while keeping the blockage ratio fixed within $0.05 \leq h/H \leq 0.1$. In the DNS study carried out by Leonardi *et al.* [87, 88], flow recirculation occurs immediately downstream of each rib for $L_p/h \geq 8$. Based on the mean streamline patterns and streamwise distribution of the local skin friction coefficient, they observed that each periodical element (consisting of one rib and one pitch) is virtually independent. They concluded that the rib-to-rib interactions are negligible if the ribs are arranged with a sufficiently large spacing between them. Fransen *et al.* [96] carried out LES of the rotating rib-roughened channel flows to study the effects of the Coriolis force. Their simulation results compared favourably with the PIV measurements of Coletti *et al.* [42] when the ribbed wall was exposed to the stabilizing rotation; however, substantial differences were observed when the ribbed wall was subjected to the destabilizing rotation. In the LES study of Fransen *et al.* [96], the flow conditions were kept the same as the experiment of Coletti *et al.* [42] with only one of the walls roughened by transverse ribs while the other wall kept smooth. In contrast, in the DNS study of Narasimhamurthy and Andersson [97], both channel walls were roughened. Based on their DNS results, Narasimhamurthy and Andersson [97] concluded that the combined influences of rib-roughness and system rotation on the turbulent flow field cannot be foreseen by straightforward superposition of these two factors. Furthermore, they observed that the flow field in the vicinity of a ribbed wall is insensitive to the condition whether the other wall is smooth or ribbed. In the core region of the channel, however, both walls have direct impacts on the flow field. Therefore, the flow field in a two-sided roughness channel is different from that in a one-sided roughness channel [97].

As an effective tool for numerical simulations, the hybrid approach has also been employed for computing rib-roughened channel flows. Tucker and Davidson [12] and Liu *et al.* [98] utilized the one-equation k-ℓ model in both RANS and LES regions for their hybrid simulation of turbulent flows in a non-rotating rib-roughened channel. According to their tests, the hybrid RANS/LES approach has yielded satisfactory predictions of the separation and reattachment phenomena in the flow. Kubacki *et al.* [99] utilized a two-equation k-ω model of Wilcox [1] in their hybrid simulation of turbulent flows in a rotating rib-roughened channel, and validated their simulation results against the experimental data of Coletti *et al.* [42].

In this chapter, the research scope is extended by considering a simplified dynamic forcing scheme for hybrid RANS/LES. The predictive performance of the forcing scheme is examined in the context of a rotating rib-roughened channel flow, in which both of the roughness and Coriolis force play significant roles in the characteristics of the flow field. To validate the proposed hybrid RANS/LES approach, the numerical results obtained are thoroughly validated against the recent PIV measurement data of Coletti *et al.* [41–43].

5.2 Numerical Aspects

Figure 5.1 shows the computational domain of the rotating rib-roughened channel and associated coordinate system. As shown in the figure, the system rotates in the spanwise direction with an angular velocity Ω, which can be either a positive constant (corresponding to counter-clockwise rotation), or a negative constant (corresponding to clockwise rotation). Components of the Coriolis force arising from counter-clockwise rotation and clockwise rotation are demonstrated in Figs. 5.1(a) and (b), respectively. The dimensions of the computational domain are $L_1 \times L_2 \times L_3 = 20h \times 10h \times 9h$ in the streamwise (x_1), wall-normal (x_2) and spanwise (x_3) directions, respectively. The bottom wall located at $x_2/h = 0$ is mounted with transverse ribs, and the upper wall located at $x_2/h = 10$ is kept smooth. The computational domain covers two periods formed by three ribs. Each rib has a square cross-section of $h \times h$. The pitch ratio is set to $L_p/h = 10$ so that the surface condition represents k-type roughness for the stationary rib-roughened channel flow case. The blockage ratio is set to $h/H = 0.1$ (where $H = L_2$ is the channel height). The geometry of the rib, pitch ratio and blockage ratio are identical to those in the PIV measurements of Coletti *et al.* [41–43]. It is worthwhile to note that the imaging system in the experiments of Coletti *et al.* [41–43] was very carefully set up, which rotated with the test section. As such, they were able to measure the relative velocities with respect to the rotating frame with the same resolution and accuracy as in a stationary test rig. Furthermore, their PIV measurements were conducted in the fully-developed region where flow statistics have attained periodicity from the upstream rib to the subsequent. In order to reproduce the experiments of Coletti *et al.* [41–43], the computational domain is also assumed to be periodical in current numerical simulations.

In accordance with the PIV experiments of Coletti *et al.* [41–43], the flow is characterized by a Reynolds number of $Re \overset{\text{def}}{=} U_b H/\nu = 1.5 \times 10^4$, and the rotation numbers ($Ro \overset{\text{def}}{=} \Omega H/U_b$) were set to 0, ± 0.3, and ± 0.38. Here, U_b denotes the bulk mean velocity. A positively valued Ro corresponds to a counter-clockwise rotation, whereas a negatively valued Ro corresponds to a clockwise rotation. As indicated by

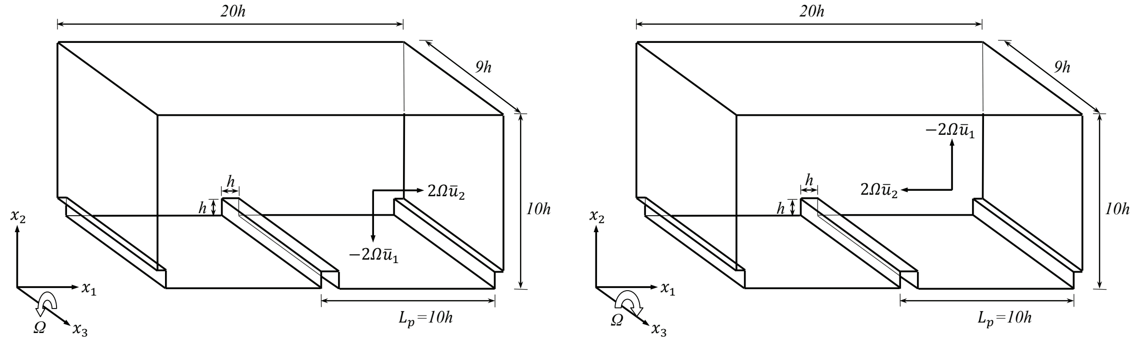

(a) counter-clockwise rotation (b) clockwise rotation

FIGURE 5.1: Computational domain for hybrid RANS/LES of turbulent flow in a rib-roughened channel subjected to a spanwise rotation. The origin of x_1-coordinates starts from the leeward face of the first rib. Under counter-clockwise rotation, the pressure (destabilizing) side is located near the rib-roughened wall (at $x_2/h = 0$); however, under clockwise rotation, the pressure (destabilizing) side is located near the smooth wall (at $x_2/h = 10$).

Coletti *et al.* [42], their selection of these Reynolds number and rotation numbers is typical of internal cooling channel flows in turbine blades. Besides these five rotation numbers used in the experiments of Coletti *et al.* [41–43], in order to thoroughly examine the rotation effects, additional tests with a much lower rotating speed $|\Omega|$ at $Ro = \pm 0.05$ and a much higher rotating speed $|\Omega|$ at $Ro = \pm 0.6$ have also been performed using hybrid RANS/LES.

The new forcing stress tensor τ_{ij}^B proposed herein is modelled as

$$\tau_{ij}^B = -C_N \eta_{ij} \quad . \tag{5.1}$$

In comparison with the previous forcing model (represented by Eq. (2.22)) tested in chapter 3 and chapter 4, it is obvious that the new forcing scheme (represented by Eq. (5.1)) to be tested in this chapter has dropped the second quadratic base tensor γ_{ij}. The rationale behind this modification is to propose a simple and robust dynamic forcing model for performing hybrid RANS/LES. It is based on the consideration that according to previous full LES studies [49–51], the γ_{ij} term does not contribute to the backscatter of KE from the subgrid to the resolved scales, and it is the η_{ij} term that contributes significantly to the backscatter.

Similarly, with the forcing stress tensor at the test-grid level modelled as $T_{ij}^B = -C_N \zeta_{ij}$, the values of the coefficient C_N in Eq. (5.1) can be obtained by minimizing the residual of the Germano identity following the conventional dynamic procedure, viz.

$$C_N = -\frac{N_{ij}\mathcal{L}_{ij}}{N_{ij}N_{ij}} \quad . \tag{5.2}$$

In this chapter, the proposed hybrid approach is evaluated based on the combination of algebraic closure models (i.e., the mixing length model for RANS region and the DSM of Lilly [47] for LES region) and the dynamic forcing scheme represented by Eq. (5.1). When hybrid RANS/LES is applied to simulation of separating/reattaching flows, the interface location that separates the RANS and LES zones can be explicitly specified using a given wall-normal distance [10–12, 98], or dynamically determined according to flow properties (such as TKE in Breuer *et al.* [100], or volumetric flow rate in Davidson and Dahlström [24]). As summarized in the comprehensive review of Fröhlich and von Terzi [8], both approaches are practical and effective in defining the interface location, and both are capable of capturing complex unsteady flow features associated with flow separation and reattachment. Following the approach of Tucker and Davidson [12], the interface location that separates the RANS zone and LES zone in the studies herein is explicitly specified at $x_2/h = 0.2$ near the lower ribbed wall, and at $x_2/h = 9.8$ near the smooth wall. Based on previous studies in chapter 3, the forcing region is indeed not a sensitive factor in a hybrid method, as long as the forcing is in use. This conclusion is consistent with previous observations of Larsson *et al.* [14] and Nikitin *et al.* [15]. In view of this, the proposed dynamic forcing scheme in Eq. (5.1) is applied to the entire computational domain.

In total, $160 \times 80 \times 80$ control volumes were used (in the streamwise, wall-normal and spanwise directions, respectively), and the number of grid points is of the same order of that employed by Tucker and Davidson [12] and Liu *et al.* [98] in their hybrid simulations of stationary rib-roughened channel flows. The grid was refined near all solid surfaces in the streamwise and wall-normal direction, and kept uniform in the spanwise direction.

No slip and impermeable boundary conditions were imposed on the velocity components at all solid surfaces. Periodic boundary conditions were employed in the streamwise and spanwise directions. Statistics of various flow variables were calculated based on 45,000 time steps (corresponding to $150h/U_b$) after the flow field became fully developed.

5.3 Results and Discussions

In this section, the numerical results on both rotating and non-rotating ribbed flows are analyzed, which include examination of the destabilizing and stabilizing rotation effects, T-G vorticies, separation and reattachment phenomena, and the first- and second-order flow statistics. In order to assess the predictive performance of the dynamic forcing scheme in the context of the rotating rib-roughened channel flow, turbulence statistics obtained from hybrid RANS/LES are compared against available laboratory measurements of Coletti *et al.* [41–43] (designated here as CMAD-2012).

5.3.1 Destabilizing and Stabilizing Rotation Effects

The Coriolis force induced by the system rotation influences the transport of momentum in the flow. The effects of the Coriolis force on the flow field can be either destabilizing or stabilizing, corresponding to either enhanced or reduced turbulence level in comparison with the non-rotating case, respectively. Under certain circumstances with sufficiently high rotating speeds, re-stabilization of the flow can occur. To further clarify these concepts related to rotating effects, the Bradshaw-Richardson number can be considered, which is defined as

$$BR = s(s+1) \quad , \tag{5.3}$$

where $s \overset{\text{def}}{=} 2\Omega/\omega_3$ and ω_3 is the spanwise vorticity given by $\omega_3 \overset{\text{def}}{=} \partial\langle\bar{u}_2\rangle/\partial x_1 - \partial\langle\bar{u}_1\rangle/\partial x_2$. Here, a pair of angular brackets $\langle\cdot\rangle$ represents time- and spanwise-averaging. According to the conventional stability criterion established by Bradshaw [72], the effect of rotation is destabilizing if $-1 < s < 0$ (corresponding to $BR < 0$), and stabilizing if $s > 0$ (corresponding to $BR > 0$), and re-stabilizing if $s < -1$ (corresponding to $BR > 0$). Under the re-stabilization condition, the turbulence level of the flow remains the same or even reduced as the rotating speed Ω increases. Furthermore, it has been recently indicated by Coletti *et al.* [42] that if the mean flow vorticity approaches the order of U_b/H, re-stabilization may occur only when $Ro > 0.5$. The measurements of Coletti *et al.* [41–43] have only been conducted up to $Ro = 0.38$. It would be of significant interest to examine the flow structures and statistics when the flow undergoes re-stabilization in response to a higher counter-clockwise rotating speed. In view of this, an additional test is performed at $Ro = 0.6$ using hybrid RANS/LES to verify the conjecture of Coletti *et al.* [42] by finding out whether re-stabilization occurs only for $Ro > 0.5$.

Figure 5.2 displays wall-normal profiles of the Bradshaw-Richardson number extracted at five streamwise locations for $x_1/h = 0$, 2, 4, 6 and 8. These profiles were obtained under three different rotating conditions: non-rotation ($Ro = 0$), clockwise rotation ($Ro = -0.38$) and counter-clockwise rotation ($Ro = 0.38$). As indicated by Coletti *et al.* [42], in the rib-roughened wall region, both the boundary layer developing along the floor downstream of the rib and the free shear layer generated by the rib are associated with a negatively valued mean spanwise vorticity ω_3. Consequently, it is expected to observe in Fig. 5.2 that in the region near the rib-roughened wall, clockwise rotation ($\Omega < 0$ at $Ro = -0.38$) results in positively valued BR, whereas counter-clockwise rotation ($\Omega > 0$ at $Ro = 0.38$) results in negatively valued BR. This implies that clockwise rotation stabilizes the region close to the rib-roughened wall, whereas counter-clockwise rotation destabilizes it (at moderate rotating speed). From Fig. 5.2, it is also observed that there are exceptions (on the sign of the BR value) in the vicinity of the floor behind the rib occurring at $x_1/h = 2$ for $Ro = 0.38$, and at $x_1/h = 2$ and 4 for $Ro = -0.38$. These exceptions were also observed by Coletti *et al.* [42] in their PIV experiments. According to the explanation of Coletti *et al.* [42], this was caused by the reverse flow behind the ribs where the mean spanwise

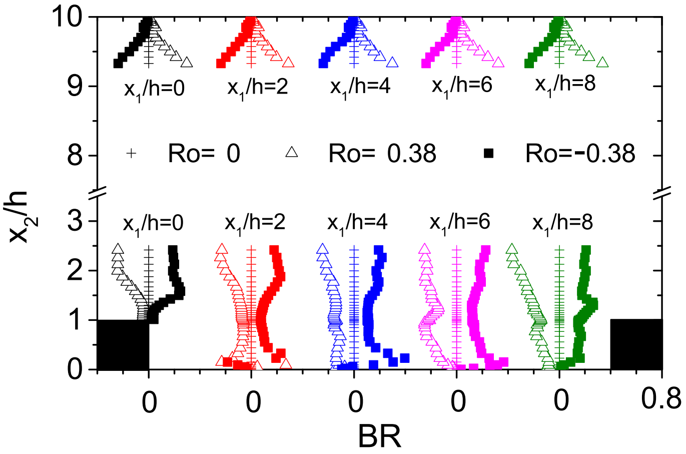

FIGURE 5.2: Profiles of Bradshaw-Richardson number BR for flow without rotation ($Ro = 0$), under counter-clockwise rotation ($Ro = 0.38$) and under clockwise rotation ($Ro = -0.38$).

vorticity changes from negative to positive values. In the region close to the smooth wall, it is clearly shown in Fig. 5.2 that the Coriolis force has a destabilizing effect for clockwise rotation (because $BR < 0$), and stabilizing effect for counter-clockwise rotation (because $BR > 0$). Differences in the profiles of the Bradshaw-Richardson number at $Ro = \pm 0.38$ exhibited in Fig. 5.2 are direct consequences of the switching of the Coriolis force direction under two opposite (counter-clockwise and clockwise) system rotations. Consequently, it is expected to observe that the level of turbulence increases near the rib-roughened wall (i.e., at $x_2/h = 0$, on the pressure side) and decreases near the smooth wall (i.e., at $x_2/h = 10$, on the suction side) under counter-clockwise rotation. In contrast, under clockwise rotation, the turbulence level is expected to be augmented near the smooth wall (i.e., at $x_2/h = 10$, on the pressure side) and reduced near the rib-roughened wall (i.e., at $x_2/h = 0$, on the suction side) in comparison with the non-rotating case ($Ro = 0$).

5.3.2 Taylor-Görtler Vortices

In the following context, time-averaged flow fields obtained under both counter-clockwise and clockwise rotations will be presented in order to demonstrate the combined effects of the Coriolis force and surface roughness on T-G vortices in a rib-roughened channel.

Figures 5.3(a) and (b) compare the time-averaged velocity fields under counter-clockwise and clockwise rotations in the central cross-stream plane of the inter-rib region (located at $x_1/h = 4.5$). In order to demonstrate the T-G vortices, contour of the wall-normal velocity $[\bar{u}_2]$ are superimposed onto the time-averaged velocity vector map. Here, a pair of square brackets $[\cdot]$ are used to indicate time-averaging. As shown in Fig. 5.3(a), for the counter-clockwise rotation case ($Ro = 0.38$), a large pair of T-G vortices occupies almost the entire plane, extending from the rib-roughened wall to vertical location around $x_2/h = 8.0$. The large-scale vortical structures shed from the rib are enlarged by the destabilizing effect of the Coriolis force near the rib-roughened wall under counter-clockwise rotation. However, as shown in Fig. 5.3(b), for the clockwise rotation case ($Ro = -0.38$), three pairs of T-G vortices are observed in the region close to the smooth wall where the destabilizing effect dominates under clockwise rotation. In sharp contrast to the counter-clockwise rotating case shown in Fig. 5.3(a), in the clockwise rotating case, fluid near the smooth wall is more turbulent due to the destabilizing effect of the Coriolis force; however, vortices triggered by the rib are suppressed close to the rib-roughened wall (especially, within $0 < x_2/h < 2.0$) due to the stabilizing effect of the Coriolis force.

5.3.3 Reattachment Length

Figure 5.4 compares time- and spanwise-averaged streamlines obtained in the (x_1-x_2)-plane of the channel at five different rotation numbers for both non-rotating and rotating rib-roughened flows. For the stationary case ($Ro = 0$), as shown in Fig. 5.4(a), due to the blockage of the rib, the flow is forced to accelerate and then expand immediately after the rib, creating a curved free shear layer that impinges onto the floor at approximately $L_R/h = 4.00$. Here, L_R represents the reattachment length. As shown in Fig. 5.4(a), such a shear layer encompasses a large recirculation zone (labeled using 'B' in the figure). The pitch ratio has a significant impact on the size of the recirculation bubble. For a small pitch ratio, the free shear layer originated

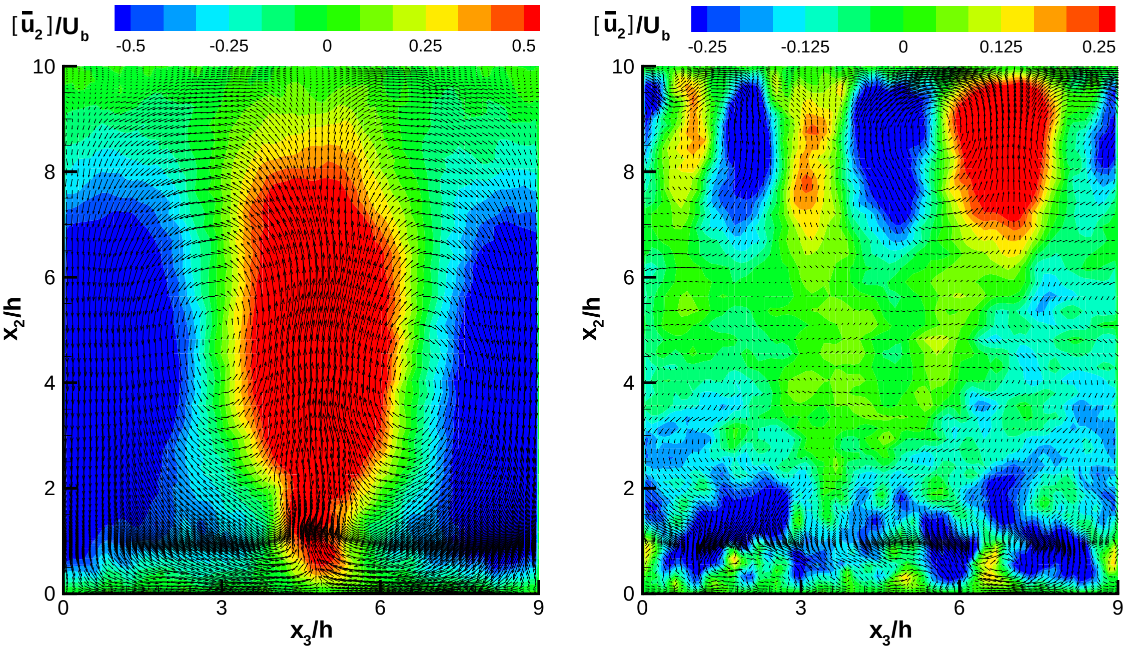

(a) $Ro = 0.38$ (b) $Ro = -0.38$

FIGURE 5.3: Taylor-Görtler vortices demonstrated in the central cross-stream plane (at $x_1/h = 4.5$) for flow under counter-clockwise rotation ($Ro = 0.38$) and under clockwise rotation ($Ro = -0.38$).

from the upstream rib extends its influence to the entire inter-rib region, facilitating a stronger rib-to-rib interaction. In contrast, for a large pitch ratio with $L_p/h \geq 8$, as demonstrated by Leonardi *et al.* [87], ribs are virtually isolated and the primary flow structures and pressure distributions are not directly altered by the upstream ribs. Because the pitch ratio in the current hybrid RANS/LES is sufficiently large (i.e., $L_p/h = 10$), the recirculation bubble B closes well before the subsequent obstacle, resulting in the so-called k-type roughness defined by Perry *et al.* [91]. Furthermore, as shown in Fig. 5.4(a), a smaller vortex (labeled using 'A') is formed at the back corner of the rib. This corner vortex A rotates in the counter-clockwise direction, which is generated as the near-wall streamlines of the reverse flow approach the leeward side of the rib and separate under an adverse pressure gradient. Downstream of the reattachment of the free shear layer, a new boundary (wall shear) layer develops, and then separates from the floor due to the blockage of the subsequent rib. This impinging effect results in a local recirculating vortex (labeled using 'C') on the windward side of the subsequent rib.

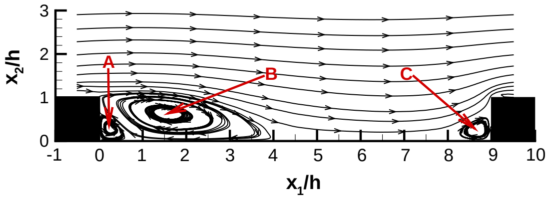

(a) $Ro = 0$

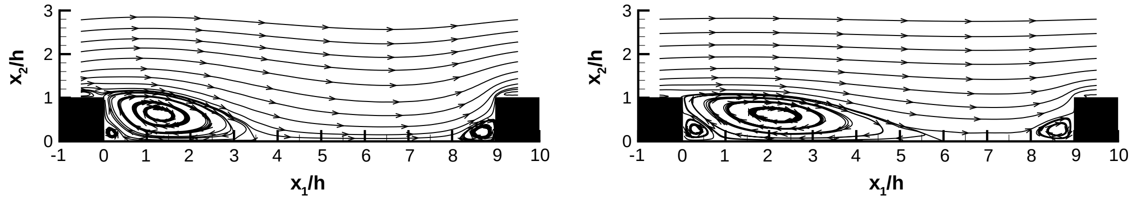

(b) $Ro = 0.38$ (c) $Ro = -0.38$

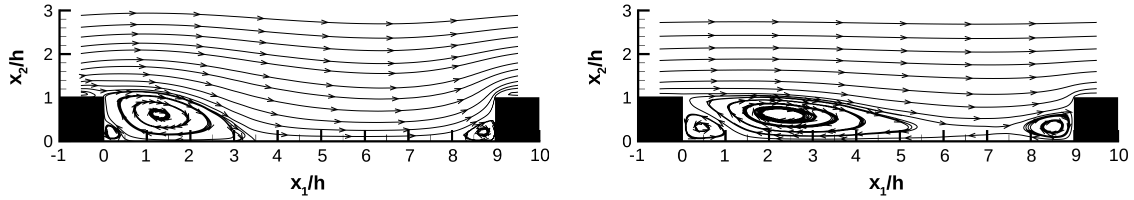

(d) $Ro = 0.6$ (e) $Ro = -0.6$

FIGURE 5.4: Time- and spanwise-averaged streamlines for flow without rotation ($Ro = 0$), under counter-clockwise rotations ($Ro = 0.38$ and $Ro = 0.6$) and under clockwise rotations ($Ro = -0.38$ and $Ro = -0.6$).

When rotation is imposed on the rib-roughened channel, as shown in Figs. 5.4(b)–(e), vortices A, B and C remain visible. However, the system rotation significantly modifies the mean flow features. In particular, the recirculation bubble B shrinks under counter-clockwise rotations in Figs. 5.4(b) and (d), whereas extends in the streamwise direction in a more pronounced manner under clockwise rotations in Figs. 5.4(c) and (e). The physical mechanism underlying this phenomenon is similar to that revealed by Rothe and Johnston [101] in their study of a backward-facing step flow subjected to the spanwise rotation. When the free shear layer is destabilized by counter-clockwise rotation, the entrainment from the outer flow into the recirculation bubble B is enhanced. The motion of entrained fluid reduces the pressure in the separated area relative to the core region of the channel, which results in a greater normal pressure gradient towards the ribbed wall. This greater pressure gradient induces a stronger streamline curvature, which further leads to an earlier reattachment and a reduction in the reattachment length L_R. As shown in Figs. 5.4(b) and (d), under counter-clockwise rotation, the streamlines in the outer flow are strongly tilted toward the roughened wall. Furthermore, as Ro increases from 0.38 to 0.6, it is observed that the size of the separation bubble changes little. The flow reattaches the floor at $L_R/h \approx 3.50$ for both $Ro = 0.38$ and $Ro = 0.6$.

Under clockwise rotation, the trends are opposite to those in the cases under counter-clockwise rotation analyzed above, and some of the discussions are skipped here to keep the analysis concise. As shown in Figs. 5.4(c) and (e), under clockwise rotation, the streamlines in the outer flow tend to be horizontally aligned with the floor of the inter-rib region. It is expected that at a higher clockwise rotating speed, the reattachment point moves further downstream as the size of separation bubble B expands. As shown in Fig. 5.4(e), the separation bubble B eventually bridges with the recirculating vortex C immediately upstream of the successive rib at $Ro = -0.6$. Consequently, the reattachment length covers the entire inter-rib region ($L_R = 9h$ as shown in Fig. 5.5(e)), switching from k-type to intermediate or d-type roughness as defined Perry *et al.* [91]. This interesting phenomenon has an important implication that the classification of roughness types relies not only on the pitch ratio L_p/h, but also on the rotation number Ro in the context of rotating rib-roughened channel flows.

Table 5.1 compares the time-averaged reattachment length L_R predicted by the current simulations and those in the PIV experiments of Coletti *et al.* [42]. As shown in the table, the values of L_R obtained from hybrid RANS/LES are in good agreement with the measured values. Without rotation, the reattachment length L_R obtained using the current hybrid RANS/LES is about $3.96h$. The reattachment length value for non-rotating rib-roughened flows has been extensively studied in literature based on slightly different geometric and flow conditions. For example, the value obtained in the experiment of Rau *et al.* [102] using laser Doppler velocimetry was about $4.12h$ for $Re = 3.0 \times 10^4$ and $L_3/L_2 = 1$, and the value obtained in the full LES simulation of Tafti [103] was about $4.10h$ for $Re = 2.0 \times 10^4$ and $L_3/L_2 = 1$. Islam *et al.* [104] further confirmed that the flow reattachment remains approximately constant at $L_R/h = 4.00$ once the Reynolds number reaches a critical value of 1.5×10^4.

TABLE 5.1: Comparison of reattachment length L_R obtained in current hybrid RANS/LES and in previous studies for a fully-developed turbulent flow in a rib-roughened channel with and without spanwise system rotations.

	L_3/L_2	h/H	L_p/h	Re	Ro	L_R/h
Present hybrid RANS/LES	0.9	0.1	10	1.5×10^4	0	3.96
					0.38	3.50
					-0.38	6.08
Coletti *et al.* [42], PIV	0.9	0.1	10	1.5×10^4	0	3.85
					0.38	3.45
					-0.38	6.00

As shown in Table 5.1, in comparison with the non-rotating case, the reattachment length L_R increases by 53.5% to the value of $6.08h$ under clockwise rotation ($Ro = -0.38$), and decreases by 11.6% to $3.50h$ under counter-clockwise rotation ($Ro = 0.38$). The increase in reattachment length due to the stabilizing effect of the Coriolis force (under clockwise rotation) is much larger than its reduction due to the destabilizing effect (under counter-clockwise rotation), although the magnitude of rotating speed $|\Omega|$ is identical in both scenarios. Figure 5.5 shows the time-averaged values of the reattachment length at different rotation numbers varying from -0.6 to 0.6. From Fig. 5.5, it is evident that the reattachment length L_R predicted using the current hybrid approach agrees very well with that obtained from PIV measurements by Coletti *et al.* [41–43], although data of only five rotation numbers were available from the PIV experiments. As shown in Fig. 5.5, under clockwise rotation, the reattachment length approaches a maximum of $9h$ (as indicated using the upper horizontal dashed line) at $Ro = -0.6$. Under counter-clockwise rotation, as shown in Fig. 5.5, the reattachment length asymptotes to a constant level (as indicated using the lower horizontal dashed line) around $3.50h$ as Ro increases from 0.3 to 0.6. Similar observations have also been reported in the previous studies on the backward-facing step flow under counter-clockwise rotations, including, e.g. PIV measurements of Rothe and Johnston [101] and Visscher and Andersson [105], and DNS study of Barri and Andersson [106]. These studies have shown that the reattachment length L_R remains constant for $Ro \geq 0.8$ (based on the bulk velocity and channel height

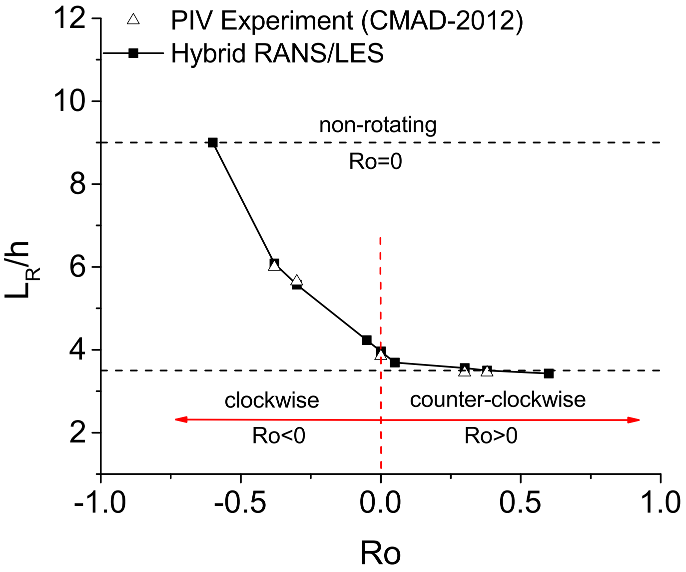

FIGURE 5.5: Time-averaged values of reattachment length L_R at different rotation numbers under both clockwise and counter-clockwise rotations (non-dimensionalized using the rib height h).

downstream of the step).

The reattachment length shown in Table 5.1 and Fig. 5.5 has been averaged over a period of time for both stationary and rotating rib-roughened channel flows. The instantaneous reattachment point, however, moves back and forth within the inter-rib region due to the flapping motion of the recirculation bubble B. This phenomenon has also been reported in similar studies on separating/reattaching turbulent flows over a backward-facing step [107, 108] and a blunt body [109]. In the current study, the instantaneous reattachment length of the rotating rib-roughened channel flow is identified when the instantaneous wall shear stress approaches zero. Figure 5.6 shows the probability density function (PDF) of the instantaneous streamwise location of the reattachment point. It is evident that the PDF exhibits a Gaussian-like distribution for both non-rotating and rotating rib-roughened channel flows. As shown in Fig. 5.6, for the non-rotating case ($Ro = 0$), the mode occurs at $3.99h$, which matches the time-averaged value of the reattachment length $3.96h$ listed in Table 5.1. Furthermore, it is seen from the figure that at $Ro = 0$, the PDF value is prominent within the zone $3.40h$–$4.59h$ (with 95% probability). As such, the streamwise length of the zone within

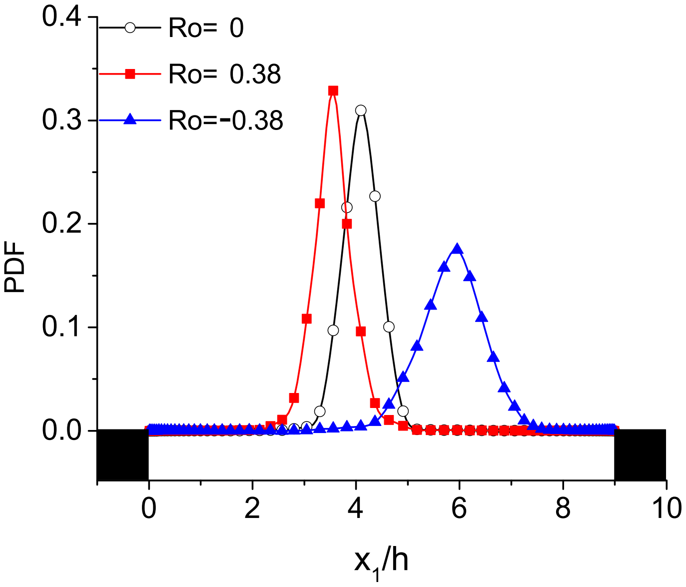

FIGURE 5.6: Probability density function of the streamwise location of the instantaneous reattachment point for flow without rotation ($Ro = 0$), under counter-clockwise rotation ($Ro = 0.38$) and under clockwise rotation ($Ro = -0.38$).

which the instantaneous reattaching point falls with a high probability is determined to be $1.19h$. This result is consistent with the experimental value $1.20h$ reported by Liu *et al.* [93].

It is clear from the figure that the system rotation has a significant impact on the mode of the PDF. The mode is $x_1/h = 3.57$ and 6.04 when the flow is subjected to counter-clockwise ($Ro = 0.38$) and clockwise ($Ro = -0.38$) rotations, respectively. These results conform well with the mean values of the reattachment length L_R presented in Table 5.1. The upstream and downstream shifts of the reattachment point (associated with a reduction and an extension of the reattachment zone, respectively) under counter-clockwise and clockwise rotations, are direct consequences of the switching of the Corioris force direction. The results observed here in the PDF of the streamwise location of the instantaneous reattachment point under different rotating conditions are also consistent with the vortex patterns shown previously in Fig. 5.4 based on time-averaged streamlines.

Figure 5.7 compares contours of the time- and spanwise-averaged pressure field under three different rotating conditions. The pressure has been non-dimensionalized as $C_p = (\langle p\rangle - \langle p_0\rangle)/q_0$, where $\langle p_0\rangle$ is the reference static pressure at the corner of the lee side of the rib and q_0 is the reference dynamic pressure defined as $q_0 = \frac{1}{2}\rho U_b^2$. In fluid mechanics, C_p is also referred to as the pressure coefficient. In order to facilitate the comparison of the flow structures, the pressure contours in these three subfigures are illustrated based on the same legend scale. As is evident in Figs. 5.7(a)–(c), for both rotating and non-rotating cases, there are two distinct pressure regions: firstly, the stagnation region which is formed in front of a rib and has the highest static pressure; secondly, the recirculation region which is located immediately behind the rib and features the lowest pressure of the flow field. Because of the pressure difference between the windward and leeward of the rib, a net form drag acts on the rib, and the fluid field exhibits complex vortex interactions and flow separations over the rib. These two pressure regions are essential to explain the underlying physical mechanism of vortex features in Fig. 5.4. Furthermore, Figs. 5.7(a)–(c) clearly demonstrate the effect of the Coriolis force on both the recirculation and stagnation regions. By comparing Fig. 5.7(b) with Fig. 5.7(a), it is clear that the size of the stagnation region with higher static pressure is magnified under counter-clockwise rotation (for $Ro = 0.38$), meanwhile, the recirculation region is shortened. In contrast, as shown in Fig. 5.7(c), under clockwise rotation, the stagnation region is much reduced and is limited to the windward of the subsequent rib, which leaves more space in the streamwise direction for the recirculation region behind the upstream rib to grow. The flow structures shown here in Fig. 5.7 using the pressure field under different rotating conditions are consistent with the streamline patterns demonstrated previously in Fig. 5.4.

5.3.4 Model Coefficients

Figure 5.8 shows time- and spanwise-averaged profiles of model coefficients $\langle C_S\rangle$ and $\langle C_N\rangle$ along the wall-normal direction. The profiles were extracted at the midpoint $(x_1/h = 4.5)$ between two ribs. In order to demonstrate the effects of rotation on the model coefficients, three different rotation numbers ($Ro = 0$, -0.38 and 0.38) are

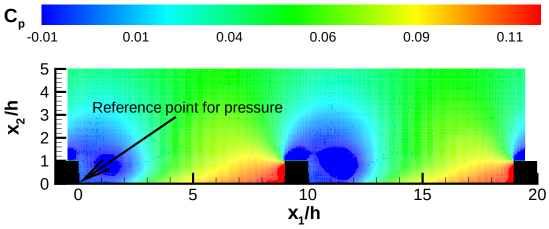

(a) $Ro = 0$

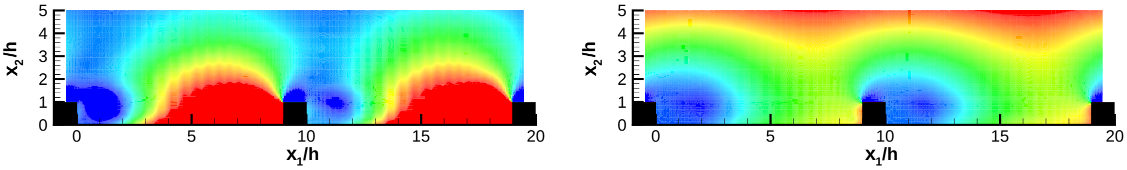

(b) $Ro = 0.38$ (c) $Ro = -0.38$

FIGURE 5.7: Contours of the non-dimensionalized pressure field C_p for flow without rotation ($Ro = 0$), under counter-clockwise rotation ($Ro = 0.38$) and under clockwise rotation ($Ro = -0.38$). The pressure coefficient is defined as $C_p = (\langle p \rangle - \langle p_0 \rangle)/q_0$, where $\langle p_0 \rangle$ is the reference static pressure at the corner of the lee side of the rib.

compared. In Fig. 5.8, the profiles of $\langle C_S \rangle$ for the DSM are displayed in the LES region (for $0.2 \leq x_2/h \leq 9.8$), while the profiles of $\langle C_N \rangle$ for the dynamic forcing scheme are displayed across the entire channel (for $0 \leq x_2/h \leq 10$). As shown in Fig. 5.8, the profiles of model coefficients exhibit a clear anisotropy in the wall-normal direction due to the restriction from the channel walls and the influence of the ribs. The averaged value is positive for $\langle C_S \rangle$, but negative for $\langle C_N \rangle$. As shown in Fig. 5.8, for the non-rotating rib-roughened channel flow case (i.e., at $Ro = 0$), $\langle C_N \rangle$ reduces to zero at both walls and its magnitude peaks at the rib height ($x_2/h = 1.0$). At the rib height, there is a strong shear layer developed along the rib top, which results in large TKE production (turbulence activities) transported to the downstream region. As shown in Fig. 5.8, in comparison with the non-rotating case, the magnitude of the peak increases under counter-clockwise rotation (for $Ro = 0.38$) but decreases under clockwise rotation (for $Ro = 0.38$). This is consistent with the previous analysis of Table 5.1 and Figs. 5.4 and 5.6 that in the region close to the rib-roughened wall, the effect of the Coriolis force is destabilizing under counter-clockwise rotation and stabilizing under clockwise rotation, respectively.

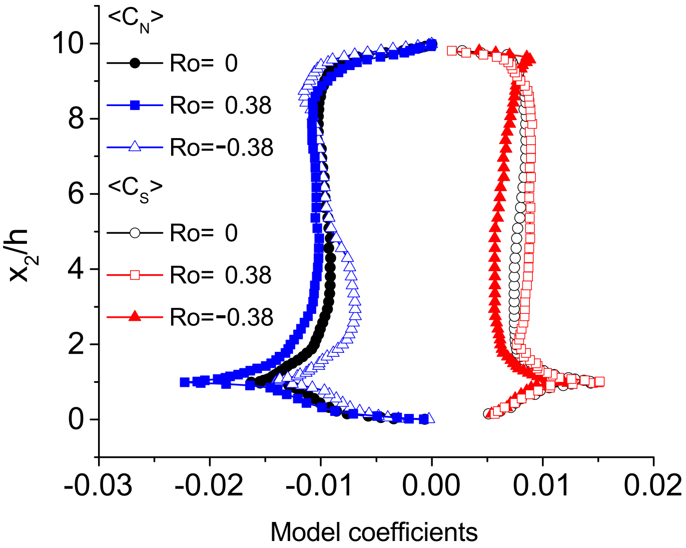

FIGURE 5.8: Profiles of time- and spanwise-averaged model coefficients at midpoint between two ribs for $x_1/h = 4.5$: $\langle C_S \rangle$ for the DSM (within the range $0.2 \leq x_2/h \leq 9.8$), and $\langle C_N \rangle$ for the dynamic forcing (within the range $0 \leq x_2/h \leq 10$).

5.3.5 Mean Resolved Velocity

Figure 5.9 compares the predicted wall-normal profiles of the mean resolved streamwise velocity against the PIV data of Coletti *et al.* [42] at three rotation numbers for stationary, counter-clockwise rotating, and clockwise rotating cases. Theses profiles were extracted at five different streamwise locations for $x_1/h = 0$, 2, 4, 6 and 8. As shown in Figs. 5.9(a)–(c), for both non-rotating and rotating cases, results obtained from current simulations are in good conformation with the measurement data of Coletti *et al.* [42] at all five streamwise locations. The velocity profiles in Figs. 5.9(a)–(c) are closely related to the vortex structures demonstrated in Figs. 5.4(a)–(c). For the non-rotating case ($Ro = 0$), as shown in Fig. 5.9(a), a strong shear layer is formed at the rib top surface which features a very large mean vertical velocity gradient ($\partial\langle\bar{u}_1\rangle/\partial x_2$). At $x_1/h = 2$, negative streamwise velocities are clearly seen in the near-wall region, illustrating a reverse flow pattern within the recirculation bubble B behind the rib. The reattachment point which features zero-velocity and zero-wall-shear (i.e., $\partial\langle\bar{u}_1\rangle/\partial x_2 = 0$ at the wall) is evident at $x_1/h = 4$. Moving downstream from the reattachment point, the flow re-establishes a wall shear flow along the floor

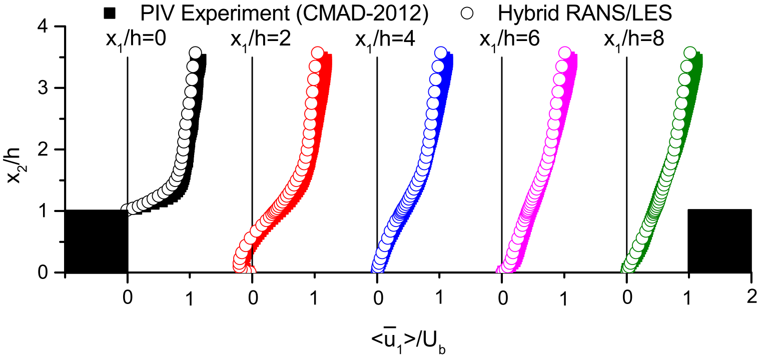

(a) $Ro = 0$

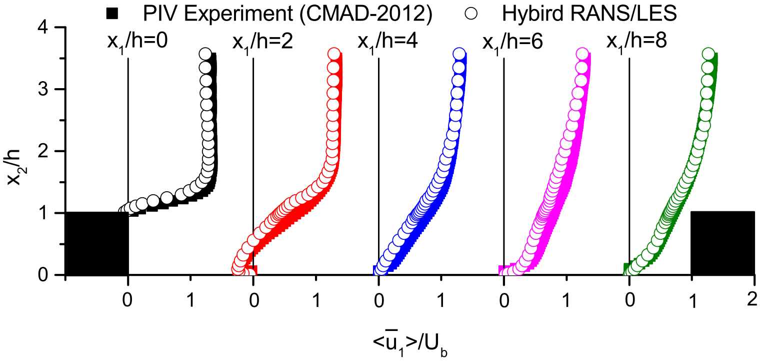

(b) $Ro = 0.38$

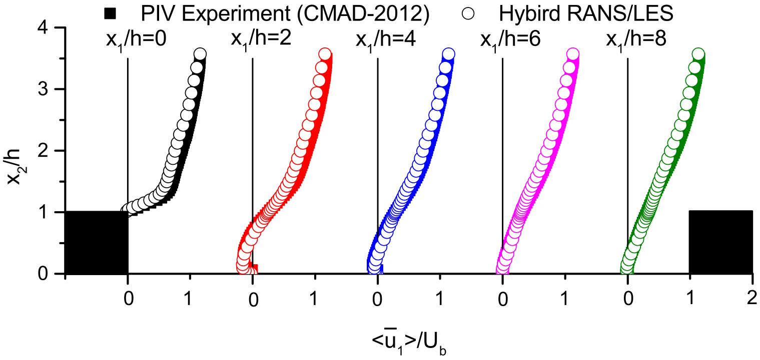

(c) $Ro = -0.38$

FIGURE 5.9: Resolved mean streamwise velocity profile for flow without rotation ($Ro = 0$), under counter-clockwise rotation ($Ro = 0.38$) and under clockwise rotation ($Ro = -0.38$).

with positive streamwise velocities reappearing at $x_1/h = 6$ and 8.

In comparison with the non-rotating case, the magnitude of the mean streamwise velocity for the counter-clockwise rotating case ($Ro = 0.38$) shown in Fig. 5.9(b) increases at all streamwise locations. This difference is caused by the Coriolis force, which accelerates the flow speed on the ribbed side under counter-clockwise rotation. Furthermore, as the size of the recirculation bubble B shrinks in size, an earlier reattachment occurs, which leaves more space for the flow to accelerate before running into the next rib. This conclusion is apparent if we compare the mean streamwise velocity profiles at $x_1/h = 4$ in Figs. 5.9(a) and 5.9(b). At this location, the flow reattaches the floor in the non-rotating case ($Ro = 0$) but a developing boundary layer can be already observed in the counter-clockwise rotating case ($Ro = 0.38$). As shown in Fig. 5.9(b), in the further downstream region, the flow in the counter-clockwise rotating case approaches the subsequent rib with higher momentum. For the clockwise rotating case ($Ro = -0.38$) as shown in Fig. 5.9(c), the development of the mean velocity profile near the ribbed wall delays significantly in comparison with that for the counter-clockwise rotating case. This is because the reattachment point of the flow moves further downstream to $x_1/h = 6$ at $Ro = -0.38$ (demonstrated previously in Fig. 5.4(c)). By comparing Fig. 5.9(c) with Fig. 5.9(a), the magnitude of the mean streamwise velocity in the region near the rib-roughened wall decreases significantly, which is consistent with the previous conclusion on the stabilizing effect of the Coriolis force in this region under clockwise rotation.

Figure 5.10 demonstrates the effects of rotation on the mean resolved wall-normal velocity $\langle \bar{u}_2 \rangle$ along the streamwise direction. The velocity profiles of the wall-normal component were extracted at height $x_2/h = 1.1$. The pattern exhibited in the profiles of $\langle \bar{u}_2 \rangle$ can be explained using the vortex structures shown previously in Fig. 5.4. In the immediate downstream region of the rib (for $0 < x_1/h < 1$), the value of $\langle \bar{u}_2 \rangle$ is weakly positive for all three rotation numbers. This is due to a combined effect from the corner vortex A and recirculation bubble B, both of which direct the streamlines upwards approaching the rear top edge of the rib. Within the downstream region for $1 < x_1/h < 6$, the value of $\langle \bar{u}_2 \rangle$ becomes negative for all three test cases. The strong shear layer generated by the rib is bent downwards and reattaches the ribbed floor, resulting in the recirculation bubble B. However, in response to the system rotation, the Coriolis force appears, pointing towards or away from the ribbed wall under counter-clockwise or clockwise rotation, respectively. As shown previously

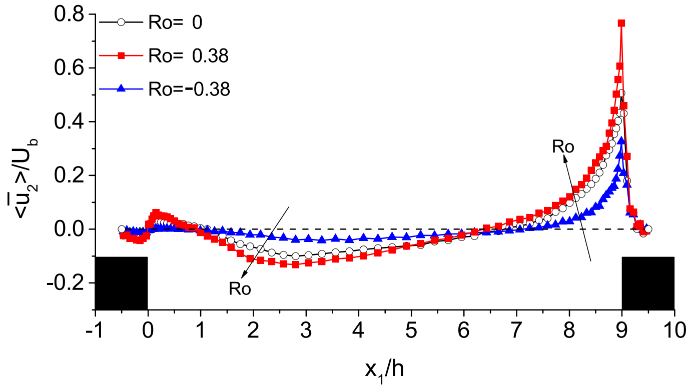

FIGURE 5.10: Comparison of resolved mean wall-normal velocity profile at height $x_2/h = 1.1$, for flow without rotation ($Ro = 0$), under counter-clockwise rotation ($Ro = 0.38$) and under clockwise rotation ($Ro = -0.38$).

in Figs. 5.4-5.6, the reattachment point moves towards or away from the upstream rib under counter-clockwise or clockwise rotation, respectively. This explains the pattern exhibited in Fig. 5.10 that the value of $|\langle\bar{u}_2\rangle|$ decreases monotonically as Ro decreases within $1 < x_1/h < 6$. This maximum magnitude of the downward velocity in the counter-clockwise rotating case ($Ro = 0.38$) is 30.1% higher than that in the non-rotating case ($Ro = 0$), and is three times higher than that under clockwise rotation ($Ro = -0.38$). An understanding of this physical mechanism is particularly important in the cooling of turbomachinery and rotating electronic devices, as it influences the flow rate of the cold fluid from the mainstream towards the hot roughened surfaces. In the further downstream region for $7 < x_1/h < 9$, the value of $\langle\bar{u}_2\rangle$ becomes positive again. Furthermore, its value increases monotonically as Ro increases. This flow feature is caused by the blockage of the subsequent rib in its immediate upstream region. As the flow impinges upon the rib, vortex C is formed in the lower front corner of the subsequent rib (see, Fig. 5.4), which then diverts the flow upwards. The fact that the flow under counter-clockwise rotation has the largest peak value of $\langle\bar{u}_2\rangle$ is consistent with the previous analysis of Figs. 5.4 and 5.9: the flow reattachment occurs earlier under counter-clockwise rotation, which then allows the boundary layer to develop under a lower adverse streamwise pressure gradient, approaching the subsequent rib with a higher momentum.

5.3.6 Second-Order Flow Statistics

Figure 5.11 compares the predicted and measured wall-normal profiles of the resolved turbulent shear stress $-\langle \bar{u}_1'' \bar{u}_2'' \rangle$ at three rotation numbers. As shown in Figs. 5.11(a)–(c), at all five streamwise locations, the shear stresses reach a peak value at a certain elevation. When the flow passes over the rib, a boundary layer develops very briefly on the rib top surface, which reduces the value of $-\langle \bar{u}_1'' \bar{u}_2'' \rangle$ to zero at the rib top and creates a peak immediately above it. Such pattern is evident in the vertical profile of $-\langle \bar{u}_1'' \bar{u}_2'' \rangle$ at the leeward side ($x_1/h = 0$) of the rib in Fig. 5.11(a). The strong shear layer created on the rib top surface extends into the downstream region of the rib, which significantly increases the turbulent activities around the rib height. Due to the recirculation flow pattern, the vertical position for the peak value of the mean resolved turbulent shear stress shifts towards the floor within $0 < x_1/h < 4$. After the reattachment point, the peak position moves progressively upwards as the wall boundary layer redevelops along the floor. Although the strong free shear layer generated at the rib top is the main source for the turbulent shear stress, the Coriolis force effect on the magnitude of $-\langle \bar{u}_1'' \bar{u}_2'' \rangle$ is evident by comparing Figs. 5.11(a)–5.11(c). The peak value of the resolved turbulent shear stress is twice higher in the counter-clockwise rotating case ($Ro = 0.38$) than in the non-rotating case ($Ro = 0$); however, the peak value in the clockwise rotating case ($Ro = -0.38$) is only half of that in the non-rotating case. The increase and decrease in the value of $-\langle \bar{u}_1'' \bar{u}_2'' \rangle$ under counter-clockwise and clockwise rotations, respectively, verifies again the destabilizing and stabilizing effects of the Coriolis force on the flow within the rib-roughened wall region under these two different system rotations.

In order to visualize the shear layer created on the rib top surface and further investigate its impact on the level of turbulence quantities, contours of the resolved TKE are displayed in Figs. 5.12(a)–(c) for three different rotating conditions. In the figure, the value of TKE has been non-dimensionalized using U_b^2 and its contours are displayed based on the same legend scale in three subfigures in order to facilitate the comparisons. As shown in Figs. 5.12(a)–(c), the strong shear layer triggered by the

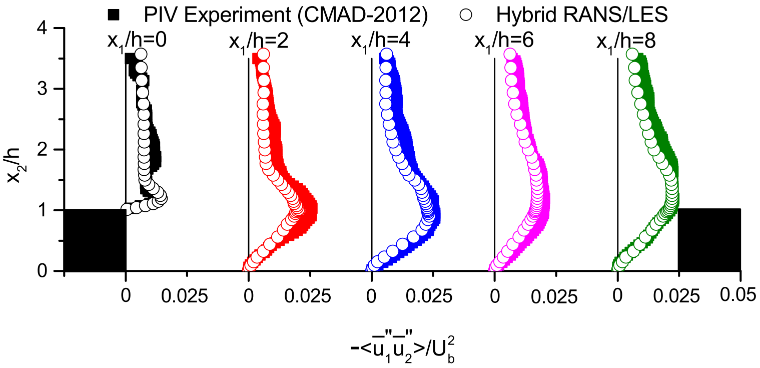

(a) $Ro = 0$

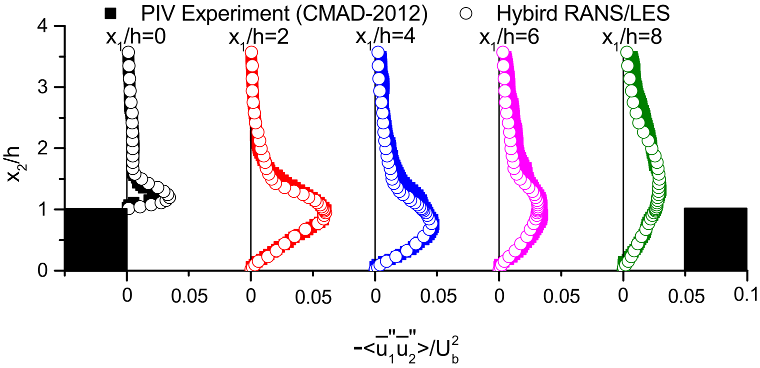

(b) $Ro = 0.38$

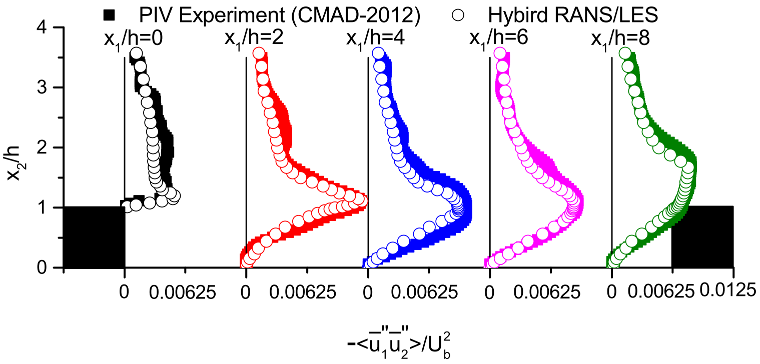

(c) $Ro = -0.38$

FIGURE 5.11: Resolved turbulent shear stress profile for flow without rotation ($Ro = 0$), under counter-clockwise rotation ($Ro = 0.38$) and under clockwise rotation ($Ro = -0.38$).

rib top immediately downstream of it is common to both non-rotating and rotating cases. The maximum TKE occurs at the top front edge of the rib where the strong shear layer starts developing on the rib top surface. At this special location, the flow directly strikes the top front edge of the rib. The strong shear layer issued by the

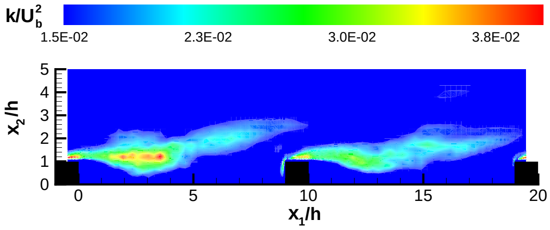

(a) $Ro = 0$

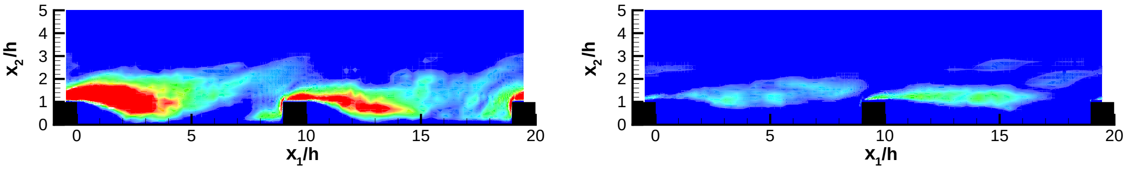

(b) $Ro = 0.38$ (c) $Ro = -0.38$

FIGURE 5.12: Contours of non-dimensionalized TKE for flow without rotation ($Ro = 0$), under counter-clockwise rotation ($Ro = 0.38$) and under clockwise rotation ($Ro = -0.38$).

rib top soon separates and further triggers flow instability. As the flow goes forward, the TKE level reduces but remains significant in the wake region behind the rib. For the non-rotating case ($Ro = 0$), as shown in Fig. 5.12(a), the shear layer curves downwards towards the floor within a length of about $4h$ behind the rib before the flow reattaches the floor. After the flow reattachment point, the shear layer then curves upwards towards the outer flow as the boundary layer redevelops along the floor.

The effects of the Coriolis force on the shear layer and level of TKE become clear by comparing these three figures. The level of TKE near the rib-roughened wall region is the highest in the counter-clockwise rotating case (for $Ro = 0.38$) but is the lowest in the clockwise rotating case (for $Ro = -0.38$). As shown in Fig. 5.12(b), the bending of the strong shear layer towards the floor is the most effective under counter-clockwise rotation. However, as shown in Fig. 5.12(c), the shear layer appears to be more horizontally aligned along the streamwise direction under clockwise rotation, as a consequence of the elongated recirculation zone.

Figures 5.13 and 5.14 show time- and spanwise-averaged profiles of the resolved streamwise and wall-normal RMS velocities, respectively. The resolved RMS velocity

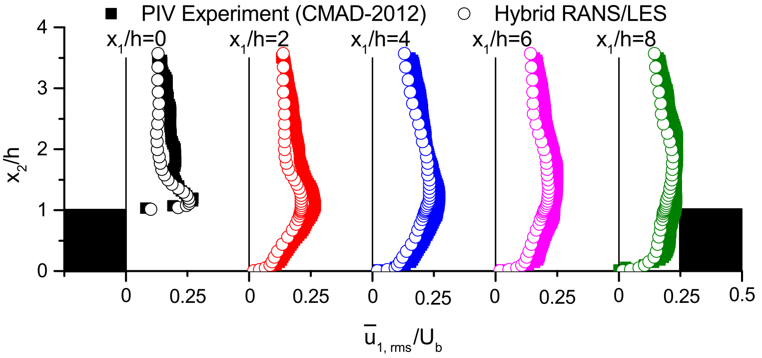

(a) $Ro = 0$

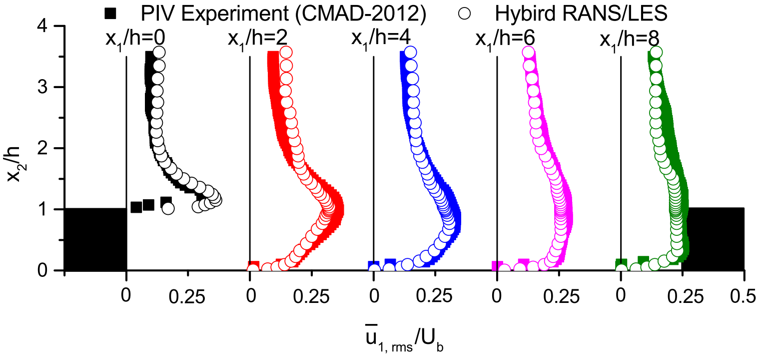

(b) $Ro = 0.38$

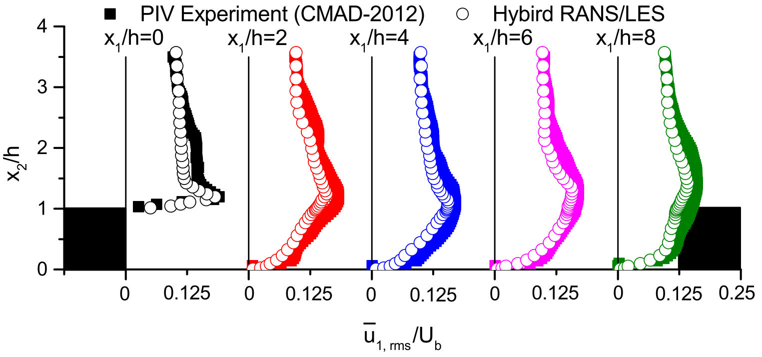

(c) $Ro = -0.38$

FIGURE 5.13: Resolved streamwise RMS velocity profile for flow without rotation ($Ro = 0$), under counter-clockwise rotation ($Ro = 0.38$) and under clockwise rotation ($Ro = -0.38$).

profiles are demonstrated at five streamwise locations for $x_1/h = 0$, 2, 4, 6 and 8. In order to compare the influence of the Coriolis force on resolved velocity fluctuations, three rotation numbers (i.e., $Ro = 0$, 0.38 and -0.38) are compared in Figs. 5.13 and 5.14. Quantities presented in these figures are normalized using the bulk velocity

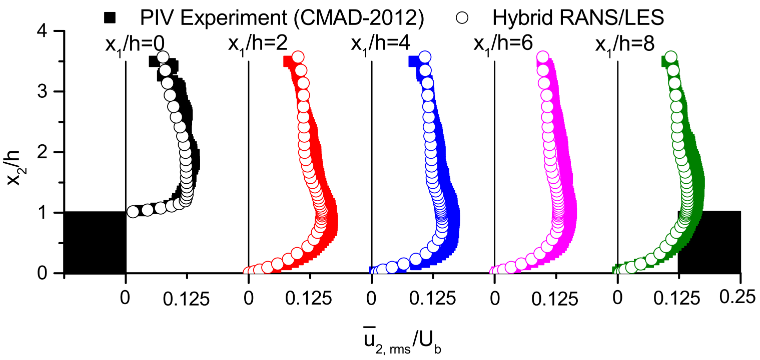

(a) $Ro = 0$

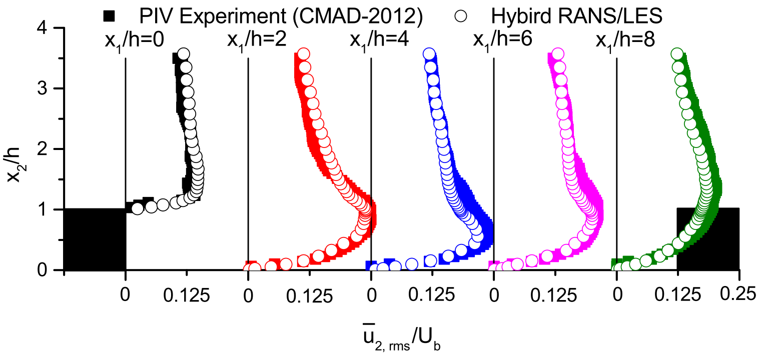

(b) $Ro = 0.38$

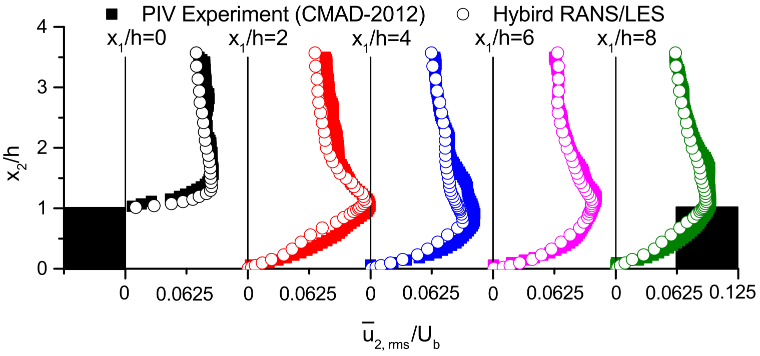

(c) $Ro = -0.38$

FIGURE 5.14: Resolved wall-normal RMS velocity profile for flow without rotation ($Ro = 0$), under counter-clockwise rotation ($Ro = 0.38$) and under clockwise rotation ($Ro = -0.38$).

U_b. As is evident in Figs. 5.13 and 5.14, in general, the profiles predicted by hybrid RANS/LES are in good agreement with the PIV measurement data of Coletti *et al.* [42] for both non-rotating ($Ro = 0$) and rotating ($Ro = \pm 0.38$) cases. As shown in Fig. 5.13(a), for the non-rotating case, the maximum value of the streamwise RMS velocity at $x_1/h = 0$ occurs immediately above the rib (around $x_2/h = 1.2$), which is about $\bar{u}_{1,\text{rms}} = 0.26U_b$. When the flow passes over the rib, a strong shear layer (with a large vertical velocity gradient) is created on the rib top, which then increases the turbulent activities and shear production rate for TKE. As the streamwise distance from the rib increases from $x_1/h = 2$ to 4, the vertical position corresponding to the peak values drops to reflect the recirculation flow pattern and reattaching process. In the further downstream region after the reattachment point (for $x_1/h > 4$), the vertical position for the peak value of $\bar{u}_{1,\text{rms}}$ keeps elevating as the boundary layer develops. By comparing Fig. 5.13(b) with Fig. 5.13(a), it is clear that the magnitude of the streamwise RMS velocity becomes much larger (with a maximum 40.8% increase in the peak value) in the counter-clockwise rotation case ($Ro = 0.38$) than that in the non-rotating case. However, as shown in Fig. 5.13(c), the peak value of $\bar{u}_{1,\text{rms}}$ under clockwise rotation (at $Ro = -0.38$) is 29.5% lower than that in the non-rotating case. These changes in the RMS velocity levels are consequences of the Coriolis force, which points to the rib-roughened wall and destabilizes the near-wall flow under counter-clockwise rotation, and does the opposite under clockwise rotation. Fig. 5.14 compares wall-normal RMS velocity ($\bar{u}_{2,\text{rms}}$) profiles at five streamwise locations under different rotating conditions. The Coriolis force effects on the streamwise development of $\bar{u}_{2,\text{rms}}$ and its peak location are similar to those of the streamwise RMS velocity ($\bar{u}_{1,\text{rms}}$) analyzed in Fig. 5.13, and detailed discussions are skipped to keep the analysis concise.

From the previous analysis, it is understood that the Coriolis force (and the T-G vortices induced by it) drastically changes the profiles of both first- and second-order flow statistics in a rotating rib-roughened channel. As revealed in the experimental study of Johnston *et al.* [69] and DNS study of Kristoffersen and Andersson [20] on rotating turbulent flows in a smooth plane channel, the production terms in the transport equations of the resolved turbulent stresses have a significant influence on the value of the resolved turbulent shear stresses and TKE. Because the effect of ribs and the effect of rotation mutually influence each other, the production terms for the resolved turbulent stresses are more complicated than those in Table 4.2 for the plane channel flow without ribs [20, 69]. As shown in Figs. 5.11–5.14, the Coriolis force effects on both the turbulent shear stresses and TKE components are very similar under the same rotating condition. In view of this, the example of the wall-normal turbulent stress component $\langle \bar{u}_2''^2 \rangle$ is used to explain how rotation affects its magnitude through its production terms in the following context.

The production rate of $\langle \bar{u}_2''^2 \rangle$ is related to three factors, i.e. the resolved turbulent stresses, rotational stresses and SGS stresses. According to Xun *et al.* [61], the production rate of the wall-normal turbulent stress component $\langle \bar{u}_2''^2 \rangle$ arising from the mean resolved turbulent (shear and wall-normal) stresses is

$$P_{22} = -2\left(\langle \bar{u}_1'' \bar{u}_2'' \rangle \frac{\partial \langle \bar{u}_2 \rangle}{\partial x_1} + \langle \bar{u}_2''^2 \rangle \frac{\partial \langle \bar{u}_2 \rangle}{\partial x_2} \right) \quad , \tag{5.4}$$

the production rate arising from the rotational stress due to the Coriolis acceleration is

$$G_{22} = -4\Omega \langle \bar{u}_1'' \bar{u}_2'' \rangle \quad , \tag{5.5}$$

and the production rate arising from the SGS stresses τ_{ij} is

$$O_{22} = 2\left(\left\langle \tau_{12} \frac{\partial \bar{u}_2''}{\partial x_1} \right\rangle + \left\langle \tau_{22} \frac{\partial \bar{u}_2''}{\partial x_2} \right\rangle + \left\langle \tau_{23} \frac{\partial \bar{u}_2''}{\partial x_3} \right\rangle \right) \quad . \tag{5.6}$$

Figures 5.15 and 5.16 show the production rate (G_{22}) due to the rotational stress and the total production rate ($P_{22}+G_{22}+O_{22}$) for the resolved wall-normal turbulent stress, respectively. The production rate profiles shown in these figures were obtained at the streamwise location $x_1/h = 4$ and have been non-dimensionalized using U_b^3/h. In order to investigate the rotation effects on the production rates, in total 9 rotation numbers varying from -0.6 to 0.6 have been considered in the current comparative study. For the non-rotating case ($Ro = 0$), $G_{22} \equiv 0$ holds strictly across the entire channel (because $\Omega \equiv 0$), which feature is well reproduced by hybrid simulations and shown in Fig. 5.15. As a consequence, the production rate of $\langle \bar{u}_2''^2 \rangle$ depends exclusively upon the other two production terms P_{22} and O_{22}, both of which are expected to be sensitive to the existence of the ribs. Indeed, as shown in Figs. 5.16 and 5.17, for the non-rotating case, the profiles of $\langle \bar{u}_2''^2 \rangle$ (or $\bar{u}_{2,\mathrm{rms}}$) and its total production rate are

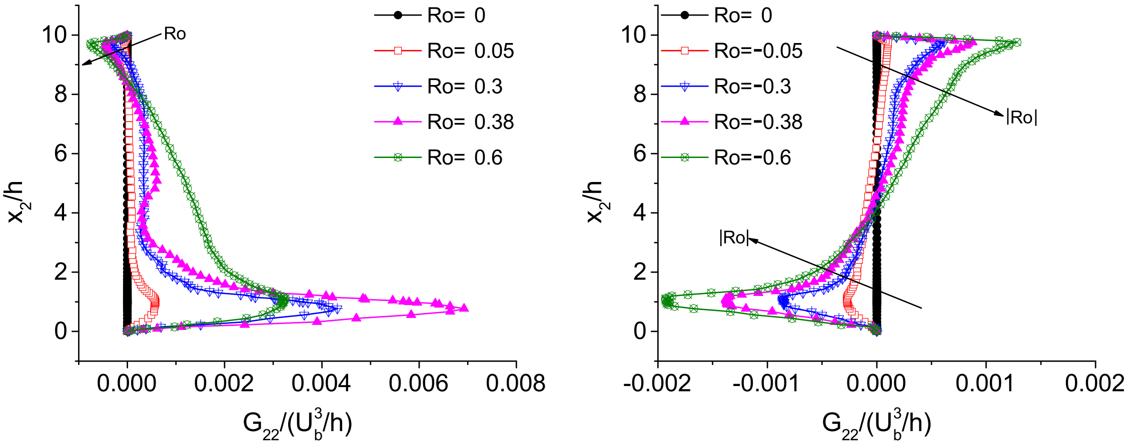

(a) Counter-clockwise rotation (b) Clockwise rotation

FIGURE 5.15: Production rate (G_{22}) due to the rotational stress for the wall-normal component of resolved turbulent stresses at different rotation numbers at the streamwise location $x_1/h = 4$.

asymmetrical in the wall-normal direction and peak near the ribbed wall, which is a direct result of the strong shear layer and large mean velocity gradients generated by the rib top.

As shown in Figs. 5.15(a) and (b), the level of G_{22} across the rib-roughened channel is significantly altered by both counter-clockwise and clockwise rotations. This feature is expected, because according to Eq. (5.5), the strength of G_{22} is linearly proportional to the system rotating speed Ω. As pointed out by Visscher and Andersson [105], the rotational production term G_{22} is a key parameter in understanding the influence of rotation on turbulent shear flows at moderate rotating speeds. It is worthwhile to note that G_{22} arises from the correlation between the velocity fluctuations $\bar{u}_2''$ and the fluctuating Coriolis force $-2\Omega\bar{u}_1''$ in the wall-normal direction. Therefore, the sign of G_{22} depends on the condition whether the wall-normal component of the fluctuating Coriolis force acts to promote or suppress the wall-normal velocity fluctuations $\bar{u}_2''$.

Under counter-clockwise rotation ($Ro > 0$), the effect of the Coriolis force is to destabilize the rib-roughened wall and $G_{22} > 0$ holds in this near-wall region. As shown in Fig. 5.15(a), for small and moderate rotation numbers (for $Ro \leq 0.38$), G_{22} maintains positively-valued and increases with Ro near the rib-roughened wall, which

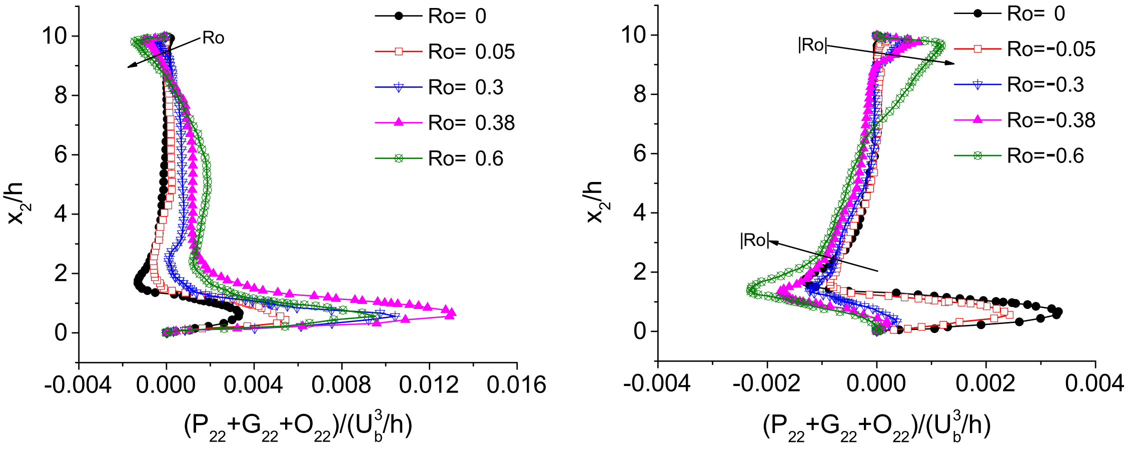

(a) Counter-clockwise rotation (b) Clockwise rotation

FIGURE 5.16: Total production rate ($P_{22}+G_{22}+O_{22}$) for the wall-normal component of resolved turbulent stresses at different rotation numbers at the streamwise location $x_1/h = 4$.

tends to increase $\langle \bar{u}_2''^2 \rangle$. Indeed, as shown in Fig. 5.17(a), the level of $\langle \bar{u}_2''^2 \rangle$ increases monotonically as Ro increases from 0 to 0.38. As the rotation number continues to increase from 0.38 to 0.6, re-stabilization occurs, and as a result, the level of G_{22} decreases in the region near the rib-roughened wall. As shown in Fig. 5.16(a) and Fig. 5.17(a), respectively, this further leads to a reduction in the total production rate and in the level of $\langle \bar{u}_2''^2 \rangle$ near the rib-roughened wall (as Ro increases from 0.38 to 0.6). As shown in Figs. 5.15–5.17, the vertical profiles of the production rates and the value of $\bar{u}_{2,\mathrm{rms}}$ are asymmetrical under the combined influences from the system rotation and presence of ribs. In contrast to the characteristics of the flow near the ribbed (or, pressure) side of the channel, near the smooth (or, suction) side (located at $x_2/h = 10$), the direct effect of system rotation is to reduce $\langle \bar{u}_2''^2 \rangle$ (or $\bar{u}_{2,\mathrm{rms}}$) because $G_{22} < 0$ and the magnitude of G_{22} increases with Ro monotonically, which feature is evident in Fig. 5.15(a). In consequence, as shown in Figs. 5.16(a) and 5.17(a), the total production rate and the level of $\bar{u}_{2,\mathrm{rms}}$ decreases monotonically as Ro increases near the smooth wall.

Under clockwise rotation ($Ro < 0$), the Coriolis force has a stabilizing effect on the flow near the rib-roughened wall of the channel. As shown in Fig. 5.15(b), the profile of G_{22} peaks near both the ribbed and smooth wall regions, and the magnitude of the

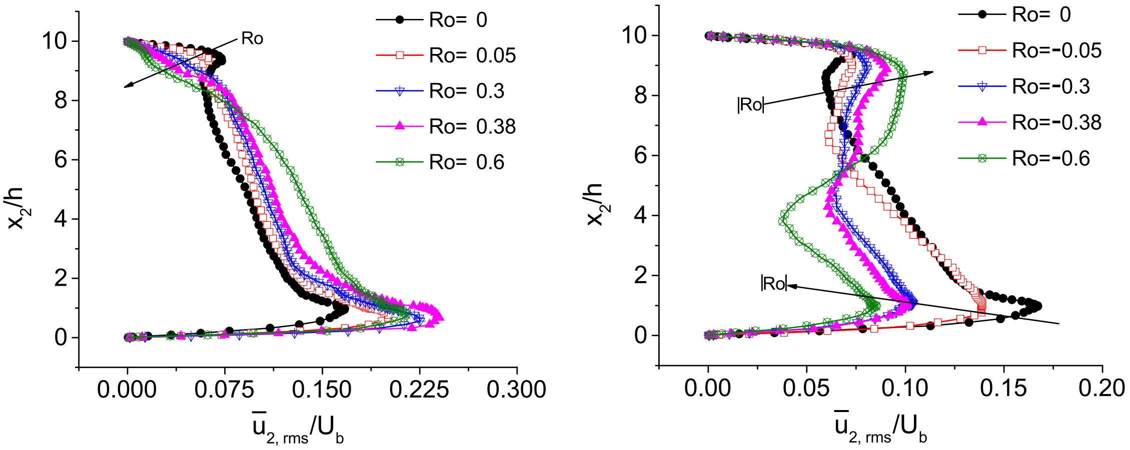

(a) Counter-clockwise rotation (b) Clockwise rotation

FIGURE 5.17: Resolved wall-normal RMS velocity profiles for different rotation numbers at the streamwise location $x_1/h = 4$.

peak value increases monotonically as the $|Ro|$ increases. Near the ribbed (suction) side, the rotational stress production term maintains $G_{22} < 0$. This tends to decrease both the total production rate and the level of $\langle \bar{u}_2''^2 \rangle$ near the rib-roughened wall, which pattern is clearly shown in Figs. 5.16(b) and 5.17(b). The rotation effects on the flow are obvious even at the lowest rotation number tested ($Ro = -0.05$). As is apparent in Fig. 5.15(b), G_{22} becomes negatively valued at $Ro = -0.05$ in the region close to the roughed wall. Correspondingly, as shown in Fig. 5.17(b), the peak value of $\langle \bar{u}_2''^2 \rangle$ for $Ro = -0.05$ around elevation $x_2/h \approx 1.0$ decreases by 17.1% in comparison with that for $Ro = 0$. Furthermore, as shown in Fig. 5.16(b), the wall-normal location where the total production is negative penetrates deeper towards the roughened wall, as the stabilizing effect of clockwise rotation increases with $|Ro|$. On the pressure (or, smooth) side of the channel, the rotational stress production term maintains $G_{22} > 0$, which tends to increase the level of $\langle \bar{u}_2''^2 \rangle$. Indeed, as shown in Figs. 5.16(b) and 5.17(b), the total production rate and the level of $\bar{u}_{2,\mathrm{rms}}$ increase monotonically as $|Ro|$ increases near the smooth wall. Finally, in comparison with Fig. 5.17(a), it is interesting to observe that the profile of $\bar{u}_{2,\mathrm{rms}}$ shown in Fig. 5.17(b) becomes increasingly symmetric as $|Ro|$ increases, which is due to the fact that the roughness effect caused by ribs is offset by the increasing stabilizing effect of clockwise rotation.

Chapter 6

Conclusions and Future Work

A 3-D in-house CFD code has been developed to conduct hybrid RANS/LES of wall-bounded turbulent flows. The code is modified from an existing computer code originally developed by LePoudre [57]. The original computer code is based on a staggered grid system for computing lid driven cavity laminar flows. In order to conduct the current hybrid RANS/LES, the code has been significantly modified based on a collocated grid arrangement and new implementations of closure models. The computer code is written using FORTRAN 90/95 programming languages and fully parallelized using message passing interface library. All hybrid simulations are executed on WestGrid (a multi-cluster high-performance computing consortium encompassing 14 major partner institutions in Western Canada).

In this thesis, a novel dynamic forcing model incorporating backscatter is proposed for hybrid RANS/LES. The forcing and its associated model coefficients C_W and C_N can be dynamically determined using the local instantaneous flow field at each time step. Therefore, in contrast to previous forcing techniques in literature, the proposed forcing in this research is more physically sound than the forcing based on stochastic white noises, and more convenient to implement than that extracted from auxiliary reference DNS or high-resolution LES databases. The proposed dynamic forcing has been thoroughly tested in the context of plane channel flows and spanwise rotating channel flows. A simplified forcing model with only one dynamic coefficient has been also proposed and tested in the context of rib-roughened channel flows with and without system rotations. In the following subsections, major conclusions on testing of the proposed forcing models for hybrid RANS/LES study of three selected benchmark flows will be summarized.

6.1 Plane Channel Flow

The effects of the dynamic forcing on reduction of the thickness and impact of the artificial buffer layer are investigated based on the study of a turbulent plane channel flow. For hybrid RANS/LES without forcing, the observation of super-streaks by Baggett [16] is confirmed in this research. Super-streaks cause a de-correlation between streamwise and wall-normal fluctuations. Correspondingly, the resolved $\bar{u}_{2,\mathrm{rms}}$ is excessively damped around the interface (if no forcing is applied in hybrid RANS/LES), which then results in an unphysical shift-up of the velocity profile to compensate the production for the resolved shear stresses, forming the so-called artificial buffer layer.

In order to identify the important factors for improving the forcing techniques for hybrid RANS/LES, the proposed dynamic forcing scheme has been tested in three different regions. It is demonstrated in this thesis that backscatter can be generated to properly treat the interfacing problem once the forcing is activated in either the RANS or the LES zone, or even throughout the entire domain. The value of the mean spanwise spacing between the near-wall streaks λ^+ has been significantly reduced from 255.3 to 127.6 when the forcing is activated. The dynamic forcing is insensitive to the region where it is applied, and super-streaks can be effectively broken up to remove the artificial buffer layer regardless the choices of the forcing region. Furthermore, a comparative study has been conducted to investigate the effects of interface locations of the RANS and LES regions. Three characteristic interface locations have been tested, corresponding to the viscous sublayer, buffer layer and overlap region, respectively. It is observed that as long as the forcing is in use, the velocity shift around the modelling interface and the associated artificial buffer layer have been successfully removed in all three test cases, indicating that the current hybrid approach is insensitive to the choices of the interface location. These are encouraging modelling features, which are fundamentally important for stable and flexible numerical simulations. It would be beneficial to further test whether these modelling features are also valid based on a dynamically prescribed interface.

In hybrid RANS/LES, the length scales resolved in LES and RANS are significantly different, which makes it important to study the effects of the grid resolution on the predicted flow field. It is observed that the grid independent state is achieved on a grid system of minimum 48^3 control volumes with respect to both the first- and second-order flow statistics of a plane channel flow. As a result, the proposed hybrid approach has saved 99.12% and 99.91% of computational cost for $Re_\tau = 650$ and $Re_\tau = 1020$, respectively, in comparison with that used in the DNS study of Iwamoto *et al.* [63] and Abe *et al.* [62]. This advantage of hybrid RANS/LES over DNS in terms of saving of computational cost is obvious. In a hybrid approach, the position of the first node off the solid wall is no longer restricted to be $\Delta x_2^+ \leq 1$ due to the use of the RANS approach in the near-wall region.

In order to examine the predictive performance of the proposed hybrid approach in terms of the momentum balance based on different SGS models in the LES zone, the budget of the shear stresses has been studied. It is observed that once the modelled shear stress component is included, the profiles of the total Reynolds shear stress obtained from the current hybrid approach are in excellent agreement with the DNS data at $Re_\tau = 650$ and 1020. Furthermore, the total shear stress balance predicted by two different SGS models (i.e., the SM and DSM) is well satisfied in the LES zone.

6.2 Rotating Channel Flow

The predictive performance of the dynamic forcing scheme is further evaluated based on the study of a spanwise rotating channel flow, in which a special body force (i.e., the Coriolis force) imposes additional challenges on turbulence models to reflect and predict the effects of rotation. The turbulent flow field subjected to the system rotation is characterized by the Reynolds number fixed to $Re_\tau = 650$, which is higher than that in previous numerical simulations of rotating channel flows in literature [20, 61, 71, 78, 80]. A series of rotation numbers ranging from $Ro_\tau = 0$ to 15 have been tested in order to investigate the effects of Coriolis forces on the flow field. The proposed hybrid approach can successfully predict prototypical features of the flow field in a rotating channel such as Taylor-Görtler vortices, the resolved mean velocity and resolved turbulent stresses. It is shown that the physical effect of the Coriolis force on the flow field is to stabilize the suction side and to destabilize the pressure side, suppressing and enhancing the level of turbulence on these two sides, respectively.

In response to the spanwise system rotaion, two pairs of persistent Taylor-Görtler vortices are observed at the rotation number $Ro_\tau = 2.5$. As the rotation number increases to 15, the flow layer on the suction side becomes thicker and more stable and the number of Taylor-Görtler vortex pairs increases to three. Owing to the presence of the Taylor-Görtler vortices induced by the Coriolis force, the wall shear stress (and also the friction velocity) on the pressure side becomes greater than that on the suction side. Furthermore, for the rotating channel flow cases, the mean resolved velocity profiles become increasingly asymmetric as rotation number Ro_τ increases. In the core region, the mean resolved velocity profiles become approximately linear with slope Ro_τ, implying the existence of the neutral stability zone. The thickness of the neutral stability zone increases as rotation number Ro_τ increases. Under the same rotation number Ro_τ, the neutral stability zone is stretched wider in the central core of the channel at a higher Reynolds number. As the Reynolds number increases, the inertial forces increase, which work against the laminarization trend near the suction side.

When the channel flow is imposed with rotation, the magnitude of all three components of the resolved turbulent intensity becomes much higher on the pressure side than on the suction side, indicating that the flow on the pressure side is more turbulent than that on the suction side. The effects of the Coriolis force on resolved turbulent stresses can be studied through their production terms (namely, P_{ij} arising from the mean resolved turbulent stresses, and G_{ij} arising from the presence of Coriolis accelerations in a rotating channel flow). Near the suction wall of the channel, the level of $\langle \bar{u}_2''^2 \rangle$ (or $\bar{u}_{2,rms}$) is reduced, because $G_{22} < 0$ and the magnitude of G_{22} increases with Ro_τ. The level of the total production $P_{12} + G_{12}$ for the turbulent shear stress increases, which then results in an increase in the value of $-\langle \bar{u}_1'' \bar{u}_2'' \rangle$ (correspondingly, a reduction in its magnitude) on the suction side. Near the pressure wall of the channel, the rotational stress production terms maintain $G_{22} > 0$ and $G_{12} > 0$, which tend to increase the levels of $\langle \bar{u}_2''^2 \rangle$ and $-\langle \bar{u}_1'' \bar{u}_2'' \rangle$.

In order to examine the predictive performance of the current hybrid RANS/LES approach in terms of the momentum balance, the budget of the shear stresses has been studied. The total shear stress balance predicted for both non-rotating and rotating channel flows is well satisfied in both RANS and LES zones. In the shear stresses budget, the resolved viscous shear stress dominates in the viscous sublayer, while the resolved turbulent shear stress dominates in the fully turbulent layer away from the wall. For the non-rotating channel flow case, the profile of each shear stress component features an anti-symmetrical pattern about channel center (located at $x_2/\delta = 0$). However, when system rotation is imposed, this physical feature no longer holds. Both the total and resolved Reynolds shear stresses become much higher on the pressure side than on the suction side.

Due to its self-calibrating mechanism, the dynamic forcing is able to reflect the anisotropic effect of the Coriolis force in the wall-normal direction. In the non-rotating case, a symmetrical dual-peak patterned backscatter distribution exhibits in the wall-normal profile of $\langle P_r^B \rangle$. In the rotating case, although the dual-peak pattern of the backscatter produced by forcing is preserved, the strength of the backscatter is significantly enhanced on the pressure side of the channel, reflecting the physical mechanism that the turbulence level is enhanced on the pressure side and suppressed on the suction side by the Coriolis force.

6.3 Rotating Rib-Roughened Channel Flow

The predictive performance of the simplified dynamic forcing scheme is evaluated based on the study of a rotating rib-roughened channel flow, which is subjected to the combined effects of the Coriolis force and roughness. The turbulent flow field studied in this study is characterized by a fixed Reynolds number of $Re = 1.5 \times 10^4$. A wide range of rotation numbers (ranging from -0.6 to 0.6) is tested in order to study the effects of the Coriolis force on the rib-roughed channel flow. The first- and second-order flow statistics and the reattachment length under both clockwise and counterclockwise system rotations obtained from the simulations are validated against recent PIV measurement data of Coletti *et al.* [41–43].

Due to the presence of ribs on one of the two channel walls, the wall-normal symmetry of the channel is broken, and the effects of clockwise and counter-clockwise rotations on the turbulent flow field are drastically different. Under clockwise rotation and counter-clockwise rotation, the wall-normal component of the Coriolis force ($-2\Omega\bar{u}_1$) points to the smooth wall and ribbed wall, respectively. Hence, the pressure side of the channel (to which the Coriolis force points to) is opposite and the secondary flows induced by the Coriolis force exhibit different dynamics under these two opposite rotating conditions. The shear layer induced by the ribs and the boundary layer developing over the rib-roughened wall are stabilized under clockwise rotation (for $Ro < 0$), whereas destabilized under counter-clockwise rotation (for $Ro > 0$).

In response to spanwise system rotation, Taylor-Görtler vortices appear near the smooth and rib-roughened walls under clockwise and counter-clockwise rotations, respectively. Under counter-clockwise rotation, the secondary flows sweep the high-speed fluids from the channel center towards the rib-roughened wall, leading to a higher level of mean streamwise velocity $\langle \bar{u}_1 \rangle$ near the roughened wall. Furthermore, turbulence intensity levels ($\bar{u}_{1,\mathrm{rms}}$ and $\bar{u}_{2,\mathrm{rms}}$), TKE and turbulent shear stresses $-\langle \bar{u}_1'' \bar{u}_2'' \rangle$ are greatly increased near the roughened wall. In contrast, under clockwise rotation, due to the stabilizing effect of the Coriolis force, the levels of turbulence intensities, TKE and turbulent shear stresses are suppressed near the roughened wall.

By comparing the mean wall-normal velocity $\langle \bar{u}_2 \rangle$ profiles along the streamwise direction under different rotating conditions, counter-clockwise rotation results in the maximum magnitude of the downward velocity. An understanding of this physical mechanism is particularly important in the cooling of turbomachinery and rotating electronic devices, as it influences the flow rate of the cold fluid from the mainstream towards the hot roughened surfaces.

The system rotation modifies strongly the mean flow features. In particular, the recirculation bubble shrinks under counter-clockwise rotations, whereas extends in the streamwise direction in a more pronounced manner under clockwise rotations. As such, counter-clockwise rotation leads to an earlier reattachment and a reduction in the reattachment length, and opposite trends are observed under clockwise rotations. Specifically, under counter-clockwise rotation, the reattachment length asymptotes to a constant level around $3.50h$ as Ro increases from 0.3 to 0.6. In contrast, under clockwise rotation, the reattachment length extends and covers the entire inter-rib region at $Ro = -0.6$, switching from k-type roughness to intermediate or d-type roughness. This is an interesting result, which implies that the classification of the roughness types based on the classical concepts of Perry *et al.* [91] now relies not only on the pitch ration L_p/h, but also on the rotation number Ro in the context of rotating rib-roughened flows.

The impact of the Coriolis force on the range of the instantaneous reattachment zone is also investigated. Within this zone, the instantaneous reattachment point moves back and forth along the floor in response to the flapping motion of the free shear layer. For the non-rotating case ($Ro = 0$), the streamwise length of the oscillation zone is $1.19h$, which however, further reduces to $1.0h$ under counter-clockwise rotation (for $Ro = 0.38$) and extends to $1.8h$ under clockwise rotation (for $Ro = -0.38$).

Because the effect of ribs and the effect of rotation mutually influence each other, the production terms for the resolved turbulent stresses are more complicated than those in the plane channel flow without ribs. As indicated by Visscher and Andersson [105], the production rate G_{22} arising from the rotational stress due to the Coriolis accelerations is a key parameter in understanding the influence of rotation on turbulent shear flows at moderate rotating speeds. The sign of G_{22} depends on the condition whether the wall-normal component of the fluctuating Coriolis force acts to promote or suppress the wall-normal velocity fluctuations $\bar{u}_2''$. Under counter-clockwise rotation, the effect of the Coriolis force is destabilizing the rib-roughened wall and $G_{22} > 0$ holds. For small and moderate rotation numbers (for $Ro \leq 0.38$), G_{22} maintains positively-valued and increases with Ro near the rib-roughened wall. As a consequence, the level of $\langle \bar{u}_2''^2 \rangle$ increases monotonically as Ro increases from 0 to 0.38. As the rotation number continues to increase from 0.38 to 0.6, re-stabilization occurs, and as a result, both G_{22} and the level of $\langle \bar{u}_2''^2 \rangle$ decrease in the region near the rib-roughened wall. Under clockwise rotation, near the ribbed side, the rotational stress production term maintains $G_{22} < 0$. Both the total production rate and the level of $\langle \bar{u}_2''^2 \rangle$ decrease with the rotating speed (indicated by the value of $|Ro|$) near the rib-roughened wall. Furthermore, the profile of $\bar{u}_{2,\mathrm{rms}}$ becomes increasingly symmetric as $|Ro|$ increases, which is due to the fact that the roughness effect caused by ribs is offset by the increasing stabilizing effect of clockwise rotation.

In order to remove the artificial buffer layer, the conventional strategy has focused primarily on determining the value of the eddy viscosity ν_t, by e.g., adjusting ν_t to an 'ideal' value to maintain the budget of shear stresses [15, 110], and merging ν_t^R and ν_t^L using blending functions or different interface locations [11, 16]. In contrast, the current hybrid approach is based on a dynamic forcing scheme, which naturally incorporate backscatter and can generate a proper level of $\bar{u}_{2,\mathrm{rms}}$ and $-\langle \bar{u}_1'' \bar{u}_2'' \rangle$ without resulting to any pre-determined 'ideal' ν_t values and blending functions. The magnitudes of the eddy viscosity and modelled turbulent stress peak at the interface of the RANS and LES regions (for both the non-rotating and rotating channel flows), which is a desirable feature and a direct consequence of the backscatter of kinetic energy produced by the proposed forcing scheme. An enhanced level of modelled turbulence at the interface is often the key to the success of the forcing modelling in a hybrid approach for properly conducting LES for transient simulation of turbulence.

The predictive performance of the current hybrid approach is satisfactory based on the combination of algebraic closure models and the dynamic forcing scheme. The anisotropy of turbulent normal stresses in the near-wall region are well captured for the tested plane channel flows, rotating flows, and separating/reattaching flows. In view of this, it would be interesting to apply the proposed hybrid approaches to simulations of engineering turbulent flows with complex boundary conditions in such as heat exchangers and rotating machinery. Furthermore, it would be of significant interest to extend the scope of the thesis by incorporating the forcing scheme with more complex turbulence closure models such as second moment Reynolds stress closure model, and further testing the proposed forcing model based on other wall-bounded turbulent flows such as atmospheric flows and complex urban environment flows in future studies.

References

[1] D. C. Wilcox, *Turbulence Modelling for CFD.* California: DCW Industries, Inc., 3rd ed., 2006.

[2] M. Wosnik, L. Castillo, and W. K. George, “A theory for turbulent pipe and channel flows,” *J. Fluid Mech.*, vol. 421, pp. 115–145, 2000.

[3] S. B. Pope, *Turbulent Flows.* Cambridge, UK: Cambridge Univ., 2000.

[4] H. Tennekes and J. L. Lumley, *A First Course in Turbulence.* Cambridge, MA: MIT, 1972.

[5] S. Hoyas and J. Jiménez, “Scaling of the velocity fluctuations in turbulent channels up to $Re_\tau = 2003$,” *Phys. Fluids*, vol. 18, no. 011702, pp. 1–4, 2006.

[6] J. Larsson, *Towards large eddy simulation of boundary layer flows at high Reynolds number: statistical modeling of the inner layer.* PhD thesis, Univ. of Waterloo, Waterloo, Canada, 2006.

[7] D. R. Chapman, “Computational aerodynamics development and outlook,” *AIAA J.*, vol. 17, pp. 1293–1313, 1979.

[8] J. Fröhlich and D. von Terzi, “Hybrid LES/RANS methods for the simulation of turbulent flows,” *Prog. Aerosp. Sci.*, vol. 44, pp. 349–377, 2008.

[9] P. R. Spalart, W. H. Jou, M. K. Strelets, and S. R. Allmaras, “Comments on the feasibility of LES for wings, and on a hybrid RANS/LES approach,” in

First AFOSR International Conference on DNS/LES (C. Liu and Z. Liu, eds.), (Columbus, OH), pp. 137–147, Greyden Press, August 1997.

[10] L. Davidson and S. H. Peng, "Hybrid LES-RANS modeling: a one-equation SGS model combined with a k-ω model for predicting recirculating flows," *Int. J. Numer. Meth. Fluids*, vol. 43, pp. 1003–1018, 2003.

[11] L. Temmerman, M. Hadžiabdić, M. A. Leschziner, and K. Hanjalić, "A hybrid two-layer URANS-LES approach for large eddy simulation at high Reynolds numbers," *Int. J. Heat Fluid Flow*, vol. 26, pp. 173–190, 2005.

[12] P. G. Tucker and L. Davidson, "Zonal k-l based large-eddy simulations," *Comput. Fluids*, vol. 33, pp. 267–287, 2004.

[13] F. Hamba, "A hybrid RANS/LES simulation of turbulent channel flow," *Theor. Comput. Fluid Dyn.*, vol. 16, pp. 387–403, 2003.

[14] J. Larsson, F.-S. Lien, and E. Yee, "The artificial buffer layer and the effect of forcing in hybrid LES/RANS," *Int. J. Heat Fluid Flow*, vol. 28, pp. 1443–1459, 2007.

[15] N. V. Nikitin, F. Nicoud, B. Wasistho, K. D. Squires, and P. R. Spalart, "An approach to wall modeling in large-eddy simulations," *Phys. Fluids*, vol. 12, no. 7, pp. 1629–1632, 2000.

[16] J. S. Baggett, "On the feasibility of merging LES with RANS for the near-wall region of attached turbulent flows," in *Annu. Res. Briefs*, (California), pp. 267–277, Center Turbul. Res., Stanford Univ., 1998.

[17] P. A. Durbin, "Separated flow computations with the k-ε-v^2 model," *AIAA J.*, vol. 33, pp. 659–664, 1995.

[18] C. R. Smith and S. P. Metzler, "The characteristics of low-speed streaks in the near-wall region of a turbulent boundary layer," *J. Fluid Mech.*, vol. 129, pp. 27–54, 1983.

[19] J. Kim, P. Moin, and R. Moser, "Turbulence statistics in fully developed channel flow at low Reynolds number," *J. Fluid Mech.*, vol. 177, pp. 133–166, 1987.

[20] R. Kristoffersen and H. I. Andersson, "Direct simulations of low-Reynolds-number turbulent flow in a rotating channel," *J. Fluid Mech.*, vol. 256, pp. 163–197, 1993.

[21] S. I. Chernyshenko and M. F. Baig, "Streaks and vortices in near-wall turbulence," *Phil. Trans. R. Soc. A*, vol. 363, pp. 1097–1107, 2005.

[22] S. I. Chernyshenko and M. F. Baig, "The mechanism of streak formation in near-wall turbulence," *J. Fluid Mech.*, vol. 544, pp. 99–131, 2005.

[23] U. Piomelli, E. Balaras, H. Pasinato, K. D. Squires, and P. R. Spalart, "The inner-outer layer interface in large-eddy simulations with wall-layer models," *Int. J. Heat Fluid Flow*, vol. 24, pp. 538–550, 2003.

[24] L. Davidson and S. Dahlström, "Hybrid LES-RANS: An approach to make LES applicable at high Reynolds number," *Int. J. Comput. Fluid Dyn.*, vol. 19, no. 6, pp. 415–427, 2005.

[25] P. Batten, U. Goldberg, and S. Chakravarthy, "Interfacing statistical turbulence closures with large-eddy simulation," *AIAA J.*, vol. 42(3), pp. 485–492, 2004.

[26] L. Davidson and M. Billson, "Hybrid LES-RANS using synthesized turbulent fluctuations for forcing in the interface region," *Int. J. Heat Fluid Flow*, vol. 27, pp. 1028–1042, 2006.

[27] U. Piomelli and E. Balaras, “Wall-layer models for large-eddy simulations,” *Annu. Rev. Fluid Mech.*, vol. 34, pp. 349–374, 2002.

[28] U. Piomelli, “Wall-modeled large-eddy simulations: present status and prospects,” in *Direct and Large-Eddy Simulation VII, ERCOFTAC* (V. Armenio, B. Geurts, and J. Fröhlich, eds.), 13, Springer, 2010.

[29] J. W. Deardorff, “A numerical study of three-dimensional turbulent channel flow at large Reynolds numbers,” *J. Fluid Mech.*, vol. 41, pp. 453–480, 1970.

[30] U. Schumann, “Subgrid scale model for finite difference simulations of turbulent flows in plane channels and annuli,” *J. Comp. Phys.*, vol. 18, pp. 376–404, 1975.

[31] C. H. Moeng, “A large-eddy simulation model for the study of planetary boundary-layer turbulence,” *J. Atmos. Sci.*, vol. 41, pp. 2052–2062, 1984.

[32] U. Piomelli, J. Ferziger, P. Moin, and J. Kim, “New approximate boundary conditions for large eddy simulations of wall-bounded flows,” *Phys. Fluids*, vol. 1, pp. 1061–1068, 1989.

[33] F. Nicoud, J. S. Baggett, P. Moin, and W. Cabot, “Large eddy simulation wall-modeling based on suboptimal control theory and linear stochastic estimation,” *Phys. Fluids*, vol. 13, no. 10, pp. 2968–2984, 2001.

[34] E. Balaras, C. Benocci, and U. Piomelli, “Two-layer approximate boundary conditions for large-eddy simulations,” *AIAA J.*, vol. 34, no. 6, pp. 1111–1119, 1996.

[35] M. Wang and P. Moin, “Dynamic wall modeling for large-eddy simulation of complex turbulent flows,” *Phys. Fluids*, vol. 14, no. 7, pp. 2043–2051, 2002.

[36] E. Balaras and C. Benocci, “Subgrid-scale models in finite-difference simulations of complex wall bounded flows,” in *74th Fluid Dynamics Symposium on Application of Direct and Large Eddy Simulation to Transition and Turbulence*, no. AGARD-CP-551, (Neuilly-Sur-Seine, France), pp. 2.1–2.6, Advisory Group for Aerospace Research & Development (AGARD), April 1994.

[37] W. H. Cabot, “Near-wall models in large-eddy simulations of flow behind a backward-facing step,” in *Annu. Res. Briefs*, (California), pp. 199–210, Center Turbul. Res., Stanford Univ., 1996.

[38] G. V. Diurno, E. Balaras, and U. Piomelli, “Wall-layer models for les of separated flows,” in *Modern Simulation Strategies for Turbulent Flows* (B. Geurts, ed.), (Philadelphia, PA), pp. 207–222, R. T. Edwards, Inc., 2001.

[39] W. Gropp, E. Lusk, and A. Skjellum, *Using MPI: Portable Parallel Programming with the Message-Passing Interface.* Massachusetts: The MIT Press, 2nd ed., 1999.

[40] I. Foster, *Designing and Building Parallel Programs.* Boston: Addison-Wesley, 1995.

[41] F. Coletti, I. Cresci, and T. Arts, “Spatio-temporal analysis of the turbulent flow in a ribbed channel,” *Int. J. Heat Fluid Flow*, vol. 44, pp. 181–196, 2013.

[42] F. Coletti, T. Maurer, T. Arts, and A. Di Sante, “Flow field investigation in rotating rib-roughened channel by means of particle image velocimetry,” *Exp. Fluids*, vol. 52, pp. 1043–1061, 2012.

[43] F. Coletti, D. Lo Jacono, I. Cresci, and T. Arts, “Turbulent flow in rib-roughened channel under the effect of coriolis and rotational buoyancy forces,” *Phys. Fluids*, vol. 26, no. 045111, pp. 1–26, 2014.

[44] P. Sagaut and R. Grohens, "Discrete filters for large eddy simulation," *Int. J. Numer. Meth. Fluids*, vol. 31, pp. 1195–1220, 1999.

[45] M. Germano, U. Piomelli, P. Moin, and W. H. Cabot, "A dynamic subgrid-scale eddy viscosity model," *Phys. Fluids A*, vol. 3, pp. 1760–1765, 1991.

[46] J. Smagorinsky, "General circulation experiments with the primitive equations, I. the basic experiment," *Mon. Weath. Rev.*, vol. 91, pp. 99–165, 1963.

[47] D. K. Lilly, "A proposed modification of the Germano subgrid-scale closure method," *Phys. Fluids A*, vol. 4, pp. 633–635, 1992.

[48] K. Horiuti, "Roles of non-aligned eigenvectors of strain-rate and subgrid-scale stress tensors in turbulence generation," *J. Fluid Mech.*, vol. 491, pp. 65–100, 2003.

[49] B.-C. Wang and D. J. Bergstrom, "A dynamic nonlinear subgrid-scale stress model," *Phys. Fluids*, vol. 17(035109), pp. 1–15, 2005.

[50] B.-C. Wang, D. J. Bergstrom, J. Yin, and E. Yee, "Turbulence topologies predicted using large eddy simulations," *J. Turbul.*, vol. 7, no. 34, pp. 1–28, 2006.

[51] B.-C. Wang, E. Yee, D. J. Bergstrom, and O. Iida, "New dynamic subgrid-scale heat flux models for large-eddy simulation of thermal convection based on the general gradient diffusion hypothesis," *J. Fluid Mech.*, vol. 604, pp. 125–163, 2008.

[52] L. Davidson, "Hybrid LES-RANS: back scatter from a scale-similarity model used as forcing," *Phil. Trans. R. Soc. A*, vol. 367, pp. 2905–2915, 2009.

[53] S. Völker, R. D. Moser, and P. Venugopal, "Optimal large eddy simulation of

turbulent channel flow based on direct numerical simulation statistical data," *Phys. Fluids*, vol. 14, pp. 3675–3691, 2002.

[54] A. Bhattacharya, A. Das, and R. D. Moser, "A filtered-wall formulation for large-eddy simulation of wall-bounded turbulent," *Phys. Fluids*, vol. 20, no. 115104, pp. 1–16, 2008.

[55] M. Germano, "Properties of the hybrid RANS/LES filter," *Theor. Comput. Fluid Dyn.*, vol. 17, pp. 225–231, 2004.

[56] B. Rajamani and J. Kim, "A hybrid-filter approach to turbulence simulation," *Flow, Turbul. Combust.*, vol. 85, pp. 421–441, 2010.

[57] P. P. LePoudre, "Parallel unsteady Navier-Stokes solver using a fully conservative discretization and an implicit fractional step method," Master's thesis, Univ. of Saskatchewan, Saskatoon, Canada, August 2003.

[58] J. Kim and P. Moin, "Application of a fractional-step method to incompressible Navier-Stokes equations," *J. Comp. Phys.*, vol. 59, pp. 308–323, 1985.

[59] H. Choi and P. Moin, "Effects of the computational time step on numerical solutions of turbulent flow," *J. Comp. Phys.*, vol. 113, pp. 1–4, 1994.

[60] J. H. Ferziger and M. Perić, *Computational Methods for Fluid Dynamics*. Berlin: Springer, 2nd ed., 1999.

[61] Q.-Q. Xun, B.-C. Wang, and E. Yee, "Large-eddy simulation of turbulent heat convection in a spanwise rotating channel flow," *Int. J. Heat Mass Trans.*, vol. 54, pp. 698–716, 2011.

[62] H. Abe, H. Kawamura, and Y. Matsuo, "Surface heat-flux fluctuations in a

turbulent channel flow up to $Re_\tau = 1020$ with $Pr = 0.025$ and 0.71," *Int. J. Heat Fluid Flow*, vol. 25, pp. 404–419, 2004.

[63] K. Iwamoto, Y. Suzuki, and N. Kasagi, "Reynolds number effect on wall turbulence: Toward effective feedback control," *Int. J. Heat Fluid Flow*, vol. 23, pp. 678–689, 2002.

[64] C. Meneveau, "Germano identity-based subgrid-scale modeling: A brief survey of variations on a fertile theme," *Phys. Fluids*, vol. 24, no. 121301, pp. 1–14, 2012.

[65] U. Piomelli, Y. Yu, and R. J. Adrian, "Subgrid-scale energy transfer and near-wall turbulence structure," *Phys. Fluids*, vol. 8, pp. 215–224, 1996.

[66] A. G. Kravchenko, P. Moin, and R. Moser, "Zonal embedded grids for numerical simulations of wall-bounded turbulent flows," *J. Comp. Phys.*, vol. 127, pp. 412–423, 1996.

[67] G. S. Winckelmans, H. Jeanmart, and D. Carati, "On the comparison of turbulence intensities from large-eddy simulation with those from experiment or direct numerical simulation," *Phys. Fluids*, vol. 14, pp. 1809–1811, 2002.

[68] P. Sagaut, *Large Eddy Simulation for Incompressible Flows: An Introduction.* Berlin: Springer, 3rd ed., 2006.

[69] J. P. Johnston, R. M. Halleen, and D. K. Lezius, "Effects of spanwise rotation on the structure of two-dimensional fully developed turbulent channel flow," *J. Fluid Mech.*, vol. 56, pp. 533–557, 1972.

[70] J. H. Watmuff, H. T. Witt, and P. N. Joubert, "Developing turbulent boundary layers with system rotation," *J. Fluid Mech.*, vol. 157, pp. 405–448, 1985.

[71] O. Grundestam, S. Wallin, and A. V. Johansson, “Direct numerical simulation of rotating turbulent channel flow,” *J. Fluid Mech.*, vol. 598, pp. 177–199, 2008.

[72] P. Bradshaw, “The analogy between streamline curvature and buoyancy in turbulent shear flow,” *J. Fluid Mech.*, vol. 36, pp. 177–191, 1969.

[73] K. Nakabayashi and O. Kitoh, “Low reynolds number fully developed two-dimensional turbulent channel flow with system rotation,” *J. Fluid Mech.*, vol. 315, pp. 1–29, 1996.

[74] K. Nakabayashi and O. Kitoh, “Turbulence characteristics of two-dimensional channel flow with system rotation,” *J. Fluid Mech.*, vol. 528, pp. 355–377, 2005.

[75] J. P. Bons and J. L. Kerrebrock, “Complementary velocity and heat transfer measurements in a rotating turbine cooling passage with smooth walls,” *ASME J. Turbomach.*, vol. 121, pp. 651–662, 1999.

[76] A. Di Sante, R. Theunissen, and R. A. Van den Braembussche, “A new facility for time resolved PIV measurements in rotating channels,” *Exp. Fluids*, vol. 44, pp. 179–188, 2008.

[77] L. Belhoucine, M. Deville, A. R. Elazehari, and M. O. Bensalah, “Explicit algebraic reynolds stress model of incompressible turbulent flow in rotating square duct,” *Comput. Fluids*, vol. 33, pp. 179–199, 2004.

[78] S. Wallin, O. Grundestam, and A. V. Johansson, “Laminarization mechanisms and extreme-amplitude states in rapidly rotating plane channel flow,” *J. Fluid Mech.*, vol. 730, pp. 193–219, 2013.

[79] J. Pallares and L. Davidson, “Large-eddy simulations of turbulent flow in a rotating square duct,” *Phys. Fluids*, vol. 12, pp. 2878–2894, 2000.

[80] Q.-Q. Xun, B.-C. Wang, and E. Yee, "Quasi-periodicity of the drag coefficient and Nusselt number induced by Taylor-Görtler vortices," *Numer. Heat Trans.: Part B*, vol. 57, pp. 30–45, 2010.

[81] I. A. Hunt and P. N. Joubert, "Effects of small streamline curvature on turbulent duct flow," *J. Fluid Mech.*, vol. 91, pp. 633–659, 1979.

[82] P. H. Hoffmann, K. C. Muck, and P. Bradshaw, "The effect of concave surface curvature on turbulent boundary layers," *J. Fluid Mech.*, vol. 161, pp. 371–403, 1985.

[83] R. D. Moser and P. Moin, "The effects of curvature in wall-bounded turbulent flows," *J. Fluid Mech.*, vol. 175, pp. 479–510, 1987.

[84] M. Nishimura and N. Kasagi, "Direct numerical simulation of combined forced and natural turbulent convection in a rotating plane channel," in *3rd KSME-JSME Therm. Eng. Conf.*, pp. 77–82, 1996. DNS data available from the Turbulence and Heat Transfer Laboratory (N. Kasagi) at University of Tokyo, http://www.thtlab.t.u-tokyo.ac.jp/.

[85] M. Agelinchaab and M. F. Tachie, "PIV study of separated and reattached open channel flow over surface mounted blocks," *ASME J. Fuids. Eng.*, vol. 130, no. 061206, pp. 1–9, 2008.

[86] D. N. Ryu, D. H. Choi, and V. C. Patel, "Analysis of turbulent flow in channels roughened by two-dimensional ribs and three-dimensional blocks. Part I: Resistance," *Int. J. Heat Fluid Flow*, vol. 28, pp. 1098–1111, 2007.

[87] S. Leonardi, P. Orlandi, R. J. Smalley, L. Djenidi, and R. A. Antonia, "Direct numerical simulations of turbulent channel flow with transverse square bars on one wall," *J. Fluid Mech.*, vol. 491, pp. 229–238, 2003.

[88] S. Leonardi, P. Orlandi, L. Djenidi, and R. A. Antonia, “Structure of turbulent channel flow with square bars on one wall,” *Int. J. Heat Fluid Flow*, vol. 25, pp. 384–392, 2004.

[89] Y. Nagano, H. Hattori, and T. Houra, “DNS of velocity and thermal fields in turbulent channel flow with transverse-rib roughness,” *Int. J. Heat Fluid Flow*, vol. 25, pp. 393–403, 2004.

[90] J. Cui, V. C. Patel, and C.-L. Lin, “Large-eddy simulation of turbulent flow in a channel with rib roughness,” *Int. J. Heat Fluid Flow*, vol. 24, pp. 372–388, 2003.

[91] A. E. Perry, W. H. Schofield, and P. Joubert, “Rough wall turbulent boundary layers,” *J. Fluid Mech.*, vol. 37, pp. 383–413, 1969.

[92] P. K. Panigrahi and S. Acharya, “Mechanism of flow transport in turbine blade coolant passage with a rib turbulator,” *ASME J. Turbomach.*, vol. 121, pp. 152–159, 1999.

[93] Y. Z. Liu, F. Ke, and H. J. Sung, “Unsteady separated and reattaching turbulent flow over a two-dimensional square rib,” *J. Fluids Struct.*, vol. 24, pp. 366–381, 2008.

[94] J. C. Han, “Heat transfer and friction in channels with two opposite rib-roughened walls,” *ASME J. Heat Trans.*, vol. 106, no. 4, pp. 774–781, 1984.

[95] T.-M. Liou and J.-J. Hwang, “Turbulent heat transfer and friction in periodically fully developed channel flows,” *ASME J. Heat Trans.*, vol. 114, pp. 56–64, 1992.

[96] R. Fransen, L. Vial, and L. Y. M. Gicquel, “Large eddy simulation of rotating ribbed channel,” in *ASME Turbo Expo 2013*, no. GT2013-95076, p. 10 pages, June 2013.

[97] V. D. Narasimhamurthy and H. I. Andersson, “Turbulence statistics in a rotating ribbed channel,” *Int. J. Heat Fluid Flow*, 2014.

[98] Y. Liu, P. G. Tucker, and G. L. Iacono, “Comparison of zonal RANS and LES for a non-isothermal ribbed channel flow,” *Int. J. Heat Fluid Flow*, vol. 27, pp. 391–401, 2006.

[99] S. Kubacki, J. Rokicki, and E. Dick, “Hybrid RANS/LES of flow in a rib-roughened rotating channel,” in *ASME Turbo Expo 2014*, no. GT2014-26194, p. 12 pages, June 2014.

[100] M. Breuer, B. Jaffrézic, and K. Arora, “Hybrid LES-RANS technique based on a one-equation near-wall model,” *Theor. Comput. Fluid Dyn.*, vol. 22, pp. 157–187, 2008.

[101] P. H. Rothe and J. P. Johnston, “Free shear layer behavior in rotating systems,” *ASME J. Fuids. Eng.*, vol. 101, pp. 117–120, 1979.

[102] G. Rau, M. Çakan, D. Moeller, and T. Arts, “The effect of periodic ribs on the local aerodynamic and heat transfer performance of a straight cooling channel,” *ASME J. Turbomach.*, vol. 120, pp. 368–375, 1998.

[103] D. K. Tafti, “Evaluating the role of subgrid stress modeling in a ribbed duct for the internal cooling of turbine blades,” *Int. J. Heat Fluid Flow*, vol. 26, pp. 92–104, 2005.

[104] S. M. Islam, L. Haga, M. Kaminaga, R. Hino, and M. Monde, “Experimental analysis of turbulent flow structure in a fully developed rib-roughened rectangular channel with PIV,” *Exp. Fluids*, vol. 33, pp. 296–306, 2002.

[105] J. Visscher and H. I. Andersson, “Particle image velocimetry measurements of massively separated turbulent flows with rotation,” *Phys. Fluids*, vol. 23, no. 075108, pp. 1–13, 2011.

[106] M. Barri and H. I. Andersson, “Turbulent flow over a backward-facing step. Part I: effects of anti-cyclonic system rotation,” *J. Fluid Mech.*, vol. 665, pp. 382–417, 2010.

[107] J. K. Eaton and J. P. Johnston, “A review of research on subsonic turbulent flow reattachment,” *AIAA J.*, vol. 19, pp. 1093–1100, 1981.

[108] I. Lee and H. J. Sung, “Multiple-arrayed pressure measurement for investigation of the unsteady flow structure of a reattaching shear layer,” *J. Fluid Mech.*, vol. 463, pp. 377–402, 2002.

[109] M. Kiya and K. Sasaki, “Structure of large-scale vortices and unsteady reverse flow in the reattaching zone of a turbulent separation bubble,” *J. Fluid Mech.*, vol. 154, pp. 463–491, 1985.

[110] P. J. Mason and D. J. Thomson, “Stochastic backscatter in large-eddy simulations of boundary layers,” *J. Fluid Mech.*, vol. 242, pp. 51–78, 1992.

[111] P. R. Spalart, S. Deck, M. L. Shur, K. D. Squires, M. K. Strelets, and A. Travin, “A new version of detached-eddy simulation, resistant to ambiguous grid densities,” *Theor. Comput. Fluid Dyn.*, vol. 20, pp. 181–195, 2006.

Appendix A

Discretization of Momentum and Continuity Equations

In this appendix, the discretization of the momentum and continuity equations based on the fractional step method [59] is presented.

A.1 Grids and Dimensions

Figure A.1 shows a typical 3-D Cartesian control volume (CV). The CV surface can be subdivided into six side faces, denoted by lower case letters corresponding to their directions (e, w, n, s, f, b) with respect to the central node (P). In the following context, subscripts e, w, n, s, f and b represent *east*, *west*, *north*, *south*, *front* and *back* faces of a CV, respectively; $A_1 = \Delta x_2 \cdot \Delta x_3$, $A_2 = \Delta x_1 \cdot \Delta x_3$ and $A_3 = \Delta x_1 \cdot \Delta x_2$ are the areas of side faces that are perpendicular to the streamwise (x_1), wall-normal (x_2) and spanwise (x_3) directions, respectively; and $\Delta V = \Delta x_1 \cdot \Delta x_2 \cdot \Delta x_3$ is the volume of the CV.

A straightforward approximation for the value at a CV face is a linear interpolation between the two nearest nodal values. At locations e and w on a Cartesian grid system shown in Fig. A.2, we have

$$\phi_e = \lambda_e \phi_E + (1 - \lambda_e)\phi_P \quad , \tag{A.1}$$

and

$$\phi_w = \lambda_w \phi_W + (1 - \lambda_w)\phi_P \quad , \tag{A.2}$$

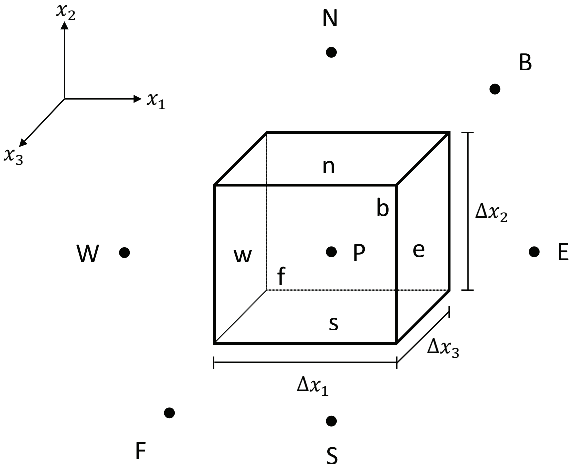

FIGURE A.1: Schematic of the control volume for the collocated grid system.

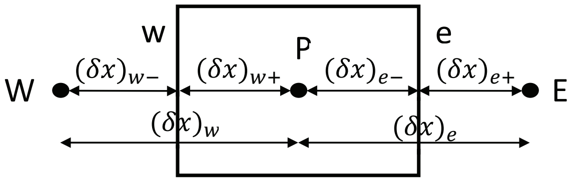

FIGURE A.2: 2-D schematic of the control volume and its dimensions.

where ϕ is a random quantity, and the linear interpolation factors λ_e and λ_w are defined as:

$$\lambda_e = \frac{(\delta x)_{e-}}{(\delta x)_e} \quad , \tag{A.3}$$

and

$$\lambda_w = \frac{(\delta x)_{w+}}{(\delta x)_w} \quad , \tag{A.4}$$

respectively. The approximation of the gradient at CV face is also evaluated by assuming a linear profile between the two nearest nodes, i.e.

$$\left(\frac{\partial \phi}{\partial x_1}\right)_e \approx \frac{\phi_E - \phi_P}{(\delta x)_e} \quad , \tag{A.5}$$

and

$$\left(\frac{\partial \phi}{\partial x_1}\right)_w \approx \frac{\phi_P - \phi_W}{(\delta x)_w} \quad . \tag{A.6}$$

The method to evaluate values at faces e and w above can be similarly used to evaluate values at faces n, s, f and b.

A.2 Discretized Momentum Equation

Details to discretize the streamwise momentum equation are demonstrated in the following context. After discretization, coefficients in the algebraic equation are obtained. The coefficients for wall-normal and spanwise momentum equations can be also derived on a collocated grid system in a similar manner.

Integrating the convective term over the CV shown in Fig. A.1, the following equation is obtained:

$$\begin{aligned}\int_b^f \int_s^n \int_w^e \frac{\partial}{\partial x_1}(\bar{u}_1\bar{u}_1)dx_1dx_2dx_3 &= \dot{m}_e\bar{u}_e - \dot{m}_w\bar{u}_w \\ &= \dot{m}_e\left[(1-\lambda_e)\bar{u}_P + \lambda_e\bar{u}_E\right] \\ &\quad - \dot{m}_w\left[(1-\lambda_w)\bar{u}_P + \lambda_w\bar{u}_W\right] \\ &= (\dot{m}_e\lambda_e)\bar{u}_E - (\dot{m}_w\lambda_w)\bar{u}_W \\ &\quad + \left[\dot{m}_e(1-\lambda_e) - \dot{m}_w(1-\lambda_w)\right]\bar{u}_P \quad ;\end{aligned} \tag{A.7}$$

and

$$\begin{aligned}\int_b^f \int_w^e \int_s^n \frac{\partial}{\partial x_2}(\bar{u}_1\bar{u}_2)dx_2dx_1dx_3 &= \dot{m}_n\bar{u}_n - \dot{m}_s\bar{u}_s \\ &= \dot{m}_n\left[(1-\lambda_n)\bar{u}_P + \lambda_n\bar{u}_N\right] \\ &\quad - \dot{m}_s\left[(1-\lambda_s)\bar{u}_P + \lambda_s\bar{u}_S\right] \\ &= (\dot{m}_n\lambda_n)\bar{u}_N - (\dot{m}_s\lambda_s)\bar{u}_S \\ &\quad + \left[\dot{m}_n(1-\lambda_n) - \dot{m}_s(1-\lambda_s)\right]\bar{u}_P \quad ;\end{aligned} \tag{A.8}$$

and

$$\begin{aligned}\int_w^e \int_s^n \int_b^f \frac{\partial}{\partial x_3}(\bar{u}_1\bar{u}_3)dx_3dx_2dx_1 &= \dot{m}_f\bar{u}_f - \dot{m}_b\bar{u}_b \\ &= \dot{m}_f\left[(1-\lambda_f)\bar{u}_P + \lambda_f\bar{u}_F\right] \\ &\quad - \dot{m}_b\left[(1-\lambda_b)\bar{u}_P + \lambda_b\bar{u}_B\right] \\ &= (\dot{m}_f\lambda_f)\bar{u}_F - (\dot{m}_b\lambda_b)\bar{u}_B \\ &\quad + \left[\dot{m}_f(1-\lambda_f) - \dot{m}_b(1-\lambda_b)\right]\bar{u}_P \quad .\end{aligned} \tag{A.9}$$

Integrating the diffusive term over the CV shown in Fig. A.1, the following equation is obtained:

$$
\begin{aligned}
\int_b^f \int_s^n \int_w^e \frac{\partial}{\partial x_1}\left(\frac{\partial \bar{u}_1}{\partial x_1}\right) dx_1 dx_2 dx_3 &= A_1 \left[\left(\frac{\partial \bar{u}_1}{\partial x_1}\right)_e - \left(\frac{\partial \bar{u}_1}{\partial x_1}\right)_w\right] \\
&= A_1 \left[\left(\frac{\bar{u}_E - \bar{u}_P}{(\delta x)_e}\right) - \left(\frac{\bar{u}_P - \bar{u}_W}{(\delta x)_w}\right)\right] \\
&= \left[\frac{A_1}{(\delta x)_e}\right] \bar{u}_E + \left[\frac{A_1}{(\delta x)_w}\right] \bar{u}_W \\
&\quad - \left[\frac{A_1}{(\delta x)_e} + \frac{A_1}{(\delta x)_w}\right] \bar{u}_P \quad ;
\end{aligned}
\tag{A.10}
$$

and

$$
\begin{aligned}
\int_b^f \int_w^e \int_s^n \frac{\partial}{\partial x_2}\left(\frac{\partial \bar{u}_1}{\partial x_2}\right) dx_2 dx_1 dx_3 &= A_2 \left[\left(\frac{\partial \bar{u}_1}{\partial x_2}\right)_n - \left(\frac{\partial \bar{u}_1}{\partial x_2}\right)_s\right] \\
&= A_2 \left[\left(\frac{\bar{u}_N - \bar{u}_P}{(\delta y)_n}\right) - \left(\frac{\bar{u}_P - \bar{u}_S}{(\delta y)_s}\right)\right] \\
&= \left[\frac{A_2}{(\delta y)_n}\right] \bar{u}_N + \left[\frac{A_2}{(\delta y)_s}\right] \bar{u}_S \\
&\quad - \left[\frac{A_2}{(\delta y)_n} + \frac{A_2}{(\delta y)_s}\right] \bar{u}_P \quad ;
\end{aligned}
\tag{A.11}
$$

and

$$
\begin{aligned}
\int_w^e \int_s^n \int_b^f \frac{\partial}{\partial x_3}\left(\frac{\partial \bar{u}_1}{\partial x_3}\right) dx_3 dx_2 dx_1 &= A_3 \left[\left(\frac{\partial \bar{u}_1}{\partial x_3}\right)_f - \left(\frac{\partial \bar{u}_1}{\partial x_3}\right)_b\right] \\
&= A_3 \left[\left(\frac{\bar{u}_F - \bar{u}_P}{(\delta z)_f}\right) - \left(\frac{\bar{u}_P - \bar{u}_B}{(\delta z)_b}\right)\right] \\
&= \left[\frac{A_3}{(\delta z)_f}\right] \bar{u}_F + \left[\frac{A_3}{(\delta z)_b}\right] \bar{u}_B \\
&\quad - \left[\frac{A_3}{(\delta z)_f} + \frac{A_3}{(\delta z)_b}\right] \bar{u}_P \quad .
\end{aligned}
\tag{A.12}
$$

Integrating the pressure gradient term over the CV shown in Fig. A.1, the following equation is obtained:

$$
\begin{aligned}
\int_b^f \int_s^n \int_w^e \left(\frac{\partial \bar{p}}{\partial x_1}\right) dx_1 dx_2 dx_3 &= A_1 (\bar{p}_e - \bar{p}_w) \\
&= A_1 \left\{[(1-\lambda_e)\bar{p}_P + \lambda_e \bar{p}_E] - [(1-\lambda_w)\bar{p}_P + \lambda_w \bar{p}_W]\right\} \quad .
\end{aligned}
\tag{A.13}
$$

Integrating the sub-grid stress term over the CV shown in Fig. A.1, the following equation is obtained:

$$\int_b^f \int_s^n \int_w^e \left(\frac{\partial \tau_{11}}{\partial x_1}\right) dx_1 dx_2 dx_3 = A_1(\tau_e - \tau_w)$$
$$= A_1 \left\{[(1-\lambda_e)\tau_{_P} + \lambda_e \tau_{_E}] - [(1-\lambda_w)\tau_{_P} + \lambda_w \tau_{_W}]\right\} \quad ; \tag{A.14}$$

and

$$\int_b^f \int_w^e \int_s^n \left(\frac{\partial \tau_{12}}{\partial x_2}\right) dx_2 dx_1 dx_3 = A_2(\tau_n - \tau_s)$$
$$= A_2 \left\{[(1-\lambda_n)\tau_{_P} + \lambda_n \tau_{_N}] - [(1-\lambda_s)\tau_{_P} + \lambda_s \tau_{_S}]\right\} \quad ; \tag{A.15}$$

and

$$\int_w^e \int_s^n \int_b^f \left(\frac{\partial \tau_{13}}{\partial x_3}\right) dx_3 dx_2 dx_1 = A_3(\tau_f - \tau_b)$$
$$= A_3 \left\{[(1-\lambda_f)\tau_{_P} + \lambda_f \tau_{_F}] - [(1-\lambda_b)\tau_{_P} + \lambda_b \tau_{_B}]\right\} \quad . \tag{A.16}$$

Integrating the Coriolis force term over the CV shown in Fig. A.1, the following equation is obtained:

$$\int_b^f \int_s^n \int_w^e 2\Omega \bar{u}_2 dx_1 dx_2 dx_3 = 2\Omega \bar{u}_2 \Delta V \quad . \tag{A.17}$$

Integrating the forcing term over the CV shown in Fig. A.1, the following equation is obtained:

$$\int_b^f \int_s^n \int_w^e \left(\frac{\partial \tau_{11}^B}{\partial x_1}\right) dx_1 dx_2 dx_3 = A_1(\tau_e^B - \tau_w^B)$$
$$= A_1 \left\{\left[(1-\lambda_e)\tau_{_P}^B + \lambda_e \tau_{_E}^B\right] - \left[(1-\lambda_w)\tau_{_P}^B + \lambda_w \tau_{_W}^B\right]\right\} \quad ; \tag{A.18}$$

and

$$\int_b^f \int_w^e \int_s^n \left(\frac{\partial \tau_{12}^B}{\partial x_2}\right) dx_2 dx_1 dx_3 = A_2(\tau_n^B - \tau_s^B)$$

$$= A_2\left\{\left[(1-\lambda_n)\tau_{P}^{B}+\lambda_n\tau_{N}^{B}\right]-\left[(1-\lambda_s)\tau_{P}^{B}+\lambda_s\tau_{S}^{B}\right]\right\} \quad ; \tag{A.19}$$

and

$$\begin{aligned}\int_w^e\int_s^n\int_b^f\left(\frac{\partial\tau_{13}^{B}}{\partial x_3}\right)dx_3dx_2dx_1 &= A_3(\tau_f^B-\tau_b^B)\\ &= A_3\left\{\left[(1-\lambda_f)\tau_{P}^{B}+\lambda_f\tau_{F}^{B}\right]-\left[(1-\lambda_b)\tau_{P}^{B}+\lambda_b\tau_{B}^{B}\right]\right\} \quad .\end{aligned} \tag{A.20}$$

The filtered (or ensemble averaged) momentum equation is written as:

$$\frac{\partial\bar{u}_i}{\partial t}+\frac{\partial}{\partial x_j}(\bar{u}_i\bar{u}_j)=-\frac{1}{\rho}\frac{\partial\bar{p}}{\partial x_i}+\nu\frac{\partial^2\bar{u}_i}{\partial x_j\partial x_j}-\frac{\partial\tau_{ij}}{\partial x_j}+2\varepsilon_{ij3}\Omega\bar{u}_j-\frac{\partial\tau_{ij}^{B}}{\partial x_j} \quad . \tag{A.21}$$

Applying the fractional step method suggested by Choi and Moin [59] to Eq. (A.21), the following equation is obtained:

$$\begin{aligned}\frac{\bar{u}_i^{(\star)}-\bar{u}_i^{(n)}}{\Delta t} =& -\frac{1}{4}\frac{\partial\left\{\left[\bar{u}_j^{(\star)}+\bar{u}_j^{(n)}\right]\left[\bar{u}_i^{(\star)}+\bar{u}_i^{(n)}\right]\right\}}{\partial x_j}\\ &+\frac{\nu}{2}\frac{\partial^2\left[\bar{u}_i^{(\star)}+\bar{u}_i^{(n)}\right]}{\partial x_j\partial x_j}-\frac{1}{\rho}\frac{\partial\bar{p}^{(n)}}{\partial x_i}-\frac{\partial\tau_{ij}^{(n)}}{\partial x_j}+2\varepsilon_{ij3}\Omega\bar{u}_j^{(n)}-\frac{\partial\tau_{ij}^{B(n)}}{\partial x_j} \quad .\end{aligned} \tag{A.22}$$

For a collocated grid system, all variables share the same CV. After expansion, the streamwise momemtum equation (i.e. $i=1$ in Eq. (A.22)) is integrated over the CV shown in Fig. A.1, i.e.

$$\begin{aligned}\frac{\bar{u}_1^{(\star)}-\bar{u}_1^{(n)}}{\Delta t}\Delta V =& -\frac{1}{4}\int_b^f\int_s^n\int_w^e\frac{\partial\left\{\left[\bar{u}_1^{(\star)}+\bar{u}_1^{(n)}\right]\left[\bar{u}_1^{(\star)}+\bar{u}_1^{(n)}\right]\right\}}{\partial x_1}dx_1dx_2dx_3\\ &-\frac{1}{4}\int_b^f\int_w^e\int_s^n\frac{\partial\left\{\left[\bar{u}_2^{(\star)}+\bar{u}_2^{(n)}\right]\left[\bar{u}_1^{(\star)}+\bar{u}_1^{(n)}\right]\right\}}{\partial x_2}dx_2dx_1dx_3\\ &-\frac{1}{4}\int_w^e\int_s^n\int_b^f\frac{\partial\left\{\left[\bar{u}_3^{(\star)}+\bar{u}_3^{(n)}\right]\left[\bar{u}_1^{(\star)}+\bar{u}_1^{(n)}\right]\right\}}{\partial x_3}dx_3dx_2dx_1\\ &+\frac{\nu}{2}\int_b^f\int_s^n\int_w^e\frac{\partial^2\left[\bar{u}_1^{(\star)}+\bar{u}_1^{(n)}\right]}{\partial x_1\partial x_1}dx_1dx_2dx_3\end{aligned}$$

$$
\begin{aligned}
&+\frac{\nu}{2}\int_b^f\int_w^e\int_s^n \frac{\partial^2\left[\bar{u}_1^{(\star)}+\bar{u}_1^{(n)}\right]}{\partial x_2\partial x_2}dx_2dx_1dx_3\\
&+\frac{\nu}{2}\int_w^e\int_s^n\int_b^f \frac{\partial^2\left[\bar{u}_1^{(\star)}+\bar{u}_1^{(n)}\right]}{\partial x_3\partial x_3}dx_3dx_2dx_1\\
&-\frac{1}{\rho}\int_b^f\int_s^n\int_w^e \frac{\partial\bar{p}^{(n)}}{\partial x_1}dx_1dx_2dx_3\\
&-\int_b^f\int_s^n\int_w^e \frac{\partial\tau_{11}^{(n)}}{\partial x_1}dx_1dx_2dx_3\\
&-\int_b^f\int_w^e\int_s^n \frac{\partial\tau_{12}^{(n)}}{\partial x_2}dx_2dx_1dx_3\\
&-\int_w^e\int_s^n\int_b^f \frac{\partial\tau_{13}^{(n)}}{\partial x_3}dx_3dx_2dx_1\\
&+\int_b^f\int_s^n\int_w^e 2\Omega\bar{u}_2^{(n)}dx_1dx_2dx_3\\
&-\int_b^f\int_s^n\int_w^e \frac{\partial\tau_{11}^{B(n)}}{\partial x_1}dx_1dx_2dx_3\\
&-\int_b^f\int_w^e\int_s^n \frac{\partial\tau_{12}^{B(n)}}{\partial x_2}dx_2dx_1dx_3\\
&-\int_w^e\int_s^n\int_b^f \frac{\partial\tau_{13}^{B(n)}}{\partial x_3}dx_3dx_2dx_1 \quad . \qquad \text{(A.23)}
\end{aligned}
$$

Equation (A.23) can be further evaluated to

$$
\begin{aligned}
\frac{\bar{u}_P^{(\star)}-\bar{u}_P^{(n)}}{\Delta t}\Delta V = &-\frac{1}{4}(\dot{m}_e^{(\star)}+\dot{m}_e^{(n)})\lambda_e\bar{u}_E^{(\star)}+\frac{1}{4}(\dot{m}_w^{(\star)}+\dot{m}_w^{(n)})\lambda_w\bar{u}_W^{(\star)}\\
&-\frac{1}{4}\left[(\dot{m}_e^{(\star)}+\dot{m}_e^{(n)})(1-\lambda_e)-(\dot{m}_w^{(\star)}+\dot{m}_w^{(n)})(1-\lambda_w)\right]\bar{u}_P^{(\star)}\\
&-\frac{1}{4}(\dot{m}_e^{(\star)}+\dot{m}_e^{(n)})\lambda_e\bar{u}_E^{(n)}+\frac{1}{4}(\dot{m}_w^{(\star)}+\dot{m}_w^{(n)})\lambda_w\bar{u}_W^{(n)}\\
&-\frac{1}{4}\left[(\dot{m}_e^{(\star)}+\dot{m}_e^{(n)})(1-\lambda_e)-(\dot{m}_w^{(\star)}+\dot{m}_w^{(n)})(1-\lambda_w)\right]\bar{u}_P^{(n)}\\
&-\frac{1}{4}(\dot{m}_n^{(\star)}+\dot{m}_n^{(n)})\lambda_n\bar{u}_N^{(\star)}+\frac{1}{4}(\dot{m}_s^{(\star)}+\dot{m}_s^{(n)})\lambda_s\bar{u}_S^{(\star)}\\
&-\frac{1}{4}\left[(\dot{m}_n^{(\star)}+\dot{m}_n^{(n)})(1-\lambda_n)-(\dot{m}_s^{(\star)}+\dot{m}_s^{(n)})(1-\lambda_s)\right]\bar{u}_P^{(\star)}\\
&-\frac{1}{4}(\dot{m}_n^{(\star)}+\dot{m}_n^{(n)})\lambda_n\bar{u}_N^{(n)}+\frac{1}{4}(\dot{m}_s^{(\star)}+\dot{m}_s^{(n)})\lambda_s\bar{u}_S^{(n)}\\
&-\frac{1}{4}\left[(\dot{m}_n^{(\star)}+\dot{m}_n^{(n)})(1-\lambda_n)-(\dot{m}_s^{(\star)}+\dot{m}_s^{(n)})(1-\lambda_s)\right]\bar{u}_P^{(n)}\\
&-\frac{1}{4}(\dot{m}_f^{(\star)}+\dot{m}_f^{(n)})\lambda_f\bar{u}_F^{(\star)}+\frac{1}{4}(\dot{m}_b^{(\star)}+\dot{m}_b^{(n)})\lambda_b\bar{u}_B^{(\star)}
\end{aligned}
$$

$$
\begin{aligned}
&-\frac{1}{4}\left[(\dot m_f^{(\star)}+\dot m_f^{(n)})(1-\lambda_f)-(\dot m_b^{(\star)}+\dot m_b^{(n)})(1-\lambda_b)\right]\bar u_P^{(\star)}\\
&-\frac{1}{4}(\dot m_f^{(\star)}+\dot m_f^{(n)})\lambda_f\bar u_F^{(n)}+\frac{1}{4}(\dot m_b^{(\star)}+\dot m_b^{(n)})\lambda_b\bar u_B^{(n)}\\
&-\frac{1}{4}\left[(\dot m_f^{(\star)}+\dot m_f^{(n)})(1-\lambda_f)-(\dot m_b^{(\star)}+\dot m_b^{(n)})(1-\lambda_b)\right]\bar u_P^{(n)}\\
&+\frac{\nu}{2}\left[\frac{A_1}{(\delta x)_e}\right]\bar u_E^{(\star)}+\frac{\nu}{2}\left[\frac{A_1}{(\delta x)_w}\right]\bar u_W^{(\star)}-\frac{\nu}{2}\left[\frac{A_1}{(\delta x)_e}+\frac{A_1}{(\delta x)_w}\right]\bar u_P^{(\star)}\\
&+\frac{\nu}{2}\left[\frac{A_1}{(\delta x)_e}\right]\bar u_E^{(n)}+\frac{\nu}{2}\left[\frac{A_1}{(\delta x)_w}\right]\bar u_W^{(n)}-\frac{\nu}{2}\left[\frac{A_1}{(\delta x)_e}+\frac{A_1}{(\delta x)_w}\right]\bar u_P^{(n)}\\
&+\frac{\nu}{2}\left[\frac{A_2}{(\delta y)_n}\right]\bar u_N^{(\star)}+\frac{\nu}{2}\left[\frac{A_2}{(\delta y)_s}\right]\bar u_S^{(\star)}-\frac{\nu}{2}\left[\frac{A_2}{(\delta y)_n}+\frac{A_2}{(\delta y)_s}\right]\bar u_P^{(\star)}\\
&+\frac{\nu}{2}\left[\frac{A_2}{(\delta y)_n}\right]\bar u_N^{(n)}+\frac{\nu}{2}\left[\frac{A_2}{(\delta y)_s}\right]\bar u_S^{(n)}-\frac{\nu}{2}\left[\frac{A_2}{(\delta y)_n}+\frac{A_2}{(\delta y)_s}\right]\bar u_P^{(n)}\\
&+\frac{\nu}{2}\left[\frac{A_3}{(\delta z)_f}\right]\bar u_F^{(\star)}+\frac{\nu}{2}\left[\frac{A_3}{(\delta z)_b}\right]\bar u_B^{(\star)}-\frac{\nu}{2}\left[\frac{A_3}{(\delta z)_f}+\frac{A_3}{(\delta z)_b}\right]\bar u_P^{(\star)}\\
&+\frac{\nu}{2}\left[\frac{A_3}{(\delta z)_f}\right]\bar u_F^{(n)}+\frac{\nu}{2}\left[\frac{A_3}{(\delta z)_b}\right]\bar u_B^{(n)}-\frac{\nu}{2}\left[\frac{A_3}{(\delta z)_f}+\frac{A_3}{(\delta z)_b}\right]\bar u_P^{(n)}\\
&-\frac{A_1}{\rho}\left\{\left[(1-\lambda_e)\bar p_P^{(n)}+\lambda_e\bar p_E^{(n)}\right]-\left[(1-\lambda_w)\bar p_P^{(n)}+\lambda_w\bar p_W^{(n)}\right]\right\}\\
&-A_1\left\{\left[(1-\lambda_e)\tau_P^{(n)}+\lambda_e\tau_E^{(n)}\right]-\left[(1-\lambda_w)\tau_P^{(n)}+\lambda_w\tau_W^{(n)}\right]\right\}\\
&-A_2\left\{\left[(1-\lambda_n)\tau_P^{(n)}+\lambda_n\tau_N^{(n)}\right]-\left[(1-\lambda_s)\tau_P^{(n)}+\lambda_s\tau_S^{(n)}\right]\right\}\\
&-A_3\left\{\left[(1-\lambda_f)\tau_P^{(n)}+\lambda_f\tau_F^{(n)}\right]-\left[(1-\lambda_b)\tau_P^{(n)}+\lambda_b\tau_B^{(n)}\right]\right\}\\
&+2\Omega\bar u_2^{(n)}\Delta V\\
&-A_1\left\{\left[(1-\lambda_e)\tau_P^{B(n)}+\lambda_e\tau_E^{B(n)}\right]-\left[(1-\lambda_w)\tau_P^{B(n)}+\lambda_w\tau_W^{B(n)}\right]\right\}\\
&-A_2\left\{\left[(1-\lambda_n)\tau_P^{B(n)}+\lambda_n\tau_N^{B(n)}\right]-\left[(1-\lambda_s)\tau_P^{B(n)}+\lambda_s\tau_S^{B(n)}\right]\right\}\\
&-A_3\left\{\left[(1-\lambda_f)\tau_P^{B(n)}+\lambda_f\tau_F^{B(n)}\right]-\left[(1-\lambda_b)\tau_P^{B(n)}+\lambda_b\tau_B^{B(n)}\right]\right\}\quad .
\end{aligned}
\tag{A.24}
$$

Assembling all terms in Eq. (A.24) and dividing all terms through by ΔV, then gathering terms to write in the form:

$$
\begin{aligned}
a_P\bar u_P^{(\star)} &= \sum a_{NP}\bar u_{NP}^{(\star)}+b\\
&= a_E\bar u_E^{(\star)}+a_W\bar u_W^{(\star)}+a_N\bar u_N^{(\star)}+a_S\bar u_S^{(\star)}+a_F\bar u_F^{(\star)}+a_B\bar u_B^{(\star)}+b\quad ,
\end{aligned}
\tag{A.25}
$$

where subscript NP is used to indicate a quantity at the neighboring nodes; and a

and b denote the coefficients and source term, respectively. By comparing Eq. (A.25) with Eq. (A.24), the coefficients at the neighboring nodes can be written as:

$$\begin{aligned}
a_E &= -\frac{(\dot{m}_e^{(\star)} + \dot{m}_e^{(n)})\lambda_e}{4\Delta V} + \frac{\nu}{2(\delta x)_e \Delta x_1} \quad , \\
a_W &= \frac{(\dot{m}_w^{(\star)} + \dot{m}_w^{(n)})\lambda_w}{4\Delta V} + \frac{\nu}{2(\delta x)_w \Delta x_1} \quad , \\
a_N &= -\frac{(\dot{m}_n^{(\star)} + \dot{m}_n^{(n)})\lambda_n}{4\Delta V} + \frac{\nu}{2(\delta y)_n \Delta x_2} \quad , \\
a_S &= \frac{(\dot{m}_s^{(\star)} + \dot{m}_s^{(n)})\lambda_s}{4\Delta V} + \frac{\nu}{2(\delta y)_s \Delta x_2} \quad , \\
a_F &= -\frac{(\dot{m}_f^{(\star)} + \dot{m}_f^{(n)})\lambda_f}{4\Delta V} + \frac{\nu}{2(\delta z)_f \Delta x_3} \quad , \\
a_B &= \frac{(\dot{m}_b^{(\star)} + \dot{m}_b^{(n)})\lambda_b}{4\Delta V} + \frac{\nu}{2(\delta z)_b \Delta x_3} \quad ,
\end{aligned} \tag{A.26}$$

and the coefficient at the central node can be written as:

$$\begin{aligned}
a_P &= \frac{1}{\Delta t} + \sum a_{NP} \\
&= \frac{1}{\Delta t} + a_E + a_W + a_N + a_S + a_F + a_B \quad .
\end{aligned} \tag{A.27}$$

Similarly, the source term can be written as:

$$\begin{aligned}
b = {} & \sum a_{NP}\bar{u}_{NP}^{(n)} - a_P\bar{u}_P^{(n)} + \frac{2}{\Delta t}\bar{u}_P^{(n)} \\
& - \frac{1}{\rho\Delta x_1}\left\{\left[(1-\lambda_e)\bar{p}_P^{(n)} + \lambda_e\bar{p}_E^{(n)}\right] - \left[(1-\lambda_w)\bar{p}_P^{(n)} + \lambda_w\bar{p}_W^{(n)}\right]\right\} \\
& - \frac{1}{\Delta x_1}\left\{\left[(1-\lambda_e)\tau_P^{(n)} + \lambda_e\tau_E^{(n)}\right] - \left[(1-\lambda_w)\tau_P^{(n)} + \lambda_w\tau_W^{(n)}\right]\right\} \\
& - \frac{1}{\Delta x_2}\left\{\left[(1-\lambda_n)\tau_P^{(n)} + \lambda_n\tau_N^{(n)}\right] - \left[(1-\lambda_s)\tau_P^{(n)} + \lambda_s\tau_S^{(n)}\right]\right\} \\
& - \frac{1}{\Delta x_3}\left\{\left[(1-\lambda_f)\tau_P^{(n)} + \lambda_f\tau_F^{(n)}\right] - \left[(1-\lambda_b)\tau_P^{(n)} + \lambda_b\tau_B^{(n)}\right]\right\} \\
& + 2\Omega\bar{u}_2^{(n)} \\
& - \frac{1}{\Delta x_1}\left\{\left[(1-\lambda_e)\tau_P^{B(n)} + \lambda_e\tau_E^{B(n)}\right] - \left[(1-\lambda_w)\tau_P^{B(n)} + \lambda_w\tau_W^{B(n)}\right]\right\} \\
& - \frac{1}{\Delta x_2}\left\{\left[(1-\lambda_n)\tau_P^{B(n)} + \lambda_n\tau_N^{B(n)}\right] - \left[(1-\lambda_s)\tau_P^{B(n)} + \lambda_s\tau_S^{B(n)}\right]\right\} \\
& - \frac{1}{\Delta x_3}\left\{\left[(1-\lambda_f)\tau_P^{B(n)} + \lambda_f\tau_F^{B(n)}\right] - \left[(1-\lambda_b)\tau_P^{B(n)} + \lambda_b\tau_B^{B(n)}\right]\right\} \quad .
\end{aligned} \tag{A.28}$$

A.3 Discretized Continuity (Poisson) Equation

In the following context, the discretization of the continuity equation is demonstrated. In the fractional step method suggested by Choi and Moin [59], the continuity (Poisson) equation for pressure at time level $(n+1)$ is:

$$\frac{\partial^2 \bar{p}^{(n+1)}}{\partial x_i \partial x_i} = \frac{2\rho}{\Delta t}\frac{\partial \bar{u}_i^{(\star\star)}}{\partial x_i} \quad . \tag{A.29}$$

Integrating the above equation over the CV shown in Fig. A.1, the following equation is obtained:

$$\begin{aligned}
&\frac{\Delta t}{2\rho}\int_b^f\int_s^n\int_w^e\left(\frac{\partial^2 \bar{p}^{(n+1)}}{\partial x_1 \partial x_1}+\frac{\partial^2 \bar{p}^{(n+1)}}{\partial x_2 \partial x_2}+\frac{\partial^2 \bar{p}^{(n+1)}}{\partial x_3 \partial x_3}\right)dx_1dx_2dx_3\\
&=\int_b^f\int_s^n\int_w^e\left(\frac{\partial \bar{u}_1^{(\star\star)}}{\partial x_1}\right)dx_1dx_2dx_3+\int_b^f\int_w^e\int_s^n\left(\frac{\partial \bar{u}_2^{(\star\star)}}{\partial x_2}\right)dx_1dx_2dx_3\\
&\quad+\int_w^e\int_s^n\int_b^f\left(\frac{\partial \bar{u}_3^{(\star\star)}}{\partial x_3}\right)dx_3dx_2dx_1 \quad .
\end{aligned} \tag{A.30}$$

Equation (A.30) can be further written as:

$$\begin{aligned}
&\frac{\Delta t}{2\rho}\left[A_1\left(\frac{\bar{p}_E^{(n+1)}-\bar{p}_P^{(n+1)}}{(\delta x)_e}-\frac{\bar{p}_P^{(n+1)}-\bar{p}_W^{(n+1)}}{(\delta x)_w}\right)\right]\\
&\quad+\frac{\Delta t}{2\rho}\left[A_2\left(\frac{\bar{p}_N^{(n+1)}-\bar{p}_P^{(n+1)}}{(\delta y)_n}-\frac{\bar{p}_P^{(n+1)}-\bar{p}_S^{(n+1)}}{(\delta y)_s}\right)\right]\\
&\quad+\frac{\Delta t}{2\rho}\left[A_3\left(\frac{\bar{p}_F^{(n+1)}-\bar{p}_P^{(n+1)}}{(\delta z)_f}-\frac{\bar{p}_P^{(n+1)}-\bar{p}_B^{(n+1)}}{(\delta z)_b}\right)\right]\\
&=A_1\left[\bar{u}_e^{(\star\star)}-\bar{u}_w^{(\star\star)}\right]+A_2\left[\bar{u}_n^{(\star\star)}-\bar{u}_s^{(\star\star)}\right]+A_3\left[\bar{u}_f^{(\star\star)}-\bar{u}_b^{(\star\star)}\right] \quad .
\end{aligned} \tag{A.31}$$

Assembling all terms in Eq. (A.31) and dividing all terms through by ΔV, then gathering terms to write in the form:

$$\begin{aligned}
a_P\bar{p}_P^{(n+1)} &= \sum a_{NP}\bar{p}_{NP}^{(n+1)}+b\\
&= a_E\bar{p}_P^{(n+1)}+a_W\bar{p}_P^{(n+1)}+a_N\bar{p}_P^{(n+1)}+a_S\bar{p}_P^{(n+1)}+a_F\bar{p}_P^{(n+1)}+a_B\bar{p}_P^{(n+1)}+b \quad ,
\end{aligned} \tag{A.32}$$

where the coefficients at the neighboring nodes can be written as:

$$\begin{aligned}
a_E &= \frac{\Delta t}{2\rho}\frac{1}{(\delta x)_e \Delta x_1} \quad , \\
a_W &= \frac{\Delta t}{2\rho}\frac{1}{(\delta x)_w \Delta x_1} \quad , \\
a_N &= \frac{\Delta t}{2\rho}\frac{1}{(\delta y)_n \Delta x_2} \quad , \\
a_S &= \frac{\Delta t}{2\rho}\frac{1}{(\delta y)_s \Delta x_2} \quad , \\
a_F &= \frac{\Delta t}{2\rho}\frac{1}{(\delta z)_f \Delta x_3} \quad , \\
a_B &= \frac{\Delta t}{2\rho}\frac{1}{(\delta z)_b \Delta x_3} \quad ,
\end{aligned} \tag{A.33}$$

and the coefficient at the central node can be written as:

$$\begin{aligned}
a_P &= \sum a_{NP} \\
&= a_E + a_W + a_N + a_S + a_F + a_B \quad .
\end{aligned} \tag{A.34}$$

Similarly, the source term can be written as:

$$b = -\left[\frac{\bar{u}_e^{(\star\star)} - \bar{u}_w^{(\star\star)}}{\Delta x_1} + \frac{\bar{u}_n^{(\star\star)} - \bar{u}_s^{(\star\star)}}{\Delta x_2} + \frac{\bar{u}_f^{(\star\star)} - \bar{u}_b^{(\star\star)}}{\Delta x_3} \right] \quad . \tag{A.35}$$